UNIVERSITY OF CALIFORNIA,
IRVINE

Cosmology Through Einstein's Lens: Understanding Galaxy Structure and Evolution Using Strong Gravitational Lensing

DISSERTATION

submitted in partial satisfaction of the requirements
for the degree of

DOCTOR OF PHILOSOPHY

in Physics

by

Nicholas Timmons

Dissertation Committee:
Professor Asantha Cooray, Chair
Professor James Bullock
Professor Kevork Abazajian

2019

DEDICATION

For my father.

TABLE OF CONTENTS

LIST OF FIGURES

LIST OF TABLES

ACKNOWLEDGMENTS

First and foremost I would like to acknowledge the immense gratitude I have for the mentorship and friendship of my advisor Dr. Asantha Cooray. Without his tireless guidence I would not be where I am today. Secondly, I would like to give a special thanks to Caitlyn Casey and Hooshang Nayyeri whom taught me nearly everything I know about astrophysics research. A big thank you to Ketron Mitchell-Wynne, Jae Calanog and Cameron Thacker for their patience and friendship as I navigated the early years. Lastly, I have to thank my friends, family and my darling Laura for supporting me on this long journey.

Financial support for this work was provided by NASA through grant HST-GO-13399 from the Space Telescope Science Institute, which is operated by Associated Universities for Research in Astronomy, Inc., under NASA contract NAS 5-26555. Additional support from NASA grants NASA NNX16AJ69G, NASA NNX16AF39G, HST-AR-13886.001-A, IGPP LANL 368641, NSF AST-1313319 and Ax Foundation for Cosmology at UC San Diego as well as the GAANN fellowship.

Some of the data presented herein were obtained at the W.M. Keck Observatory, which is operated as a scientific partnership among the California Institute of Technology, the University of California and the National Aeronautics and Space Administration. The Observatory was made possible by the generous financial support of the W.M. Keck Foundation. The authors wish to recognize and acknowledge the very significant cultural role and reverence that the summit of Mauna Kea has always had within the indigenous Hawaiian community. We are most fortunate to have the opportunity to conduct observations from this mountain. The Submillimeter Array is a joint project between the Smithsonian Astrophysical Observatory and the Academia Sinica Institute of Astronomy and Astrophysics and is funded by the Smithsonian Institution and the Academia Sinica. H-ATLAS is a project with Herschel, which is an ESA space observatory with science instruments provided by European-led Principal Investigator consortia and with important participation from NASA. The H-ATLAS website is http://www.h-atlas.org/.

A significant portion of the text in this dissertation is a reprint of the material as it appears in "Dust and Stellar Emission from Lensed High Redshift Simulations of Galaxies in FIRE 2 Simulations" (ApJ in prep.), "Halo Pressure Profile through the Skew Cross-Power Spectrum of Sunyaev-Zel'dovich Effect and CMB Lensing in Planck" (ApJL, 849, 6), Multi-wavelength Lens Reconstruction of a Planck & Herschel -Detected Starbursting Galaxy" (ApJ, 829, 21) in addition to "Extinction and Nebular Line Properties of a Herschel Lensed Dusty Starburst at z = 1.207" (ApJ, 805, 140). The co-authors listed in these publications di- rected and supervised research which forms the basis for the following dissertation. The author would like to acknowledge the Astrophysical Journal for granting permission to reproduce their previous work in this dissertation.

CURRICULUM VITAE

Nicholas Timmons

EDUCATION

Doctor of Philosophy in Physics **2019**
University of California, Irvine *Irvine, CA*

Master of Science in Physics **2018**
University of California, Irvine *Irvine, CA*

Bachelor of Science in Phyics **2015**
University of California, Irvine *Irvine, CA*

RESEARCH EXPERIENCE

Graduate Research Assistant **2015–2019**
University of California, Irvine *Irvine, California*

TEACHING EXPERIENCE

Teaching Assistant **2015–2019**
University of California, Irvine *Irvine, CA*

Professor of Astronomy, Part-time **2017–2019**
Orange Coast College *Costa Mesa, CA*

REFEREED JOURNAL PUBLICATIONS

1. "Dust and Stellar Emission from Lensed High Redshift Simulations of Galaxies in FIRE 2 Simulations"
   Timmons et al. *ApJ in prep.*

2. "Halo Pressure Profile through the Skew Cross-Power Spectrum of Sunyaev-Zel'dovich Effect and CMB Lensing in Planck"
   Timmons et al. ApJL, 849, 6 (2017)

3. "Multi-wavelength Lens Reconstruction of a Planck & Herschel -Detected Starbursting Galaxy"
   Timmons et al. ApJ, 829, 21 (2016)

4. "Extinction and Nebular Line Properties of a Herschel Lensed Dusty Starburst at z = 1.207"
   Timmons et al. ApJ, 805, 140 (2015)

5. "The molecular gas properties in the gravitationally lensed merger HATLAS J142935.3-002836"
   Messias et al. MNRAS, 486, 2366 (2019)

6. "SOFIA/HAWC+ Detection of a Gravitationally Lensed Starburst Galaxy at z = 1.03"
   Ma et al. ApJ, 864, 60 (2018)

7. "Herschel and Hubble Study of a Lensed Massive Dusty Starbursting Galaxy at z 3"
   Nayyeri et al. ApJ, 844, 82 (2017)

8. "Spitzer Imaging of Strongly lensed Herschel-selected Dusty Star-forming Galaxies"
   Ma et al. ApJ, 814, 17 (2015)

9. "Lens Models of Herschel-selected Galaxies from High-resolution Near-IR Observations"
   Calanog et al. ApJ, 797, 138 (2014)

ABSTRACT OF THE DISSERTATION

Cosmology Through Einstein's Lens: Understanding Galaxy Structure and Evolution Using Strong Gravitational Lensing

By

Nicholas Timmons

Doctor of Philosophy in Physics

University of California, Irvine, 2019

Professor Asantha Cooray, Chair

Presented here are four studies in which the strong gravitational effect is used as a tool in studying the physical properties and environments of galaxies with an emphasis on dusty star-forming galaxies at high redshifts. The first chapter contains an introduction to the dissertation. In the second chapter we present Hubble Space Telescope (HST) WFC3 imaging and grism spectroscopy observations of the *Herschel*-selected gravitationally-lensed starburst galaxy HATLASJ1429-0028. It is found that a combination of high stellar mass, lack of AGN indicators, low metallicity, and the high star-formation rate of HATLASJ1429-0028 suggest that this galaxy is currently undergoing a rapid formation. In chapter 3 we present a source-plane reconstruction of a *Herschel* and *Planck*-detected gravitationally-lensed dusty star-forming galaxy (DSFG) at $z = 1.68$ using *Hubble*, Sub-millimeter Array (SMA), and Keck observations. We present a lens model with source plane reconstructions at several wavelengths to show the difference in magnification between the stars and dust, and highlight the importance of a multi-wavelength lens models for studies involving lensed DSFGs. We find the ratio of star formation rate surface density to molecular gas surface density puts this among the most star-forming systems, similar to other measured sub-millimeter bright galaxies (SMGs) and local ultra-luminous infrared galaxies (ULIRGS). In chapter 4 we make use of FIRE-2 cosmological simulations in order to model the light coming from

sub-millimeter bright galaxies and quantify the effect of differential magnification. We compare the results to observation and find that there is a physical offset between the light coming from stars and the light radiated by dust in the simulated galaxies that is in agreement with observations. Having the source and lens be physically offset, having the lens be closer to the source than the observer and increasing the mass of the lens all contribute to a greater magnification of the stellar light vs. the dust emission intensifying the differential magnification effect. When deriving the physical properties of galaxies from model SEDs we find that the overall effect of differential magnification is an underestimation of the ratio of star-formation rate to stellar mass that is equivalent to the ratio of stellar magnification to dust magnification. In chapter 5 we measure the Cosmic Microwave Background (CMB) skewness power spectrum in *Planck*, using frequency maps of the HFI instrument and the Sunyaev-Zel'dovich (SZ) component map. We model fit the SZ power spectrum and CMB lensing-SZ cross power spectrum via the skewness power spectrum to constrain the gas pressure profile of dark matter halos. The gas pressure profile is found to be in agreement with existing measurements in the literature including a direct estimate based on the stacking of SZ clusters in *Planck*.

Chapter 1

Introduction

The science of cosmology is one of studying the origins of our Universe as well as piecing together the evolution of our Universe. Cosmology is asking questions of how did galaxies like our own Milky Way come to be? Are there other galaxies like our own? To pursue this knowledge we must look deep into the past to try to understand how galaxies once formed and changed over time. Thankfully, light travels at a finite speed and so the deeper we look into the Universe the farther back in time we look. We can see slices of our history just by knowing where to look. The distant Universe does not reveal itself so easy however, and astronomers must utilize every tool they can to find the answers to their questions. In this dissertation we discuss the power of gravitational lensing as a tool for probing distant past in order to understand the evolution of the Universe.

1.1 Gravitational Lensing

The distant Universe is extremely faint to even our most powerful telescopes with matters becoming worse as large swaths are shrouded in dust. In the mid-20th century astronomers

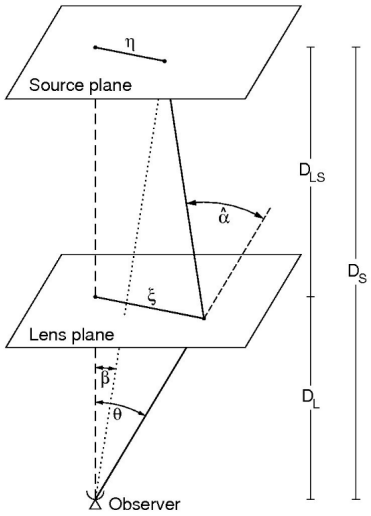

Figure 1.1: Typical Lens Configuration. Figure comes from Bartelmann & Schneider (2001)

devised a novel way of looking deeper into the reaches of space to reveal what was once hidden. Einstein's General Theory of Relativity claimed that light, which travels in a straight line, would have its direction deflected by the presence of a large gravitational potential. This was proven to be true by Eddington in 1919 when he observed the effect now known as gravitational lensing during a solar eclipse. This remarkable feat helped prove General Relativity to be true, make Einstein a household name as well as set the stage for future cosmologists to utilize the same principle.

From General Relativity Einstein derived the angle with which light would be deflected by a gravitational potential to be

$$\hat{\alpha} = \frac{4GM}{c^2 b} \tag{1.1}$$

where M is the mass of the deflecting object and b is the impact parameter. In practical use the deflecting object or "lens" will be extended. The typical configuration of a lensing

system is shown in Figure 1.1. The source is positioned in the source plane a distance D_s from the observer and the lens is modeled to be entirely in the lens plane a distance D_L from the observer. $\hat{\alpha}$ remains the angle with which an observer will see the light from the source deflected. The distribution of matter is given by the surface density

$$\Sigma(\xi) = \int \rho(\xi, z) dz \tag{1.2}$$

integrated over the line of sight. The deflection angle comes from the summed components of the mass

$$\hat{\alpha}(\xi) = \frac{4G}{c^2} \int \frac{(\xi - \xi') \sum \xi'}{|\xi - \xi'|} d^2\xi' \tag{1.3}$$

We define strong lensing as a case in which the surface density Σ exceeds a critical surface density Σ_{cr} where

$$\Sigma_{cr} = \frac{c^2}{4\pi G} \frac{D_s}{D_L D_{LS}} \tag{1.4}$$

Gravitational lensing can cause either convergence, the isotropic magnification or demagnification of an image, as well as the distortion of the image called shear. The measure of

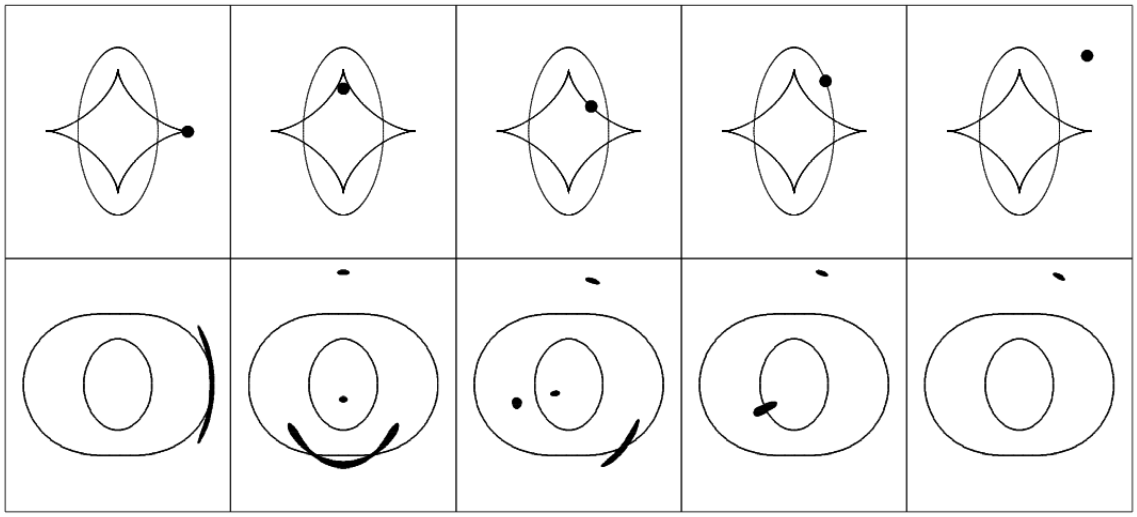

Figure 1.2: Different lens situations with a source being placed at different configurations with an elliptical lens. The top row shows the source and the caustic lines in the source plane while the bottom shows the resultant image and the critical lines. Large arcs and multiple images are possible as the source falls close to or within the caustics.Bartelmann & Narayan (1995)

convergence in the source plane κ is equivalent to $2\Sigma/\Sigma_{cr}$. The shear component γ is derived from the 3D Newtonian potential and the total equation for magnification μ is given by

$$\mu = \frac{1}{(1-\kappa)^2 - \gamma^2} \tag{1.5}$$

The points in which the magnification goes to infinity are called critical lines in the lens plane and caustic lines in the source plane. At these critical lines the image becomes stretched tangentially and strongly distorted.

Figure 1.2 shows different resultant images of a source being placed near to the caustic lines of an elliptical lens. In the case of strong gravitational lensing multiple images and elongated arcs are observed. The magnification caused by lensing is the key to using the effect as a tool in cosmology. The law of conservation of surface brightness ensures that the magnified

object will appear to have the same brightness per area while the area has been enlarged due to convergence. The key result is that the object will have its signal boosted by convergence as well as the spatial resolution of the image is increased.

1.2 Gravitational Lensing and Dusty Star-Forming Galaxies

Dusty star-forming galaxies (DSFGs) represent some of the most extreme cases of star-formation in our Universe (see review by Casey, Narayanan, & Cooray (2014)). With infrared luminosities $L_{\rm IR} \sim 10^{12} - 10^{13}$ $L_\odot$, implying star-formation rates (SFRs) in excess of 200 $M_\odot$ yr^{-1} with a subset of DSFGs being those that are bright in sub-millimeter wavelengths or sub-millimeter galaxies (SMGs) having SFRs $\sim$ $10^3 M_\odot$ yr^{-1} in starbursting phases (Greve et al., 2005; Tacconi et al., 2006, 2008; Riechers et al., 2011; Magnelli et al., 2012; Toft et al., 2014). They could make up as much as 20-30% of the star-formation rate density at z = 2 (Chapman et al., 2005; Casey et al., 2013).

SMGs have been shown to be massive $M_\odot \sim 10^{11} M_\odot$, with high gas and dust content, as well as metal rich $Z \sim Z_\odot$ (Greve et al., 2005; Magnelli et al., 2012; Michałowski et al., 2010b, 2016; Hainline et al., 2011; Swinbank et al., 2004) and undergoing a rapid assembly due to the star-formation and gas consumption that might make them the progenitors of today's massive elliptical galaxies (Lilly et al., 1999; Swinbank et al., 2006; Lapi et al., 2011; Fu et al., 2013).

There is still a fair amount that is unclear about SMGs and DSFGs in general. One example being the process by which they form. It is possible that they could have formed in gas-rich mergers (Tacconi et al., 2006; Engel et al., 2010) or that they are just extreme versions of normal star-forming galaxies which have grown through the smooth infall of gas (Dekel et al.,

2009; Davé et al., 2010). Studying SMGs is difficult due to their being dust obscured as well as being faint in shorter wavelengths.

Thankfully, gravitational lensing can be utilized to identify and study galaxies that otherwise would be too faint for observations. The signal boost that comes with the magnified image coupled with the high luminosity in longer wavelengths as a result of the UV light from hot young stars being absorbed and re-radiated out at long wavelengths by the dust have allowed large area far-infrared and sub-millimeter surveys, for example, the *Herschel*-Astrophysical TeraHertz Large Area Survey (H-ATLAS) (Eales et al., 2010), to efficiently select gravitationally lensed high-z dusty star-forming galaxies (e.g., Negrello et al. 2007, 2010; González-Nuevo et al. 2012; Wardlow et al. 2013; Bussmann et al. 2013; Nayyeri et al. 2016).

With the increased spatial resolution that comes with gravitational lensing, studies have been conducted, with the help of robust lens modeling, to understand the spatial extent and structure of these extreme star-forming galaxies (see, Ivison et al. 1998; Frayer et al. 1999; Riechers et al. 2011; Gavazzi et al. 2011; Swinbank et al. 2011; Bussmann et al. 2012; Fu et al. 2012, 2013; Messias et al. 2014; Nayyeri et al. 2017a).

1.3 Lensing and the Cosmic Microwave Background

Beyond individual galaxy studies, gravitational lensing has proven extremely useful in a wide variety of cosmological studies. The Cosmic Microwave Background Radiation (CMB) is made up of photons that were freed during the time of recombination. Throughout the journey of these early photons they interact with matter and dark matter alike being deflected by the large gravitational potentials. The light can be lensed by dark matter halos, the distribution of which can be measured by looking at temperature gradients in the CMB

maps from satellites such as the *Planck* mission (Planck Collaboration et al., 2011a). Two first order the differences in the temperature maps, or anisotropies, which trace the dark matter potentials gives observers a wealth of information about our current cosmology models (Planck Collaboration et al., 2016a). Of interest to this work are second order anisotropies which come about from other effects like the Sunyaev-Zel'dovich (SZ) effect (Sunyaev & Zeldovich, 1980) and integrated Sachs-Wolfe effect (ISW) (Sachs & Wolfe, 1967). The amplitude of the non-Gaussian signals arising from secondary effects can help constrain physical properties of the large scale structure of the Universe.

The following dissertation is organized as follows: In Chapter 2 we discuss the physical properties derived by observing a DSFG that is strongly lensed by a foreground galaxy. In Chapter 3 we discuss a DSFG that has been lensed by a galaxy cluster using a multi-wavelength lens model and spectral energy distribution to model physical properties of the galaxy in question. In Chapter 4 we look at the effect of differential lensing on simulated galaxies when compared to observed SMGs and quantify the amount that differential lensing effects derived properties. In Chapter 5 we step back and look at the cross-correlation between the squared temperature map and the SZ map from *Planck* and use the result to model the gas pressure profile of galaxy clusters across a wide range of masses and redshifts. Chapter 5 is followed by a bibliography.

Chapter 2

A Herschel-selected lensed dusty starburst at z=1.027

We present Hubble Space Telescope (HST) WFC3 imaging and grism spectroscopy observations of the *Herschel*-selected gravitationally-lensed starburst galaxy HATLASJ1429-0028. The lensing system consists of an edge-on foreground disk galaxy at $z = 0.218$ with a nearly complete Einstein ring of the infrared luminous galaxy at $z = 1.027$. The WFC3 spectroscopy with G102 and G141 grisms, covering the wavelength range of 0.8 to 1.7 μm, resulted in detections of Hα+[NII], Hβ, [SII], and [OIII] for the background galaxy from which we measure line fluxes and ratios. The Balmer line ratio Hα/Hβ of 7.5 ± 4.4, when corrected for [NII], results in an extinction for the starburst galaxy of $E(B-V) = 0.8 \pm 0.5$. The $H\alpha$ based star-formation rate, when corrected for extinction, is 60 ± 50 M$_\odot$ yr^{-1}, lower than the instantaneous star-formation rate of 390 ± 90 M$_\odot$ yr^{-1} from the total IR luminosity. We also compare the nebular line ratios of HATLASJ1429-0028 with other star-forming and sub-mm bright galaxies. The nebular line ratios are consistent with an intrinsic ultra-luminous infrared galaxy with no evidence for excitation by an active galactic nucleus (AGN). We estimate the metallicity, $12 + log(O/H)$, of HATLASJ1429-0028 to be 8.49 ± 0.16. Such a

low value is below the average relations for stellar mass vs. metallicity of galaxies at $z \sim 1$ for a galaxy with stellar mass of $\sim 2 \times 10^{11}$ $M_\odot$. The combination of high stellar mass, lack of AGN indicators, low metallicity, and the high star-formation rate of HATLASJ1429-0028 suggest that this galaxy is currently undergoing a rapid formation.

2.1 Background

Dusty star-bursting galaxies, especially those that are identified at far-IR/sub-mm wavelengths, have infrared luminosities $L_{\rm IR} \sim 10^{12} - 10^{13}$ $L_\odot$, implying star-formation rates (SFRs) in excess of 200 $M_\odot$ yr^{-1} (see review by (Casey, Narayanan, & Cooray, 2014)). As a primary contributor to the cosmic far-IR background, a significant fraction of cosmic star formation and metal production could have occurred in these star-bursting galaxies. Due to deep and wide surveys with the *Herschel* Space Observatory (Pilbratt et al., 2010), we now have large samples of dusty, star-burst galaxies at $z > 1$. Despite large number statistics our knowledge on the physical processes within such galaxies is still limited.

Traditional studies at optical and IR wavelengths involving nebular lines to probe the interstellar medium (ISM) of these dusty starbursts are challenging due to high dust extinction. One way to overcome this limitation is to make use of the flux magnification provided by gravitational lensing. Sub-mm surveys provide an efficient way to select lensed high-redshift galaxies due to the negative K-correction of the thermal dust spectral energy distribution (SED) and the steep faint-end slope of the sub-mm source counts (Blain, 1996). The two large area surveys, *Herschel*-ATLAS (Eales et al., 2010) and HerMES (Oliver et al., 2012), have resulted in sufficiently large samples of lensed galaxies (Negrello et al., 2010; Wardlow et al., 2013; Bussmann et al., 2013) from which we can find interesting targets for detailed follow-up observations.

Here we present results on the rest-frame optical spectroscopy of a lensed starburst galaxy to study its nebular line emission and line ratios. We make use of the *Hubble* Space Telescope Wide Field Camera 3 (HST/WFC3) grisms for these observations. To detect both Hα and Hβ over the wavelength covered by WFC3 grisms we require lensed galaxies to be at $z < 1.6$. One feasible target for WFC3 grism observations from currently known lensed *Herschel* sources is HATLASJ142935.3-002836 (Messias et al., 2014) (H1429-0028; G15v2.19 in Calanog et al. (2014)). The lensed galaxy was detected in the GAMA-15 field of *Herschel*-ATLAS (Eales et al., 2010) with $S_{160\,\mu m}$=$1.1 \pm 0.1 Jy$. The lensing models of the system using KeckII/NIRC2 laser guide star adaptive optics image and high-resolution ALMA imaging data are presented in Calanog et al. (2014) and Messias et al. (2014). The system includes a foreground edge-on disk galaxy (z = 0.218) with a near complete Einstein ring (Fig. 2.1). The lens model in Messias et al. (2014) shows that H1429-0028 is comprised of two components with a mass ratio of $(1 : 2.8^{+1.8}_{-1.5})$. The two components have been used to suggest H1429-0028 may be undergoing a galaxy merger, but the two components of H1429-0028 are found to lie on top of each other. This also leaves the possibility that the compact bright component of H1429-0028 is a starbursting clump or a region within a galaxy. The full extent of the galaxy is traced by the extended component that is gravitationally lensed to an Einstein ring (Fig. 2.1). The background source is at z = 1.027 with a total magnification factor of $\mu = 7.9 \pm 0.8$ at infrared wavelengths (Messias et al., 2014). The K-band (AB) magnitude of H1429-0028 is 18.2 (Calanog et al., 2014) and is at the level that allows grism observations with just one or two HST orbits.

Here we report HST/WFC3 grism spectroscopic observations of H1429-0028 making use of G102 and G141 grism filters, covering the wavelength range of 0.8 to 1.7 μm. At the redshift of H1429-0028 these observations probe the rest-frame wavelength range of 0.4-0.8 μm allowing us to measure several photoionization emission lines. We use these measurements to explore the properties of this system in terms of several emission line diagnostic diagrams. We also establish the gas-phase metallicity in a star-forming galaxy. The chapter

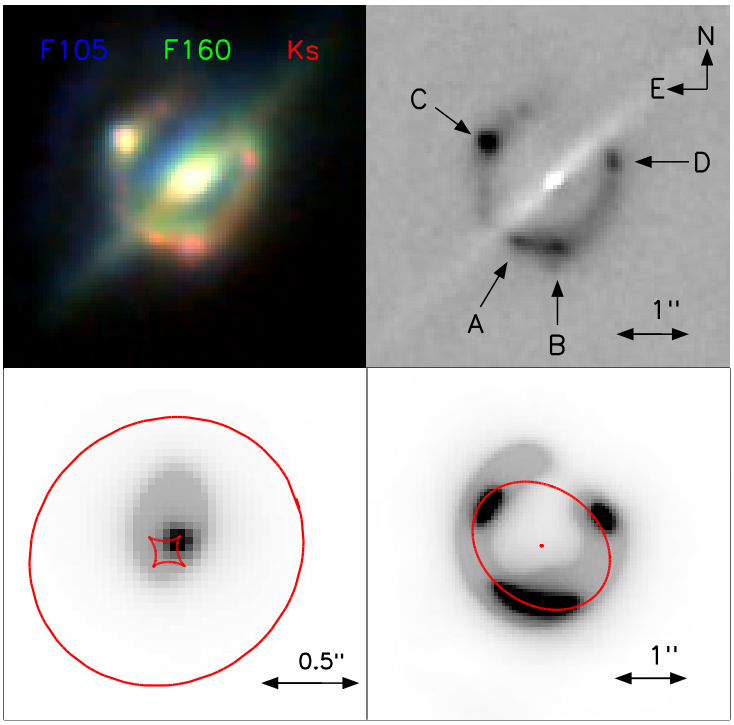

Figure 2.1: *Top Left:* The three color image of the gravitationally lensed system HATLASJ1429-0028 (also G15v2.19 in Calanog et al. (2014)) using WFC3/F105W (blue), F160W (green), and KeckII/NIRC2-LGS K_s (red) imaging data. *Top Right:* The foreground lensing galaxy was modeled using GALFIT (Peng et al., 2002) and then subtracted from the K_s-band imaging data. We label the bright knots following the scheme that was presented in Messias et al. (2014). *Bottom Left:* Source plane reconstruction showing the two components of HATLASJ1429-0028 and the caustic curves. *Bottom Right:* Image plane reconstruction showing the lens model and the critical curve. Note that the bright features A, B, C and D are from the bright compact source near the inner cusp caustic while the diffuse ring is due to the extended source.

is organized as following: In Section 2.2 we describe the observations and our data reduction procedure. In Section 2.3 we present our results related to emission lines and emission line flux ratios and discuss them in the context of existing studies in the literature. We conclude with a summary in Section 2.4. When calculating luminosities we make use of the standard flat-ΛCDM cosmological model with H_0= 70 km s^{-1} Mpc^{-1} and Ω_Λ=0.73.

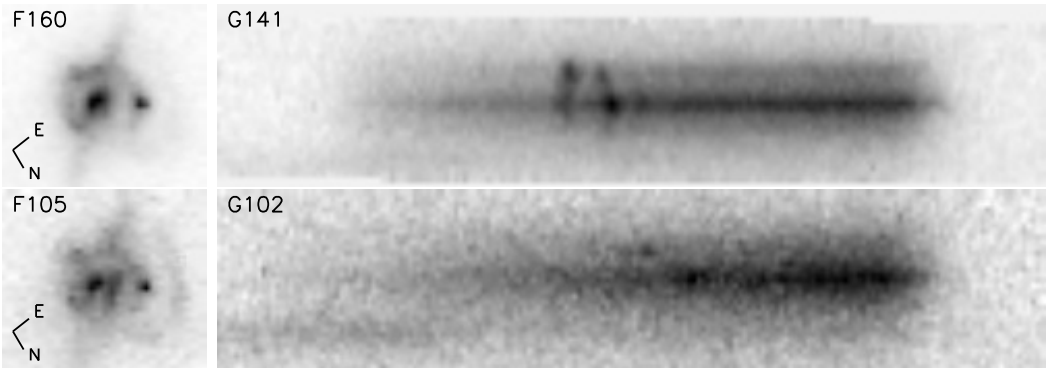

Figure 2.2: *Left:* The direct image in each of the WFC3 imaging filters oriented along the dispersion direction of the grism. *Right:* The two-dimensional grism images of H1429-0028. The top panel shows G141 and F160W images while the bottom panel shows G102 and F105W images. The upper trace contains the signal from knots A+B while the lower trace contains the signal from knot C as well as from the foreground lens.

2.2 Observations

HST/WFC3 observations of H1429-0028 were completed with two orbits under GO program 13399 in Cycle 21 (PI:Cooray). We obtained a total of five exposures, including two direct images and three grism observations in two filters. The two direct images made use of WFC3/F160W and F105W filters for a total of 250 and 350 seconds, respectively. We obtained G102 and G141 grism observations over 1800 and 2900 seconds, respectively. The G141 grism covers 1.0 to 1.8 μm, while G102 grism covers 0.7 to 1.2 μm. At $z = 1.027$ these observations then allow important emission line studies of H1429-0028 involving Hα at 1.33 μm, Hβ at 0.985 μm, [OIII] at 1.015 & 1.005 μm, and [SII] at 1.364 & 1.361 μm. Due to the low spectral resolution of order 80 Å the data do not resolve the [SII] doublet or Hα from [NII].

We made use of the calibrated HST imaging and grism data from the CALWF3 reduction pipeline, as provided by the Space Telescope Science Institute. The spectra for individual objects in the image were extracted with the aXe software package (Kümmel et al., 2009). Briefly, we created an object catalog making use of the broad-band F160W and F105W images with the SExtractor package (Bertin & Arnouts, 1996). A sky background sub-

traction was performed on the direct as well as the grism images. The core aXe marks spectral regions for each object in the SExtractor catalog, estimates contamination from nearby sources, and flat fields each of those regions or beams. A two-dimensional stamp of each grism beam is generated and then combined together with multiple observations of the same stamp to create a final two-dimensional image for scientific analysis. The data products include the two-dimensional combined grism stamp for each object as well as flux-calibrated one-dimensional spectra, contamination estimates, and error estimates.

We identified emission lines in the one-dimensional spectra using the known redshift of $z = 1.027$ for H1429-0028. We made use of custom IDL scripts as well as the Pyraf task SPLOT with ICFIT to extract the emission line flux densities and their errors from the one-dimensional spectra. To account for the contamination from the foreground lensing galaxy, we also model a continuum and account for the contamination in our line flux densities. Detailed lens modeling of H1429-0028 in four bands have shown clear evidence for differential magnification. For the rest-frame optical observations as is the case for our data the appropriate magnification is 7.9 ± 0.8 (Messias et al., 2014).

2.3 Results

In order to derive extinction corrections and line ratios, we measure the line intensities for detected bright regions of H1429-0028. In Fig. 2.1 we label the bright components following the scheme of Messias et al. (2014). In the G141 grism the brightest component C and (A+B) as well as parts of the Einstein ring had clear emission detections. For G102 only components (A+B) had a detectable [OIII] as well as Hβ. In G102 component C had clear detection of the [OIII] lines but only an upper limit on the Hβ line. Given the ratio of Hα to Hβ in knots (A+B), and the detected value of Hα in knot C, the expected value of Hβ in knot C is $\sim 3.2 \pm 1.9 \times 10^{-17}$ erg $s^{-1}cm^{-2}$. We measured the Hβ line flux density to be

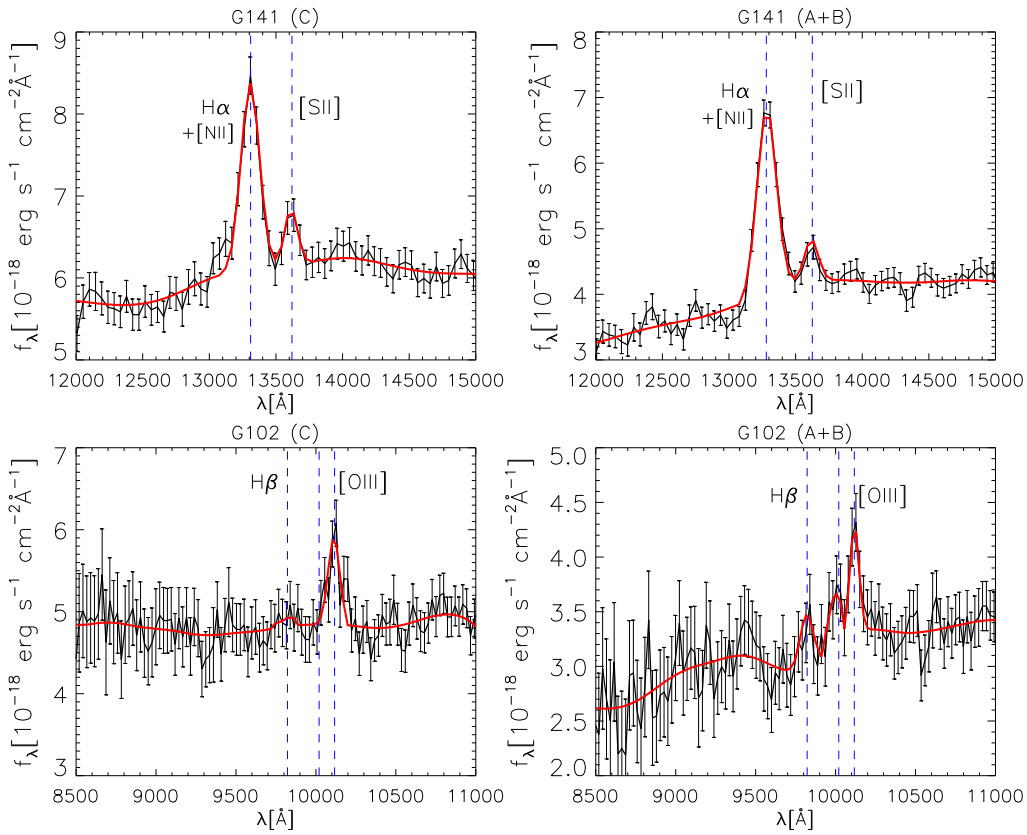

Figure 2.3: The extracted one-dimensional spectra showing the regions of detected emission lines We separate these detections to different knots identified in Fig. 2.1, mainly knot C, brightest of the features, and the combination of knots A+B. The spectra from knot C are plotted on the left while the spectra from knots A+B are plotted on the right. Emission lines from knot D were undetected or confused with the continuum emission from the foreground lensing galaxy in the dispersion direction of the two grism observations.

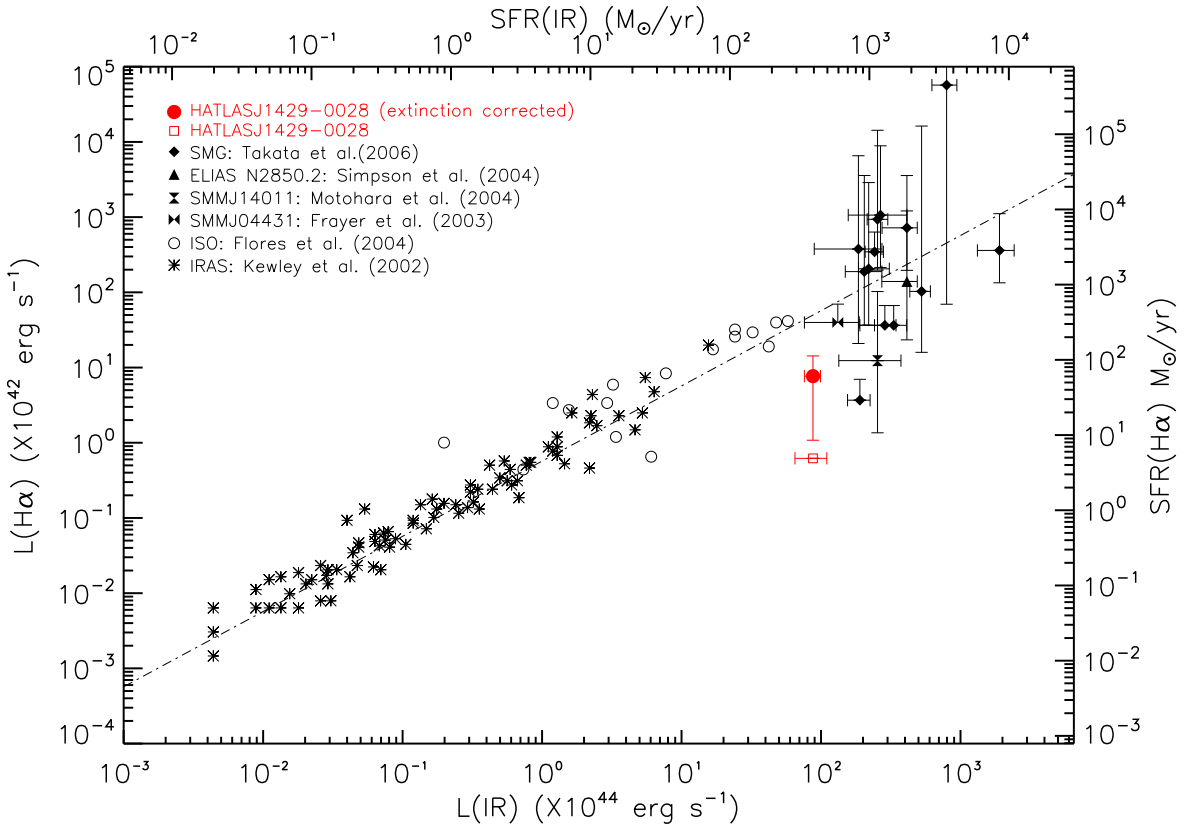

Figure 2.4: Hα luminosity vs. Far-infrared for H1429-0028 compared to the extinction corrected sample of IR luminous and sub-mm galaxies in Takata et al. (2006). For reference we also show the corresponding SFRs based on IR luminosity and Hα luminosity to the top and left of the plot, respectively. We show H1429-0028 for two cases with and without extinction correction of Hα luminosity. The dot-dashed line represents the case that SFRs from Hα and far-infrared are equal. H1429-0028 falls below this trend line but the difference between IR and Hα-based SFRs is fully consistent with the observed scatter of previous measurements.

Table 2.1: Emission Lines

Line	Component	Flux[1]	Eq. Width[2] ($\mathring{A}$)
Hα+[NII]	(A+B)	45.8 ± 2.3	108.4 ± 5.4
Hα+[NII]	(C)	32.9 ± 2.6	52.4 ± 4.2
Hβ	(A+B)	4.5 ± 2.6	15.1 ± 8.8
Hβ	(C)	1.4 ± 3.8	2.9 ± 8.0
[OIII]λ(5007)	(A+B)	6.4 ± 1.8	18.8 ± 5.2
[OIII]λ(4959)	(A+B)	4.1 ± 1.9	12.6 ± 5.9
[OIII]λ(5007+4959)	(C)	10.8 ± 2.2	22.6 ± 4.7
[SII](doublet)	(A+B)	10.1 ± 1.8	23.7 ± 4.2
[SII](doublet)	(C)	8.7 ± 2.1	14.1 ± 3.4

[1] Line fluxes are in 10^{-17} erg s^{-1} cm^{-2}, not corrected for lens magnification.
[2] Equivalent widths should be considered as an upper limit due to potential systematic uncertainties in the background continuum model.

$1.4 \pm 3.8 \times 10^{-17}$ erg $s^{-1}cm^{-2}$. This value falls within the estimated range but is not robust enough to be used for scientific analysis.

From Fig. 2.1 the lens models suggest two components for H1429-0028, one that is compact and bright and a second that is extended. The two components have effective radii of 0.18"$\pm$0.01 and 0.03"$\pm$0.01, for the source responsible for the ring and for knots, respectively. It is clear from the lensing models that the quadruply imaged knots A to D are from the same source. While it has been suggested that H1429-0028 is a merger, due to the presence of two components in the lens model, it is not clear from such a model if H1429-0028 is two separate galaxies or if the smaller component is a high star-forming region within a galaxy. Our spectral line data do not have the adequate velocity resolution but in the future this question can be addressed with an integral field unit (IFU) observations. In this work, for the line ratios, we only study the ratios of bright knots. Thus our line ratios capture the physical properties within the starbursting compact region or a compact galaxy. For the total Hα flux we add the flux from each component with their corresponding magnification from the lens

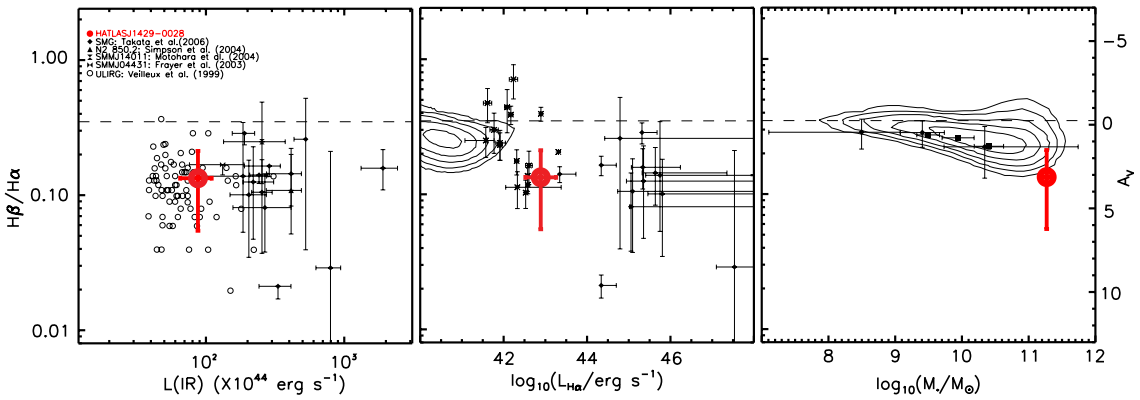

Figure 2.5: *Left:* Balmer decrement vs. IR luminosity. The background data are from Takata et al. (2006). *Middle:* Balmer decrement vs. Hα luminosity. The stars come from Domínguez et al. (2013) and the diamonds are from Takata et al. (2006). The contours show the galaxy population traced by SDSS. *Right:* Balmer decrement vs. galaxy stellar mass. The contours show the galaxy population traced by SDSS. The diamonds correspond to star-forming galaxies of $0.75 \leq z \leq 1.5$ presented in Domínguez et al. (2013), while the squares correspond to $z \sim 2$ from Sobral et al. (2012). We show the expected optical attenuation A_V to the right of the right panel for corresponding values of H_β/H_α.The dashed line represents the intrinsic value of the Balmer decrement.

model. The values are a magnification factor of $\mu \sim 27$ for the compact component, which contributes to the bright knots, and $\mu \sim 10$ for the larger component which contributes to the ring. We scale the observed line flux to a total estimate of the line intensity across the galaxy based on K-band photometry of the bright components and the diffuse rings. This correction results in a factor of 2.6 ± 0.1 from the line fluxes measured for the sum of the components A+B+C to the galaxy as a whole assuming that the continuum fluxes detected for the other components and ring scale as the rest-frame optical magnitudes.

To correct for the [NII] contamination of Hα we make use of two independent methods to derive the expected [NII]/Hα line ratio and average them as the final value to use here. This follows the approach given in Domínguez et al. (2013). The first method from Sobral et al. (2012) estimates the [NII]/Hα ratio using the Hα + [NII] equivalent width (EWs). Using the measured EWs we estimate the ratio to be 0.27 ± 0.07. However it could be that we are overestimating the EWs in our line fitting procedure due to systematic uncertainties associated with the model for the continuum, especially since the continuum is dominated

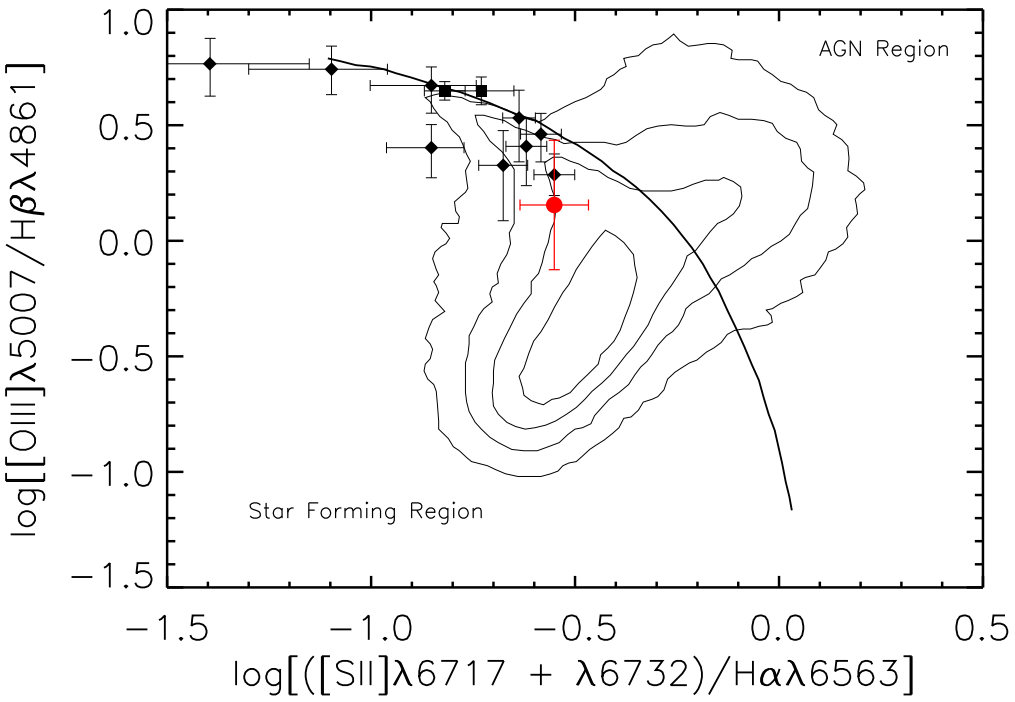

Figure 2.6: *Top:* BPT diagram with the black line separating the AGN and star-forming regions Kewley et al. (2001). The red point corresponds to H1429-0028, while the black points come from star forming galaxies in the redshift range $0.75 \leq z \leq 1.5$ from Domínguez et al. (2013) represented as diamonds and two $z \sim 2$ lensed star-forming galaxies from Hainline et al. (2009) represented as squares. The background contours show the galaxy population traced by SDSS Kewley et al. (2001) .

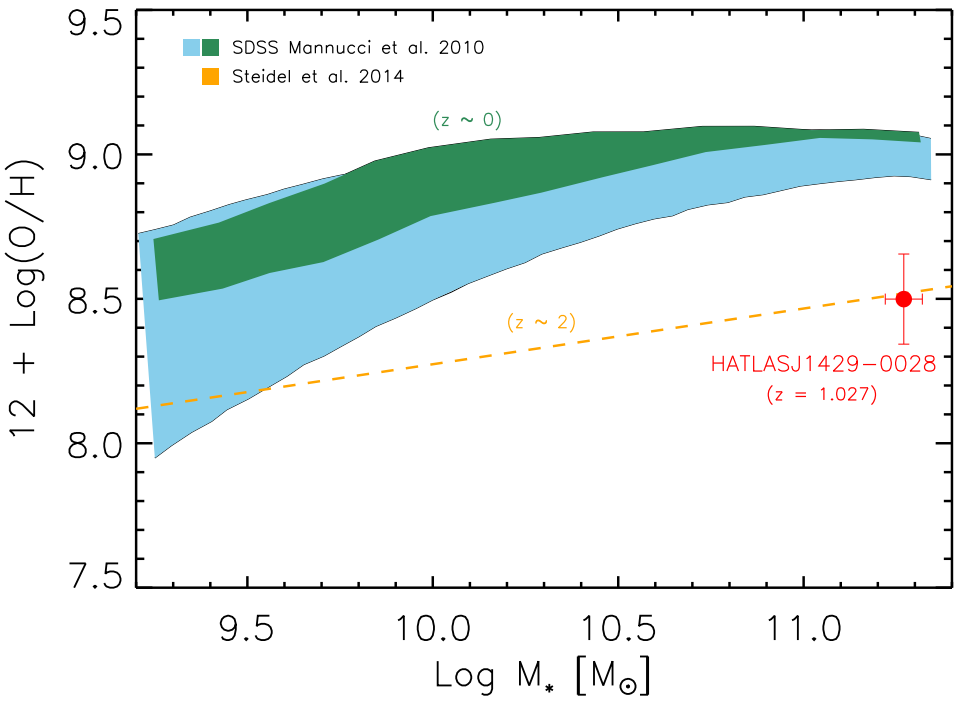

Figure 2.7: Metallicity vs. Stellar Mass. The green band represents local SDSS galaxies while the blue region represents a second order fit to SDSS extrapolated towards higher SFR (Mannucci et al., 2010). The orange dashed line representing $z \sim 2$ galaxies from Steidel et al. (2014). The calculated value of metallicity for H1429-0028 representing the O3N2 calculation using the O[III]/Hβ to N[II]/Hα ratio (Pettini & Pagel, 2004).

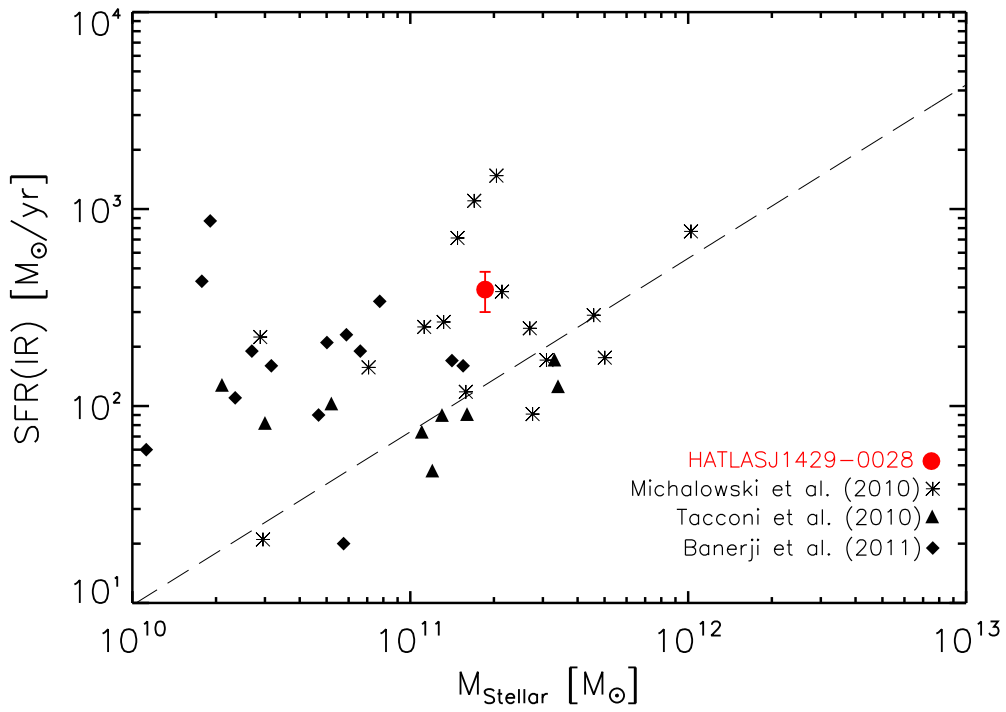

Figure 2.8: Star formation rate (based on the IR luminosity) vs. stellar mass. For comparison $z \sim 1$ SMGs from Michałowski et al. (2010a),Tacconi et al. (2010a), and Banerji et al. (2011) are shown. The dashed line shows the $z = 1$ main sequence relation (Elbaz et al., 2007).

by the residual fluxes from the foreground lensing galaxy. Thus we also employ a second method, but we find consistent estimates on the [NII]/Hα ratio.

The second method from Erb et al. (2006) relies on a relationship derived between stellar mass of a galaxy and the Hα/NII ratio of that galaxy. Here, instead of an independent estimate of the stellar mass, we make use of the SED modeling in Ma et al. (in prep) with a stellar mass of $1.9 \pm 0.02 \times 10^{11}$ M$_\odot$ derived from MAGPHYS. The resulting [NII]/Hα ratio is 0.27 ± 0.03. Both Sobral et al. (2012) and Erb et al. (2006) make use of the calibration method used in Pettini & Pagel (2004). The two estimates are consistent with each other. Note that the stellar mass we use is slightly lower than the value of $\sim 3 \times 10^{11}$ M$_\odot$ quoted by Messias et al. (2014). We prefer to use a revised value for the stellar mass using MAGPHYS models as we include new optical measurements of the SED and, as discussed later, we find consistent estimates on the extinction with SED modeling when compared to the estimates based on the Balmer line ratios.

For the values we discuss below we take the average ratio of [NII]/Hα from Sobral et al. (2012) and Erb et al. (2006) to be 0.27 ± 0.05. Once corrected for [NII] we find Hα/Hβ = 7.49 $\pm$ 4.4. Using this ratio we calculate the nebular extinction $E(B-V)$ following Momcheva et al. (2013) and find it to be 0.82 ± 0.50. Using Calzetti (2001), the corresponding optical depth τ_V is 2.93 ± 1.9. The extinction is lower than the τ_V value of $\sim 11.2^{+4.5}_{-3.2}$ for H1429-0028 in Messias et al. (2014), based on the broad-based SED model fitting using MAGPHYS. A revised model fit to H1429-0028 using new estimates of the background galaxy, including deblended IRAC data, finds $\tau_V \sim 4.2 \pm 0.4$ consistent with the estimate of τ_V from the Balmer line ratios (Ma et al. in prep).

In Fig. 2.4 we compare the extinction-corrected Hα luminosity of H1429-0028 with other star-forming galaxies. All data points from the literature (following Takata et al. 2006) are extinction corrected though we show the case for H1429-0028 with and without extinction correction. Though the apparent luminosity of H1429-0028 corresponds to that of a hyper-

luminous infrared galaxy with $L_{IR} \sim 10^{13}$ $L_{\odot}$, the intrinsic luminosity, once corrected for lensing magnification, is that of a ultra-luminous infrared galaxy (ULIRG). The galaxy falls between the SMGs and local ULIRGs studied by Swinbank et al. (2004) and Takata et al. (2006) with rest-frame optical spectroscopy at Keck and Subaru, respectively. We find the extinction-corrected SFR of H1429-0028, at 60 ± 50 $M_{\odot}$ yr^{-1}, to be lower than the instantaneous SFR implied by the total IR luminosity, with a value of 390 ± 90 $M_{\odot}$ yr^{-1} using the Kennicutt (1998) relation. Given the scatter observed in Fig. 2.4, however, we do not find this difference to be statistically significant.

In Fig. 2.5 we compare the Balmer decrement of H1429-0028 against Hα, IR luminosity, and stellar mass for a sample of galaxies. As shown in Fig. 2.5 middle panel, for the sample of galaxies with both Hβ and Hα measurements in the literature, we find that the extinction-corrected Hα luminosity of H1429-0028 to be among the highest. The Domínguez et al. (2013) sample comes from HST/WFC3 grism observations of $z \sim 0.75$–1.5 galaxies. The SDSS-detected star-forming galaxies have $L_{H\alpha} < 10^{42}$ ergs s^{-1}, while for H1429-0028 $L_{H\alpha} > 10^{43}$ ergs s^{-1}. This is consistent with the fact that H1429-0028 is an ULIRG. The right panel shows the trend in the Balmer decrement with the stellar mass such that there is a slight decrease in the Hβ to Hα ratio with an increase in the stellar mass. The plotted points are the sample-averaged values from Domínguez et al. (2013) as diamonds and Sobral et al. (2012) as squares in three stellar mass bins in both studies. These data mainly probe the stellar mass below a few times 10^{10} $M_{\odot}$. H1429-0028 is massive with $M_{\star} \sim 10^{11}$ $M_{\odot}$ and has a Balmer decrement that is lower than the typical star-forming galaxies in the same redshift range of 0.75 to 1.5.

In Fig. 2.6 we compare the line ratios of [OIII]/Hβ vs. [SII]/Hα. This is a variant of the more traditional BPT diagram (Baldwin et al., 1981) that involves [OIII]/Hβ vs. [NII]/Hα. Given that [NII] is blended with Hα in our low-resolution data we make use of [SII]/Hα ratio. We make extinction corrections for the [SII]/Hα ratio here given the two [SII] lines are

somewhat separated in wavelength from Hα. In this diagram H1429-0028 is consistent with the low metallicity end of the star forming regions although the ratios have large uncertainties associated with measurement errors. The measurements are incompatible with AGN regions of galaxies from SDSS data at $z < 0.3$. While H1429-0028 is luminous this is primarily due to gravitational lensing; the intrinsic luminosity of H1429-0028 is compatible with a galaxy star forming at a rate of 200 to 400 $M_\odot$ yr^{-1}. The lens models shown in Messias et al. (2014) are compatible with a merger system. Interestingly a value for [NII]/Hα of 0.27 ± 0.03 is higher than the average [NII]/Hα ratio of 0.19 ± 0.05 for the galaxies classified as star-forming in the SCUBA sample of Swinbank et al. (2004), and lower than the average for SMGs hosting AGN of 0.41 ± 0.05 from the same study.

In Fig. 2.7 we make use of the nebular line ratios, with the estimate of [NII]/Hα ratio, to make an estimate of the metallicity. Instead of an estimate based on [NII]/Hα ratio alone, we make use of the O3N2 ratio (Pettini & Pagel, 2004) as the estimator here as it also involves the measured [OIII]/Hβ ratio. The metallicity value, as measured in terms of $12+\log(O/H)$ was found to be 8.49 ± 0.16. In Fig. 2.7 we compare the metallicity vs. the stellar mass. The figure shows the average metallicity vs. stellar mass relations for both local (Mannucci et al., 2010) and $z \sim 2$ galaxies (Steidel et al., 2014). H1429-0028 has a metallicity comparable to galaxies at $z \sim 2$ despite being at $z = 1.027$. H1429-0028 has a high SFR, but shows no indication that it is hosting an AGN. H1429-0028 is metal poor despite its high stellar mass and argues for a scenario that it is still under a rapid formation phase.

Finally in Fig. 2.8 we show the location of H1429-0028 in comparison to the main sequence of galaxies at $z \sim 1$. Here we plot the total IR luminosity-based SFR of H1429-0028 vs. stellar mass. We find that H1429-0028 is above the $z = 1$ correlation from Elbaz et al. (2007). For comparison, we also show other dusty star-forming galaxies at $z \sim 1$ from the literature. Finally the average gas fraction $M_{ISM}/(M_\odot+M_{ISM})$ for the Tacconi et al. (2010a) sample of star-forming galaxies is 0.34%. The gas fraction for H1429-0028 is 0.25 ± 0.1%, where

we make use of the gas mass of $M_{ISM} = 4.6 \pm 1.7 \times 10^{10} M_{\odot}$ from ALMA CO observations reported in Messias et al. (2014).

H1429-0028 is one example of a grism observation with HST based on a galaxy that was first selected with the *Herschel* catalog as a lensed background source. Based on lensing models (Wardlow et al., 2013), we find that there should be roughly 0.25 deg^{-2} lensed starburst galaxies in the redshift interval of 1 to 2. In the future such galaxies will be automatically included as part of the surveys that will be done with slitless grisms on Euclid and WFIRST. In the 2000 deg^2 High Latitude Deep survey we expect WFIRST will detect close to 500 lensed starbursts at $z \sim 1$ to 3. The study we have presented for one lensed galaxy can then be expanded to a large enough sample for detailed statistical study that probes the internal structure of lensed starbursts.

2.4 Summary

We observed the *Herschel*-selected gravitationally-lensed starburst galaxy HATLASJ1429-0028, studied in detail in Messias et al. (2014) with some initial description in Calanog et al. (2014). We present Hubble/WFC3 G101 and G412 grisms of HATLASJ1429-0028. The observations covered the wavelength regime of 0.8 to 1.7 μm and resulted in detections of Hα+[NII], Hβ, [SII], and [OIII] for several bright regions of the background galaxy. The Balmer line ratio $H\alpha/H\beta$ of 7.5 ± 4.4, when corrected for [NII], results in an extinction for the starburst galaxy of $E(B-V) = 0.8 \pm 0.5$. The $H\alpha$ based star formation rate, when corrected for extinction, is at the level of 60 ± 50 M$_{\odot}$ yr^{-1}, lower than the star formation rate of 390 ± 90 M$_{\odot}$ yr^{-1} from the total IR luminosity. HATLASJ1429-0028 also has a low metallicity despite its high stellar mass at the level of 10^{11} M$_{\odot}$. The combination of high stellar mass, lack of AGN indicators, low metallicity, and the high star-formation rate of HATLASJ1429-0028 suggests that this galaxy is still going through a rapid formation.

Chapter 3

Multi-wavelength lens reconstruction of a *Planck* & *Herschel*-detected star-bursting galaxy

We present a source-plane reconstruction of a *Herschel* and *Planck*-detected gravitationally-lensed dusty star-forming galaxy (DSFG) at $z = 1.68$ using *Hubble*, Sub-millimeter Array (SMA), and Keck observations. The background sub-millimeter galaxy (SMG) is strongly lensed by a foreground galaxy cluster at $z = 0.997$ and appears as an arc of length $\sim 15''$ in the optical images. The continuum dust emission, as seen by SMA, is limited to a single knot within this arc. We present a lens model with source plane reconstructions at several wavelengths to show the difference in magnification between the stars and dust, and highlight the importance of a multi-wavelength lens models for studies involving lensed DSFGs. We estimate the physical properties of the galaxy by fitting the flux densities to model SEDs leading to a magnification-corrected star formation rate of 390 ± 60 $M_\odot$ yr^{-1} and a stellar mass of $1.1 \pm 0.4 \times 10^{11}$ $M_\odot$. These values are consistent with high-redshift massive galaxies that have formed most of their stars already. The estimated gas-to-baryon fraction, molecular

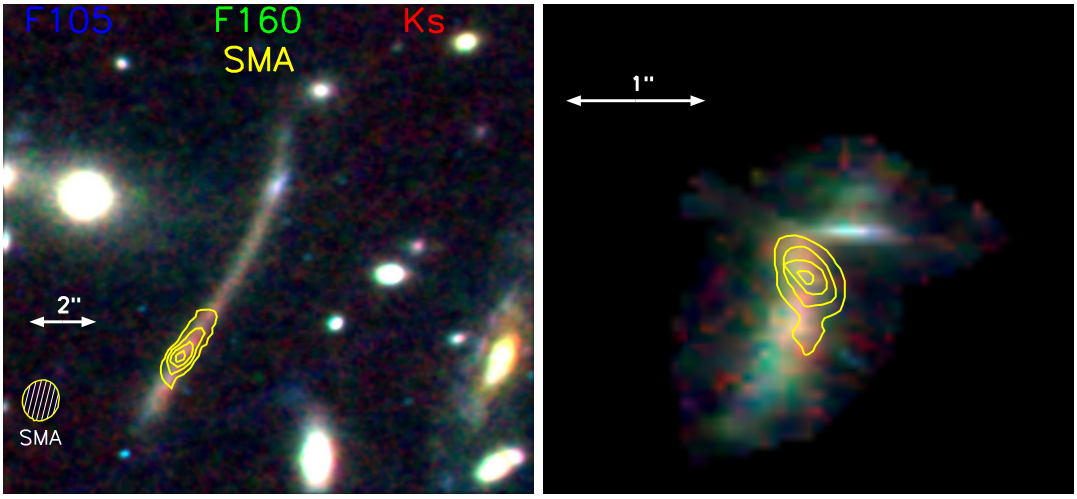

Figure 3.1: *Left:* Three color image of HATLAS J132427+284452 using *Hubble*/WFC3 F105W (blue) and F160W (green), and Keck NIRC2 K_s (red) bands with Submillimeter Array (SMA) 870 μm band emission contours are overlaid. The SMA contours are at 3σ, 6σ, 9σ and 12σ, where σ is the rms noise (0.6 mJy beam^{-1}). The dust emission, and thus the *Herschel* and primary *Planck* source, associated with the DSFG is concentrated in the area of the yellow contours while the optical emission extends over an arc of $\sim 15''$. For reference, we show the SMA beam in the bottom left. *Right:* Three color source plane reconstruction with SMA source plane contours overlaid with the same contouring steps as left (see Section 4 for the lens reconstruction). The spatial resolution of the reconstruction is $\sim 0.06\,''$ pixel^{-1} or ~ 0.5 kpc pixel^{-1}.

gas surface density, and SFR surface density have values of 0.43 ± 0.13, 350 ± 200 M$_\odot$ pc^{-2}, and $\sim 12 \pm 7$ M$_\odot$ yr^{-1} kpc^{-2}, respectively. The ratio of star formation rate surface density to molecular gas surface density puts this among the most star-forming systems, similar to other measured SMGs and local ULIRGS.

3.1 Background

In recent years, large area far-infrared and sub-millimeter surveys, for example, the *Herschel*-Astrophysical TeraHertz Large Area Survey (H-ATLAS) (Eales et al., 2010), have allowed the efficient selection of gravitationally lensed high-z dusty star-forming galaxies (DSFGs; e.g., Negrello et al. 2007, 2010; González-Nuevo et al. 2012; Wardlow et al. 2013; Bussmann

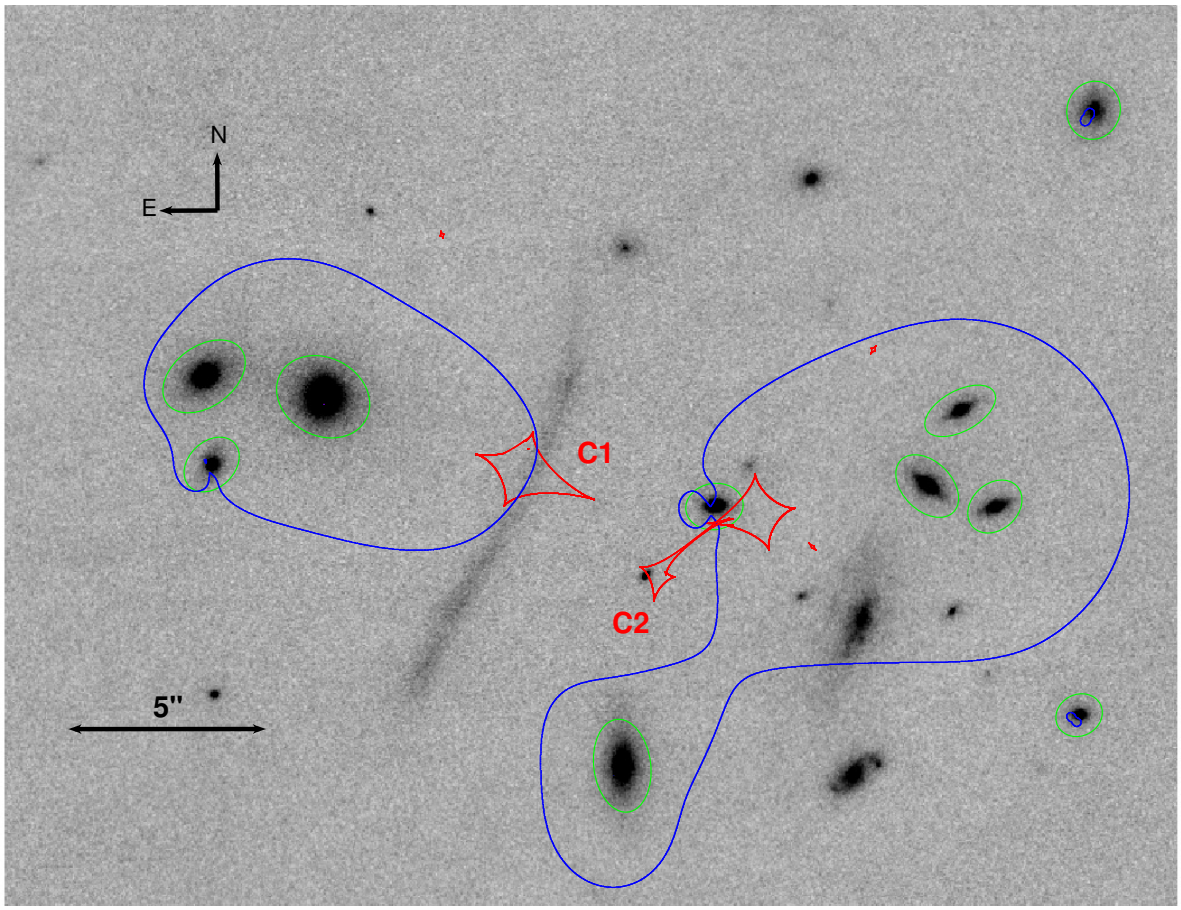

Figure 3.2: Keck/NIRC2 K_s-band image with the critical and caustic (C1 and C2) lines overplotted in blue and red, respectively. Circled in green are the foreground lens galaxies used in constructing the lens model. In addition to individual galaxies the lensing reconstruction requires extended potential associated with the two galaxy groups/clusters to the east and west of the lensing arc.

et al. 2013; Nayyeri et al. 2016). These DSFGs (see Casey et al. 2014 for a recent review) have star formation rates (SFRs) of $\sim 10^2$–10^3 $M_\odot$ yr^{-1}, with typical stellar mass of $\sim 10^{11}$–10^{12} $M_\odot$, and are generally found during the peak epoch of galaxy formation and evolution at $z \sim 1-4$. Such rapid star- formation has a short lifetime (< 0.1 Gyr) and is rare in the local Universe (Tacconi et al., 2010b). Luminous and ultra-luminous infrared galaxies (LIRGs and ULIRGS), of which DSFGs are an analog, contribute significantly ($\sim 70\%$) to the cosmic star formation at $z = 1$ (Le Floc'h et al., 2005). Recent studies have shown that DSFGs may differ from ULIRGs in that their star-forming regions may be more spatially extended (e.g., Younger et al. 2008; Ivison et al. 2011; Riechers et al. 2011). There is evidence to suggest DSFGs are likely an early stage of today's massive elliptical galaxies (e.g., Lilly et al. 1999; Swinbank et al. 2006; Lapi et al. 2011; Fu et al. 2013). DSFGs are usually faint at rest-frame optical wavelengths due to dust obscuration, but are bright in the rest-frame far-IR, making sub-mm surveys the perfect tool to study DSFGs (Negrello et al., 2010).

While wide area surveys with *Herschel* and ground-based instruments have increased the sample sizes of DSFGs at sub-mm wavelengths, due to limitations associated with existing instruments in sensitivity and spatial resolution, our ability to conduct detailed investigations on the physical properties of DSFGs has been severely hampered. Thankfully, strong gravitational lensing can be used to overcome these limitations. The flux amplification as a result of gravitational lensing allows for the detection of otherwise intrinsically fainter dust obscured galaxies and the associated spatial enhancement allows spatially resolved imaging observations with existing facilities (e.g., Fu et al. 2012; Messias et al. 2014).

H-ATLAS J132427.0+284452 (hereafter HATLAS J132427) peaks at 350 μm with a flux density of $\sim 380 \pm 8$ mJy (from *Herschel* Spectral and Photometric Imaging Receiver, SPIRE). It is also identified in the all-sky maps from *Planck* (Planck Collaboration et al., 2011b) as PLCKERC857 G047.32+82.53 (1.3 ± 0.15 Jy) at 857 GHz (350 μm) in the *Planck* Early Release Compact Source Catalog (ERCSC; Planck Collaboration et al. 2011b). Although

the *Planck* detected flux density is $\sim 4\times$ larger than *Herschel*/SPIRE measurement in H-ATLAS, the difference can be explained as due to the large 3-5 arcmin beam of *Planck* measurements which may cause blending in an over-dense field. Such a difference is also present in a previous *Planck*-detected H-ATLAS lensed source. H-ATLAS J114637.9-001132 (Fu et al., 2012) is detected by *Planck* with a flux density of $S_{350} = 2.1 \pm 0.8$ Jy but in *Herschel* the flux density is measured to be $S_{350} = 378 \pm 28$ mJy corresponding to a $\sim 5\times$ larger *Planck* flux density much like HATLAS J132427. Despite the *Planck* flux being uncertain the detection is validated through other observations and confirms *Planck*'s ability to detect the brightest lensed DSFGs (see Canameras et al. 2015).

In this chapter we present new *HST*, SCUBA2 and Keck observations of HATLAS J132427 along with previous multi-wavelength observations to create a complete profile of this *Planck* and *Herschel*-detected DSFG. In Section 3.2 we describe the observations and data reduction procedures. In Section 3.3 we describe previous and archival observations used in the analysis. In Section 3.4 we use high resolution imaging to construct a lens model and calculate the magnification factors. In Section 3.5 we model the spectral energy distribution (SED) and derive physical properties from the fit. In Section 3.6 we discuss the derived properties of HATLAS J132427 and compare them to other SMGs and DSFGs. We conclude with a summary in Section 3.7. Throughout we make use of the standard flat-ΛCDM cosmological model with H_0= 70 km s^{-1} Mpc^{-1} and Ω_Λ=0.73.

3.2 Observations

Early observations of HATLAS J132427 are presented in George et al. (2013). Here we present new Keck, SCUBA2, *Hubble*/WFC3 imaging data and *Hubble*/WFC3 grism observations. Figure 3.1 shows a three color image of the source using *HST* (F105W and F160W bands) and Keck (K_s band) imaging along with SMA contours overlaid to show the spatial

Table 3.1: Observed Properties

Parameter	Value
R.A., DEC	13:24:27.206 +28:44:49.40
$z_{\rm source}$	1.676 ± 0.001
$z_{\rm lens}$	0.997 ± 0.017

variations of the source at different wavelengths. Figure 3.2 shows Keck NIRC2 $K_{\rm s}$-band imaging with the critical and caustic lines used in the lens model.

3.2.1 Keck/NIRC2

We obtained a 1680 second exposure in H band with an airmass of 1.02 and a 3840 second exposure in $K_{\rm s}$ band with an airmass of 1.36 (PI: Cooray) on 4 February 2012 with the KeckII/NIRC2 instrument aided with the laser guide-star adaptive optics system (LGSAO; Wizinowich et al. 2006). The imaging observations made use of a pixel scale at $0.04''$ pixel^{-1} for both filters. Custom IDL scripts were used to reduce the data following the procedures in Fu et al. (2012, 2013) which includes a dark subtraction, bad pixel masking, background subtraction as well as flat-fielding. The $K_{\rm s}$-band image was flux calibrated using UKIDSS (Lawrence et al., 2007) K-band photometry. The H-band image was flux calibrated using a common set of bright stars detected in NIRC2 image and in the *Hubble*/WFC3 F160W band image.

3.2.2 Hubble/WFC3

Hubble/WFC3 observations of HATLAS J132427 were completed with three orbits under GO program 13399 in Cycle 21 (PI: Cooray). We obtained a total of ten exposures including two direct images (F105W and F160W) and eight grism observations. The F105W observation had a total exposure time of 453 seconds while the F160W observation had a total exposure time of 353 seconds. Six of the grism observations were taken with the G102 (800 nm–1150 nm) grism for a total exposure time of 5218 seconds. The remaining two grism observations were taken with the G141 (1075 nm–1700 nm) grism for a total exposure time of 2406 seconds.

We made use of the calibrated *HST* imaging and grism data from the CALWF3 reduction pipeline, as provided by the Space Telescope Science Institute [1]. The spectra for individual objects in the image were extracted with the aXe software package (Kümmel et al., 2009). The data products include the two-dimensional combined grism stamp for each object as well as flux-calibrated one-dimensional spectra, contamination estimates, and error estimates. Similar analysis and reduction steps for the other target, (HATLASJ1429-0028) in GO program 13399 in Cycle 21 are described in Timmons et al. (2015).

The top portion of Figure 3.3 shows the direct imaging for the F105W and F160W filters aligned so that the dispersion direction of the grism is horizontal. Figure 3.3 also shows the two-dimensional stamps for the two grism filters. The bottom portion of Figure 3.3 shows the extracted one-dimensional spectra for each grism filter with a close up view of the two-dimensional continuum shown as an inset. The 2D stamp and the 1D spectra come from the bright northern clump as can be seen in Figure 3.3. Only the northern clump had a detectable continuum that was not overly contaminated by other spectra in the field. This clump has been circled in blue in the F105W and F160W images in Figure 3.3. The expected

[1] www.stsci.edu/hst/wfc3/pipeline/wfc3_pipeline

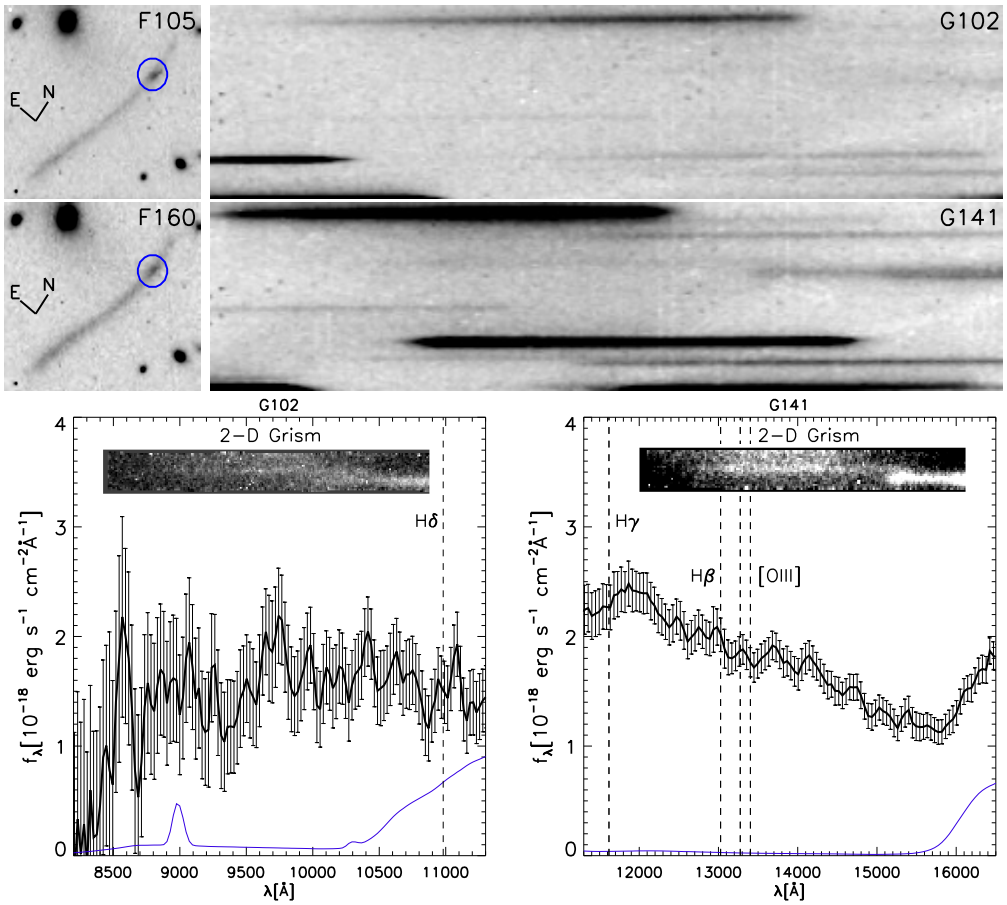

Figure 3.3: *Top Left:* The direct image in each of the WFC3 imaging filters oriented so that the dispersion direction of the grism is horizontal. *Top Right:* The two-dimensional grism images of HATLAS J132427. The top panel shows G102 and F105W images while the middle panel shows G141 and F160W images. *Bottom:* The extracted 1D spectra from the G102 and G141 slit-less spectra. The blue line is the estimated contamination coming from other spectra in the field. The 2D grism stamps are inlayed with vertical lines corresponding to useful emission lines over-plotted. Despite the presence of continuum emission no emission lines were detected. Due to contamination from other spectra in the field only the bright northern clump which has been circled in blue had an extractable continuum. It was not possible to extract a 1D spectrum from the southern clump associated with the radio detection.

emission lines at $z = 1.68$ are shown in the 1D spectra of Figure 3.3 and it is clear there is no significant line detection in either of the grism spectra, and so we cannot conduct line ratio diagnostics on HATLAS J132427. This is due to the low surface brightness of the galaxy compared to the source detected in Timmons et al. (2015) which involved bright multiply-imaged star-forming knots. Unfortunately, due to the overlapping grism spectra from nearby galaxies, we cannot integrate longer to improve the signal-to-noise of the spectrum from our target.

3.2.3 SCUBA2

This source, and the field around it, was observed by the SCUBA2 bolometer array camera on the JCMT (Holland et al., 2013). These observations were part of a broader program following up sources in the H-ATLAS survey (M13AU12, PI D.L. Clements). The observations of the field around HATLAS J132427 were made on 2013 April 8th and 12th using the standard pseudo-circular DAISY observing sequence for small and compact sources. This provides maps of a circular region of roughly 350 arcseconds in radius around the target position. The integration time in this field is a function of position, with the central regions receiving greater integration time than the outer regions. Five separate DAISY maps of HATLAS J132427 were made, three on April 8th, two on April 12th. The conditions for these observations were rated grade 3, indicating $\tau_{225\mathrm{GHz}}$ 0.08 to 0.12. These conditions are adequate for 850 μm observations but not for good 450 μm photometry.

The data were reduced in the standard manner using the SMURF software provided by the observatory. The SMURF iterative mapmaker *makemap* produced individual maps for each of the five subintegrations using the reduction recipe optimized for blank fields with corrections for atmospheric opacity. The five resulting maps were then combined using the mosaic tool to produce a final image which was then match filtered to optimize the S/N of

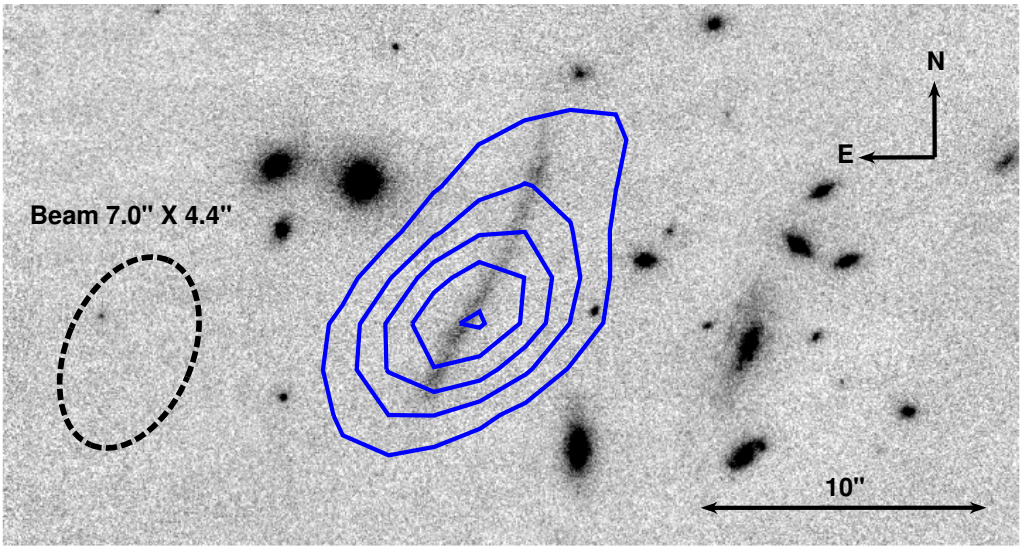

Figure 3.4: Keck/NIRC2 K_s-band image with CARMA contours overlaid. The contours are at 2σ, 4σ, 6σ, 8σ and 10σ, where σ is the rms noise (0.76 mJy beam^{-1}). For reference, we show the CARMA beam size and orientation.

unresolved sources. The final image was then trimmed to produce a 350 arcsecond radius field. The final map has a total integration time of 1850 s at its center, where HATLAS J132427 is located, falling to 450 s at the edges. HATLAS J132427 is detected at the centre of the final images with an 850 μm S/N ratio of $\sim$ 30 and a flux of 43 $\pm$ 1.2 mJy. It is interesting to note that five other 850 μm sources are detected at $> 4\sigma$ in the final map, suggesting the presence of a moderate over-density of sub-mm sources around HATLAS J132427.

3.3 Previous and Archival Observations

HATLAS J132427 was first reported as a candidate strongly lensed giant arc at optical wavelengths in Gladders et al. (2003) and its discovery and follow-up as a bright source in Herschel data is discussed in George et al. (2013). The following is a summary of previous or archival observations that were used for the present analysis. The flux densities are shown in Table 2.

Herschel Photoconductor Array Camera and Spectrometer (PACS) (Poglitsch et al., 2010) data at 100 μm and 160 μm were collected as a part of the OT1 program (OT_RIVISON_1). The total integration time of 360 s reaching $\sigma \sim 10$ mJy for 100 μm and $\sigma \sim 12$ mJy for 160 μm. *Herschel*/SPIRE Fourier Transform Spectrometer (FTS) (Griffin et al., 2010) observations were completed on 2 August 2012. The wavelength coverage was $\lambda_{\rm obs} = 194 - 671$ μm and the total observing time was 3.8 h. The data resulted in the discovery of the bright [CII]/158 μm emission line with a peak flux density of ~ 0.8 Jy, allowing the redshift of $z = 1.68$ to be measured directly, for the first time, from far-infrared spectroscopy. While the PACS data are used for the SED analysis the FTS spectrum is not. It is shown in Figure 3.6 but is not used in the SED analysis due to the presence of the bright [CII]158 μm emission line.

As a part of program 2011B-S044, 870 μm imaging data were taken with the Submillimeter Array (SMA) (PI: Bussmann). The total integration time of 9.7 h was taken in the compact, extended, and very extended array configurations, with baselines of 20-400 m. 1924-292, a blazar, was utilized as a bandpass calibrator and Titan was used for the flux calibration (Bussmann et al., 2013). The effective beam size is $1.66''$ and the rms is 6 mJy beam^{-1}. The SMA continuum is shown in Figure 3.1 and is used in the lensing model.

The CO J$= 2 \rightarrow 1$ line ($\nu_{\rm rest} = 230.538$ GHz, $\nu_{\rm obs} = 86.0$ GHz at $z = 1.68$) was detected by the Combined Array for Research in Millimeter-wave Astronomy (CARMA; PI: Riechers). The observations were conducted on 23 November 2012 using the D configuration (11-146 m baselines). The beam size was $7'' \times 4.4''$ and a rms noise of 0.76 mJy beam^{-1}. The total on-source time was 2.3 h while two blazars 1310+323 and 0927+390 were used to derive the bandpass shape and for complex gain calibration. Figure 3.4 shows CARMA contours overlaid on the Keck/NIRC2 $K_{\rm s}$-band image.

The Canada-Hawaii-France Telescope (CFHT) was used to image HATLAS J132427 in both the z (925 nm) and r (640 nm) bands (PI: Yee). The integration times for the r and z

bands were 900 s and 600 respectively and the observations were carried out on 5 July 1999 (Gladders et al., 2003). These observations were used to measure $z = 0.9$ for the foreground cluster.

The Institut de Radioastronomie Millimetrique Plateau de Bure Interferometer (IRAM PdBI) was used to obtain 1.1 h of on-source time during November 2012 using six 15 m antennas with the D configuration. The frequency was set to 129.028 GHz. The CO $J = 3 \rightarrow 2$ line was detected at 3σ.The flux density measurement is used in the SED analysis.

HATLAS J132427 is detected by the Wide Field Infrared Survey Explorer (WISE) (Wright et al., 2010) in four bands ranging from 3.35 $\rightarrow$ 22.09 μm all used in the SED analysis (Table 2).

3.4 Lens Model

We make use of the program LENSTOOL (Kneib et al., 1996; Jullo et al., 2007) to reconstruct the lensed galaxy and to derive the magnification factors of HATLAS J132427. Using the *HST* F160W high resolution imaging data, the gravitational potentials contributing to this model are identified using SExtractor (Bertin & Arnouts, 1996) with their parameters being optimized by the Bayesian Markov chain Monte Carlo (MCMC) sampler used in LENSTOOL. For each image (F160W, F105W, $K_{\rm s}$, SMA) the whole arc is broken down into four ellipses of varying size and brightness which are created using measured elliptical sizes and flux densities from SExtractor. These ellipses are then passed through the LENSTOOL model to reconstruct the source plane image.

Figure 3.2 shows Keck/NIRC2 $K_{\rm s}$-band image, with the gravitational potentials used in the model circled in green, and the critical and caustic lines overlaid. From Gladders & Yee (2005) the cluster members used in the model are at photometric $z = 0.997 \pm 0.017$

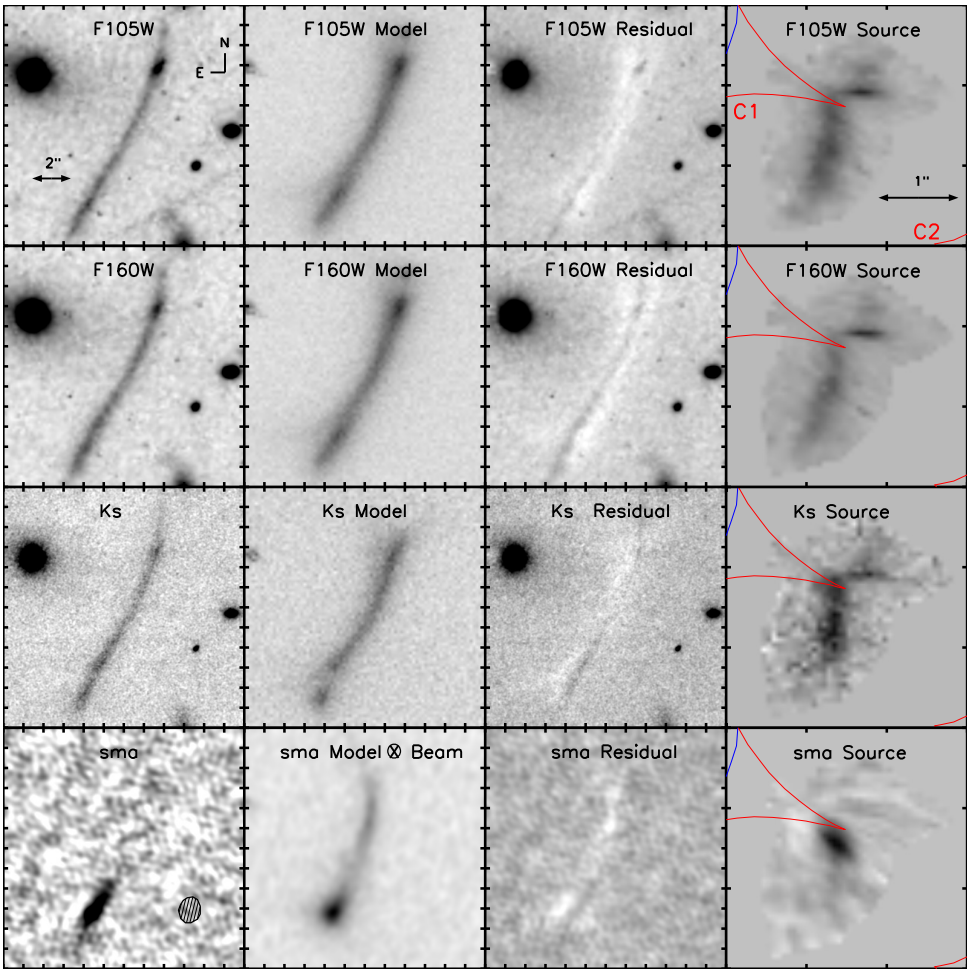

Figure 3.5: Lens modeling of HATLAS J132427 at several optical/infrared wavelengths and at 870 μm. *1st column:* The original imaging for the two *HST* bands, as well as Keck and SMA. The beam size and orientation is overlaid on the SMA frame. *2nd column:* Image obtained with the lens model for each band. The SMA model is convolved with a 2D Gaussian model of the SMA beam. *3rd column:* The residual obtained by subtracting the model from the original image. The scale is set to see the areas of over and under subtraction. *4th column:* The source plane reconstruction for each band, with the critical and caustic lines overlaid in blue and red, respectively. The C2 and C2 refer to the caustic lines as shown in Figure 3.2.

based on r and z band imaging. We assume a constant mass-to-light ratio and adopt a $0.5''$ uncertainty in the position of the critical lines which, corresponds to the thinnest part of the arc and should account for line-of-sight perturbations. The lens galaxies are modeled using a pseudo-elliptical isothermal mass density profile (PIEMD) (Kneib et al., 1996). To create the model the other sources in the field of unknown redshift were also placed at $z = 0.997$. There are a total of 26 galaxies used in the model, most of which are out of view in the figure and do not contribute significantly to the modeled potential. The cluster members which contribute the largest potential to the model are the galaxies which fall in the blue critical lines in the figure.

Compared with observations, models with multiply-imaged systems resulted in lenses that were too large and, thus, unrealistic. Therefore, a model assuming a singly imaged source was utilized. As a main constraint, we assumed that the central thin part of the arc was overlapping the critical line, as has been observed for some very elongated arcs (see the Clone arc in Jones et al. 2010). Placing the critical line closer to the arc results in increased stretching. The arc of HATLAS J132427 is very stretched, thus the critical line must overlap with the arc. However, the critical line cannot cross the arc, otherwise there would be two images.

Figure 3.5 shows the imaging for four bands F105W, F160W, $K_{\rm s}$ and SMA along with their model in the image plane, the residual and the source plane reconstruction. The long arc is detected in the near-IR bands, with the SMA flux only being detected above 3σ in the southern portion of the arc. The stellar portion of HATLAS J132427 corresponds to the large extended arc suggesting it has a higher magnification than the dust portion. The third column of Figure 3.5 shows the residual after subtracting the model from the image. It is clear that the model that LENSTOOL constructs does not perfectly describe the morphology and does leave residuals. Considering the lack of additional constraints to improve the overall

lens model, resulting from a singly-imaged source, we accepted that the current model is likely the best we can presently construct.

The best fit model gives $\mu_{\rm dust} = 4.9 \pm 1.8$ while the stellar magnification making up the extended arc is $\mu_{\rm stars} = 15.7 \pm 4.3$. In George et al. (2013) a magnification estimate for the molecular gas is derived following Harris et al. (2012) and Bothwell et al. (2013). Using the J= 1 $\rightarrow$ 0 luminosity and the FWHM, $\mu_{\rm Gas}$ is found to be $\sim$ 11. Due to the large uncertainty in the FWHM of the gas (e.g., 640 ± 270 km s^{-1}) the final estimate of the error for the derived value is $\pm$ 7 which is consistent with the magnification values found with the lens model used here. In Bussmann et al. (2013) a lens model for SMA using two galaxies instead of the two cluster components resulted in a magnification of 2.8 ± 0.4. The SMA data having just one image in Bussmann et al. (2013) made the model more difficult to constrain whereas the multi-wavelength model presented here includes SMA, Keck, *HST* etc. and can be considered a more complete model of the dust magnification.

3.5 Spectral energy distribution modeling

The spectral energy distribution (SED) of HATLAS J132427 was analyzed using the Multi-wavelength Analysis of Galaxy Physical Properties (MAGPHYS) software (da Cunha et al., 2008). The MAGPHYS package compares the observed flux density values to a library of model SEDs at the same redshift. Here we use the new HIGHZ model library of MAGPHYS SEDs, which was developed to interpret observations of SMGs from the ALESS survey (da Cunha et al., 2015), and should be more appropriate to fit the SEDs of DSFGs at high redshift.

The photometry for CFHT, *HST* and Keck were done using the SExtractor package (Bertin & Arnouts, 1996) using a flexible elliptical aperture to account for the elongated nature of

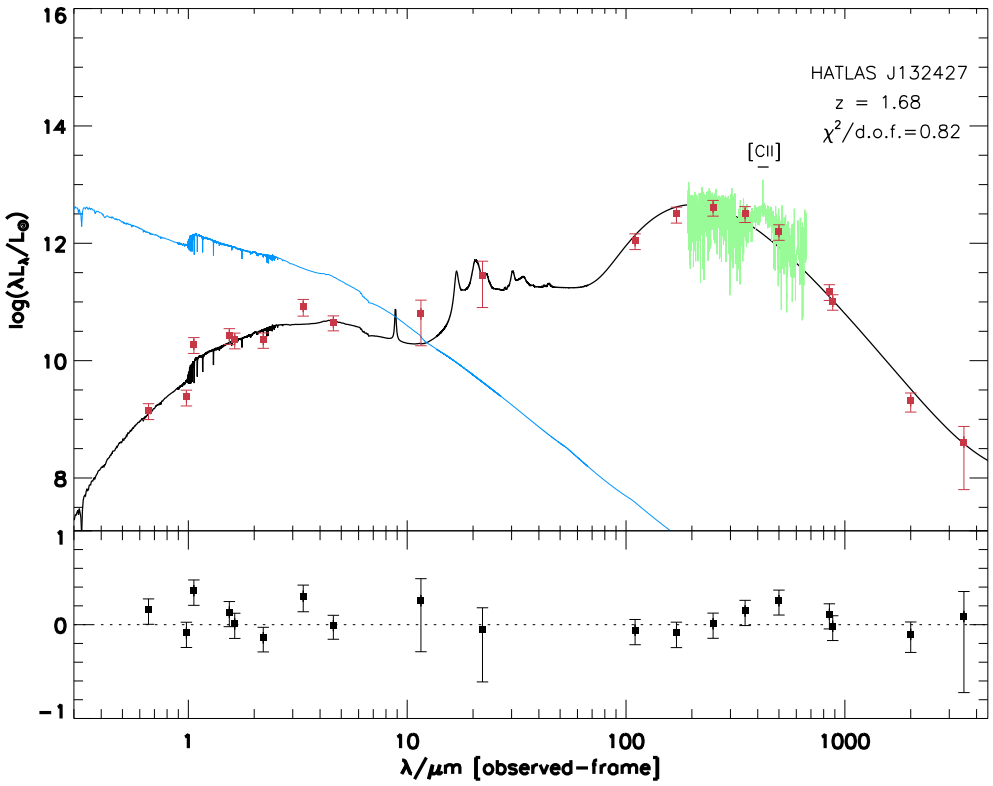

Figure 3.6: Top: The best-fit SED model is plotted in black while the intrinsic model without dust extinction is plotted in blue. The flux values have been de-magnified based on wavelength. The *Herschel* FTS spectrum is shown in green. The FTS spectrum is not used in the SED fit but is shown here for reference. Bottom: The residuals for each fit.

the source. The WISE photometry comes from the online WISE catalogs. The remaining photometry comes from George et al. (2013) and is discussed in Section 3. Table 2 lists the observed photometry used in the model fit with a spectroscopic redshift of 1.68. Because there is differential magnification for the dust and stellar components(Calanog et al., 2014) the observed fluxes were de-magnified based on wavelength. The stellar fluxes corresponding to the full arc in the SED were de-magnified by 15.7 ± 4.3 while the dust portion centered on the lower bright clump was de-magnified by 4.9 ± 1.8.

The WISE W3 and W4 bands, at 12 and 22 μm respectively, posed a problem as the MAGPHYS model SED showed those flux densities were a combination of both stellar and dust emission. In order to account for the uncertainty the error bars were extended to cover the entire magnification range, with flux densities corrected by 10, corresponding to the average of the dust and stellar magnification factors. Several fits were performed using a lower magnification for the W4 band, corresponding to more dust emission, as well as a higher magnification for the W3 band, corresponding to higher stellar contribution, in the end the average value provided the best-fit.

We note that the SMA flux measurements might be underestimated in the fit due to the short baseline coverage of the observations which could account for the difference between the 870 μm and 850 μm flux values. This could lead to an underestimate of the SFR which is correlated with the total dust luminosity (Kennicutt, 1998). The dust temperature is also correlated with the dust luminosity (Chapman et al., 2005) and therefore could also be underestimated. The compact configuration of SMA is expected to give an angular resolution of about $9''$ and, considering the large uncertainty and narrow width of the feature, the total flux from SMA should not be resolved out.

Figure 3.6 shows the final best fit for the SED plotted in black while the intrinsic model without dust extinction is plotted in blue. The physical properties derived from the SED fit are listed in Table 3. The FTS spectrum, with the [CII] line labeled, is shown for reference

Table 3.2: Photometry of HATLAS J132427

Instrument	λ	S_ν
CHFT (r band)	0.66 μm	0.05 ± 0.01 μJy
CHFT (z band)	0.98 μm	0.09 ± 0.01 μJy
HST (F105W)	1.06 μm	0.79 ± 0.4 μJy
HST (F160W)	1.54 μm	1.81 ± 0.6 μJy
Keck (H band)	1.63 μm	2.41 ± 0.8 μJy
Keck (K_s band)	2.20 μm	3.92 ± 0.6 μJy
WISE W1	3.35 μm	0.30 ± 0.01 mJy
WISE W2	4.60 μm	0.22 ± 0.01 mJy
WISE W3	11.56 μm	0.32 ± 0.03 mJy
WISE W4	22.09 μm	2.81 ± 0.7 mJy
Herschel (PACS)	100 μm	41 ± 4 mJy
Herschel (PACS)	160 μm	180 ± 14 mJy
Herschel (SPIRE)	250 μm	347 ± 25 mJy
Herschel (SPIRE)	350 μm	378 ± 28 mJy
Herschel (SPIRE)	500 μm	268 ± 21 mJy
SCUBA2 JCMT	850 μm	43 ± 1.2 mJy
SMA	870 μm	30.2 ± 5.2 mJy
PdBI	2 mm	1.2 ± 0.1 mJy
CARMA	3.5 mm	200 ± 170 μJy
VLA	4.3 cm	350 ± 30 μJy
VLA	21 cm	1.95 ± 0.24 mJy

and not used in the fit. The χ^2 per degree of freedom is 0.82. The importance of the results of the SED fitting and their derived properties are discussed in the next section.

3.6 Discussion

Our knowledge of the physical properties of DSFGs remains limited and the goal of recent studies is to increase our understanding of the starburst phenomena in DSFGs. For this purpose we examine the various components of the galaxy, including the dust temperature,

Table 3.3: SED fit and derived properties

SED fit	
f_μ(SFH/IR)	$0.857^{+0.20}_{-0.35}$
A_V	$4.19^{+0.20}_{-0.24}$
M_*	$11.2^{+3.2}_{-3.8}$ 10^{10} $M_\odot$
SFR	390^{+60}_{-57} $M_\odot$ yr^{-1}
L_{dust}	$46.8^{+5.6}_{-7.0}$ 10^{11} $L_\odot$
M_{dust}	$13.9^{+3.0}_{-2.8}$ 10^8 $M_\odot$
T_{dust}	$33.9^{+2.1}_{-1.9}$ K
sSFR	30 ± 2 10^{-10} yr^{-1}

Derived Properties	
μ_{dust}	4.9 ± 1.8
μ_{stars}	16 ± 4.3
r_{eff} Gas	8.8 ± 3.7 kpc
r_{eff} Dust	3.2 ± 1.2 kpc
Σ_{SFR}	$12.2^{+6.8}_{-6.7}$ $M_\odot$ yr^{-1} kpc^{-2}
Σ_{gas}	347 ± 200 $M_\odot$ pc^{-2}
M_{gas}	$8.6 \pm 3.3 \times 10^{10} \times \alpha_{CO}$ $M_\odot$
Gas Fraction $(M_{gas})/(M_{star} + M_{gas})$	0.43 ± 0.13

[1] Based on Narayanan et al. (2012)

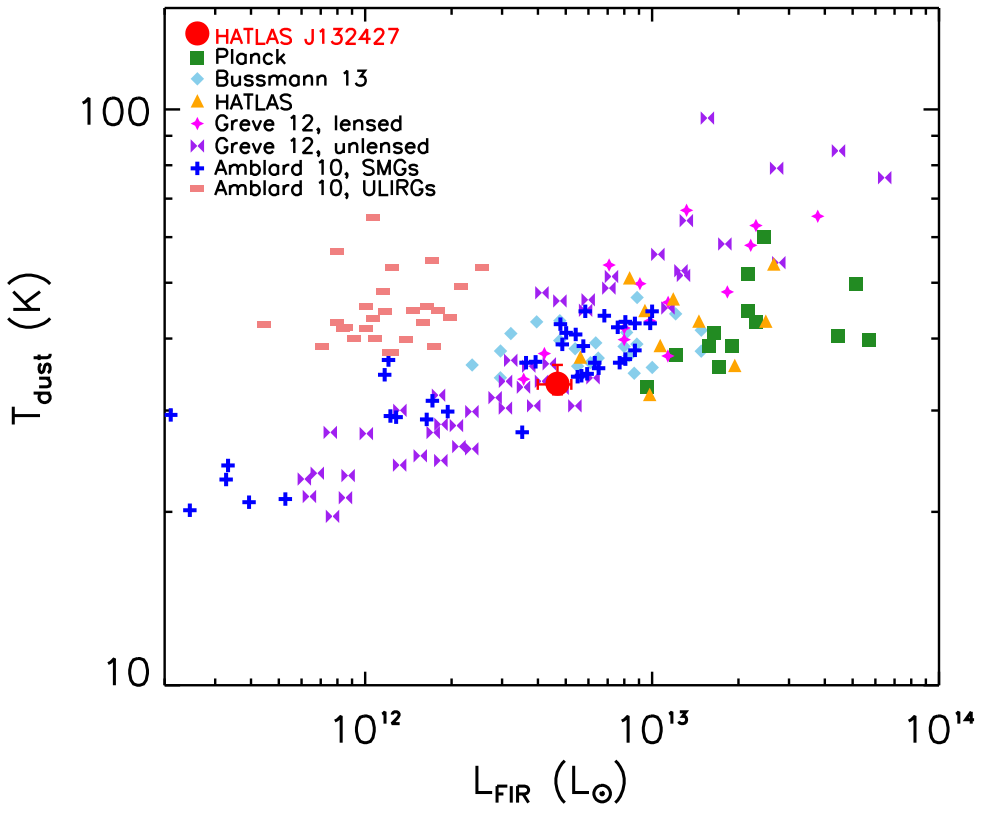

Figure 3.7: Dust temperature vs. FIR luminosity. For comparison other lensed and non lensed galaxies are plotted, including the other Plank/*Herschel* detected lensed galaxies (Canameras et al., 2015), *Herschel* lensed galaxies (Bussmann et al., 2013) as well as other lensed/unlensed SMGs and ULIRGs (Greve et al., 2012; Amblard et al., 2010). To make the comparison more instructive the lensed galaxies have had L_{FIR} de-magnified by a factor of 5.

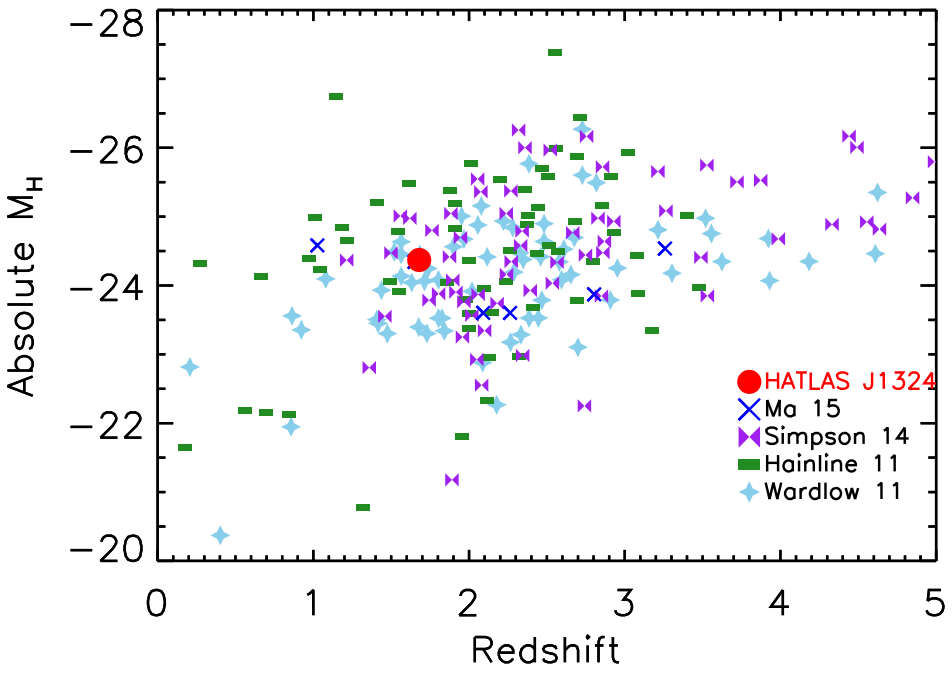

Figure 3.8: Rest-frame absolute H-band magnitude vs. redshift for DSFGs. The magnitudes have been corrected for magnification. For comparison DSFGs from other samples are included from Ma et al. (2015); Simpson et al. (2014); Hainline et al. (2011); Wardlow et al. (2013).

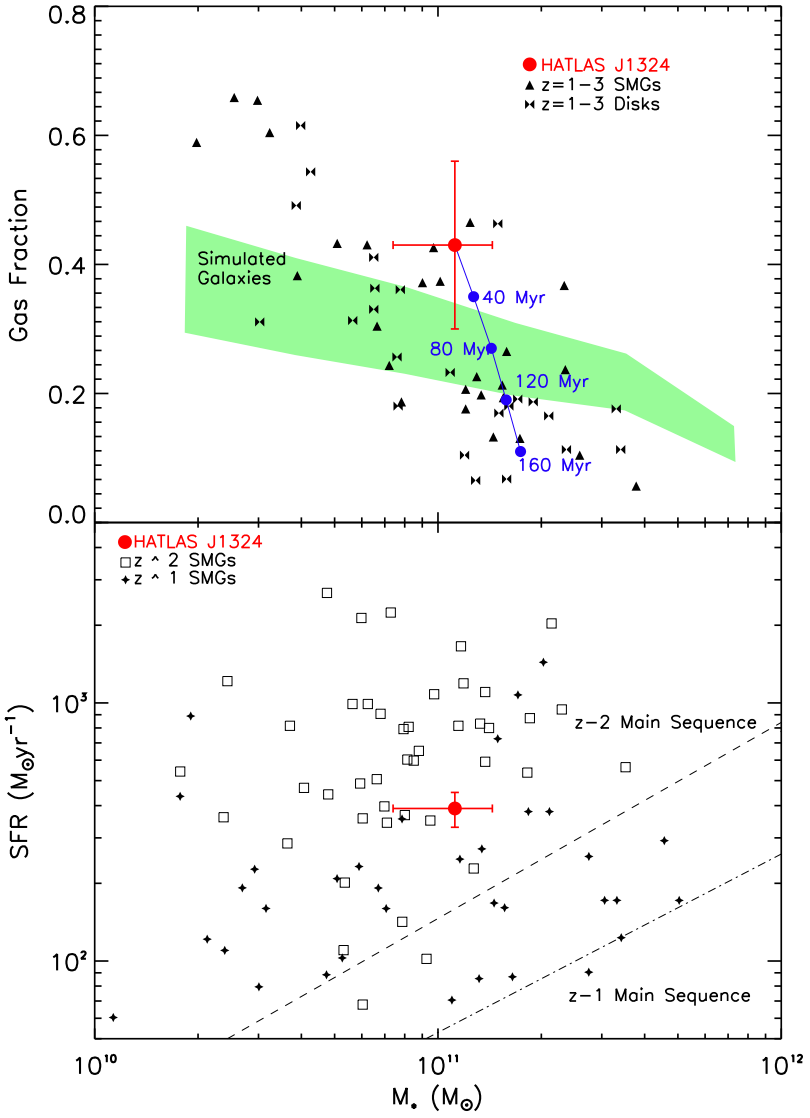

Figure 3.9: Top: Gas fraction vs. stellar mass. The other objects are from Narayanan et al. (2012). The green shaded region represents star-forming galaxies at $z = 2$ from cosmological hydrodynamic simulations (Davé et al., 2010). The blue circles represent the evolution of HATLAS J132427 over the course of 160 Myr. Each successive circle represents an 40 Myr time step with a constant SFR and mass conservation. Bottom: Star formation rate vs. stellar mass. For comparison $z \sim$ 2 SMGs are plotted (Fu et al., 2013) as well as $z \sim$ 1 SMGs (Michałowski et al., 2010a; Tacconi et al., 2010a; Banerji et al., 2011; Timmons et al., 2015). The $z = 1$ and $z = 2$ main sequence (Ma et al., 2015) are also plotted.

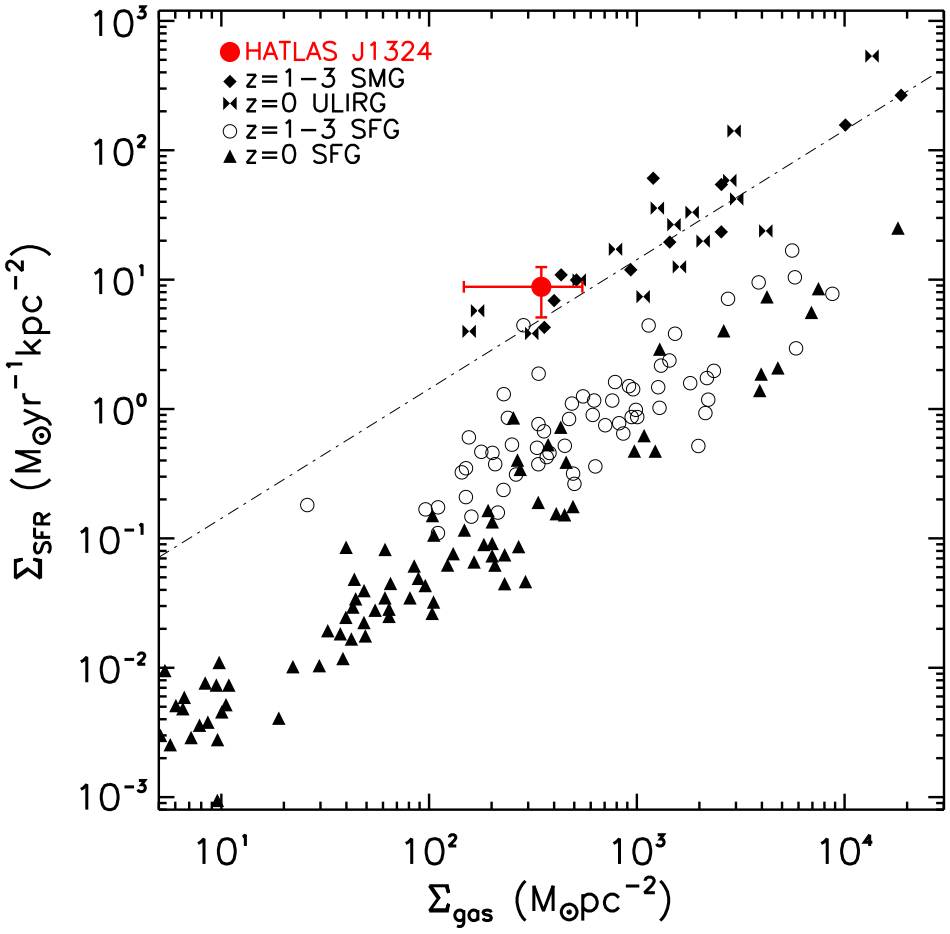

Figure 3.10: Star formation rate surface density vs. molecular gas surface density for local ULIRGS and SFGs as well as z $\sim 1-3$ SMGs and SFGs. For comparison SFGs are plotted (Kennicutt, 1998), as well as SMGs and local ULIRGs (Tacconi et al., 2013; Fu et al., 2013). The dashed line represents a constant gas consumption ($\tau_{\rm disk} = \Sigma_{\rm gas}/\Sigma_{\rm SFR}$) of 70 Myr for star-forming disks.

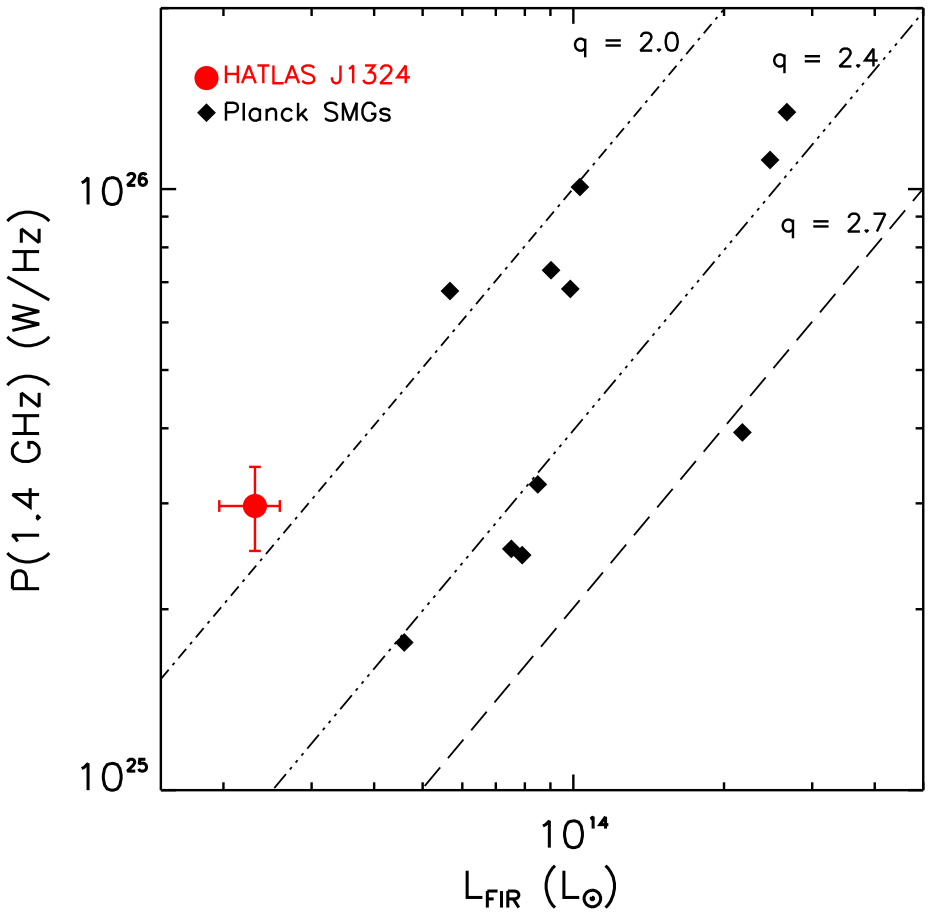

Figure 3.11: The far-infrared radio correlation for *Planck* and *Herschel* detected lensed DSFGs. The other *Planck* detected galaxies are from Canameras et al. (2015) and represent the total number of high-redshift lensed galaxies detected in both *Planck* and *Herschel*. The lines represent varying q values ($\log L_{IR}/(3.75 \times 10^{12}$ W)-$\log L_{1.4}/(\mathrm{W\ Hz^{-1}})$) of 2.0, 2.4, and 2.7.

the ratio of gas to baryons, the star formation rate and its density as well as the far-infrared radio correlation. We start with a discussion of the physical properties derived from the SED fit and compare them to other SMGs and DSFGs.

From the SED analysis, the estimated dust temperature is approximately 34 K, which is consistent with *Herschel*-selected galaxies at a similar luminosity (Symeonidis et al., 2013), as well as ALESS SMGs at a similar redshift (da Cunha et al., 2015). In Figure 3.7 we examine the relationship between dust temperature and FIR luminosity for SMGs as well as local ULIRGs. From Greve et al. (2012) the high FIR luminosity to dust temperature ratio is suggestive of a high magnification factor. In DSFGs an increased FIR luminosity correlates with an increased dust temperature. Both values come from the SED fit and are in agreement with the other high-z strongly lensed galaxies. Greve et al. (2012) estimate the magnification factor for the lensed galaxies to be a factor of 1–10, which is consistent with the magnification factor ($\mu_{\rm dust} \sim 5$) from the lens model for HATLAS J132427.

Stellar masses, as derived from SED fits, depend on a few fundamental assumptions such as the assumed star formation histories (SFH), initial mass functions (IMF) and population synthesis models (see Chabrier 2003; Thomas et al. 2005; Davé et al. 2012; Michałowski et al. 2012; Conroy et al. 2013; Michałowski et al. 2014). These introduce uncertainties in the measured stellar mass which, along with uncertainties introduced by variations in the metallicity, is usually observed as the scatter around the main sequence in the mass-SFR relation (see also Shivaei et al. 2015 & Speagle et al. 2014). Rest-frame H-band absolute magnitude (M_H) can act as a trace of stellar mass that does not depend upon an assumed SFH. In Figure 3.8, HATLAS J132427 is shown to have an M_H consistent with other DSFGs samples and likely has a stellar mass consistent with DSFG samples.

To calculate the gas mass we use the $\rm CO_{(2-1)}$ luminosity from George et al. (2013) ($\rm CO_{(2-1)}$ $= 11.3 \pm 1.4$ Jy km s^{-1}) and adopt a CO-$\rm H_2$ conversion factor $\alpha_{\rm CO} = 1$ M$_\odot$ (K km s^{-1} pc^2)$^{-1}$ consistent with other SMGs (e.g., Tacconi et al. 2008; Hodge et al. 2012). This results in a

gas mass of $8.6 \pm 3.3 \times 10^{10} \times (\alpha_{\rm CO}/1.0)$ $M_\odot$ assuming the magnification factor of the gas distribution to be $\mu = 4.9$, consistent with the dust. An alternative calculation for the gas mass comes from Scoville et al. (2014), in which 28 ($z < 3$) SMGs are used to find the ratio of the gas mass to the 850 μm luminosity. This ratio is found to be 1.01 ± 0.52. In Scoville et al. (2014) an $\alpha_{\rm CO}$ of 4.6 is used and so here we scale the ratio down to $\alpha_{\rm CO} = 1$, giving a final ratio of $L_{850}/M_{\rm ISM} = 0.22 \pm 0.11$. This ratio gives a gas mass of $7.3 \pm 4.6 \times 10^{10} \times (\alpha_{\rm CO}/1.0)$ $M_\odot$ for HATLAS J132427, which is consistent with the previous result.

The top portion of Figure 3.9 shows the gas-to-baryon fraction vs. stellar mass. For comparison $z = 1-3$ SMGs are plotted as well as z = 1 − 3 main sequence star-forming galaxies. For its stellar mass, HATLAS J132427 has a large gas-to-baryon ratio $(M_{\rm gas})/(M_{\rm star} + M_{\rm gas})$ of 0.43. This is in agreement with other measurements of high-z star-forming galaxies (Tacconi et al., 2013). The green shaded region in Figure 3.9 shows star-forming galaxies at $z = 2$ from cosmological hydrodynamic simulations (Davé et al., 2010). In Narayanan et al. (2012) it is suggested that $\alpha_{\rm CO}$ is overestimated for systems at high redshift which could account for some of the scatter. The blue circles on Figure 3.9 represent the future evolution of HATLAS J132427 assuming a constant SFR and mass conservation. Each blue dot represents a time step 40 Myr and shows the slope of the evolution as being steeper than the overall trend of gas fraction vs. M_*, due to the fact that some gas must be recycled. The bottom portion of Figure 3.9 shows the star formation rate vs. stellar mass. Also plotted are $z \sim 1$ SMGs and $z \sim 2$ SMGs from the literature for comparison. HATLAS J132427 is above the main sequence lines for both $z = 1$ (Elbaz et al., 2007) and $z = 2$ (Daddi et al., 2007). This is consistent with the large gas mass of HATLAS J132427 and its being observed in a star-bursting phase. Given the scatter in this relation, the HATLAS J132427 measured mass and star formation is different from the underlying star-forming galaxy population and is consistent with SMGs at similar redshifts.

Figure 3.10 shows the star formation surface density vs. molecular surface density. Plotted for comparison are $z = 1 - 3$ SMGs and SFGs, as well as local ULIRGs and SFGs. The gas area and effective gas radius is calculated using the observed gas area from CARMA and computing a de-magnified gas area based on the lens model. The dust area and effective dust radius are calculated by measuring the area of the SMA source plane reconstruction. The gas consumption time $\tau_{\rm disk}$, which refers to the star-forming disk region can be calculated using the ratio $\tau_{\rm disk} = \Sigma_{\rm gas}/\Sigma_{\rm SFR}$. For HATLAS J132427 the gas consumption time is ~ 10 Myr. The dot dashed line on the plot represents $\tau_{\rm disk} = 70$ Myr, which is populated with SMGs and ULIRGs while the more quiescent star-forming galaxies have $\tau_{\rm disk} \sim 1.5$ Gyr. This short timescale of star formation for HATLAS J132427 is consistent with other DSFGs.

We investigate the possibility of an AGN contribution to this source by examining the correlation between FIR and 1.4 GHz radio luminosity which is shown in Figure 3.11. It is common to define this correlation in terms of a value q which is defined as $\mathrm{q} = \log(\mathrm{L_{IR}}/(3.75\times 10^{12}\ \mathrm{W}))\text{-}\log(\mathrm{L_{1.4}}/(\mathrm{W\ Hz^{-1}}))$. A spectral index $\alpha = -0.8$ is assumed (Condon, 1992). The q value for HATLAS J132427 is 1.90 which is lower than the average for DSFGs ~ 2.4 (Ivison et al., 2010). The low q value corresponds to a high relative luminosity in the radio emission and might suggest that HATLAS J132427 has a luminous AGN (e.g.,Vlahakis et al. 2007; Bourne et al. 2011). It is assumed in this calculation that the radio and FIR luminosity are being magnified by the same factor. The output values of MAGPHYS are not strongly affected by AGN contamination (da Cunha et al., 2015). Hayward & Smith (2015) shows that strong AGN contamination can lead to an overestimation of the stellar mass in a SED analysis. If the longer wavelength radio is less magnified due to differential lensing the q value would be underestimated as a result.

3.7 Summary

HATLAS J132427.0+284452 is a *Herschel* Astrophysical Terahertz Large Area Survey (H-ATLAS) selected strongly lensed arc of length $\sim 15''$ at $z = 1.68$. HATLAS J132427 is also *Planck* detected at 1.30 ± 0.15 Jy in the 350 μm band and is one of a few high-z Planck detections in H-ATLAS. A lens model with source plane reconstructions at several wavelengths allows the estimation of magnification factors for the stars $\mu_{\rm stars} \sim 16$ and the dust $\mu_{\rm dust} \sim 5$. The different magnification values for the dust and stellar components become important for the SED analysis in which the observed fluxes must be de-magnified according to wavelength. This source demonstrates the fact that lens models constructed in a single wavelength should not be considered complete due to the effect of differential lensing.

Physical properties of the galaxy are estimated by fitting model SEDs gives a SFR of ~ 400 $M_\odot$ yr^{-1} and a stellar mass of $\sim 11 \times 10^{10}$ $M_\odot$ which are consistent with a high-z dusty star-forming galaxy. The SFR surface density 12 $M_\odot$ yr^{-1} kpc^{-2} is high compared to the molecular gas surface density 350 $M_\odot$ pc^{-2}. This comes from the lens model reconstruction of the dust area which reveals a large amount of star formation is happening in a single clump. We find that the gas fraction is slightly higher than star-forming galaxies from cosmological hydrodynamic simulations but still consistent with other observations of SMGs at this redshift. The far-infrared radio correlation suggests that HATLAS J132427 might host a luminous AGN or it might be an artifact of differential lensing.

Chapter 4

Dust and Stellar Emission from Lensed High Redshift Simulations of Galaxies in FIRE 2 Simulations

We make use of FIRE-2 cosmological simulations in order to model the stellar and dust emission from sub-millimeter bright galaxies. We investigate the role of differential magnification in distant lensed sub-millimeter galaxies by modeling the simulated emission in our sample at various wavelengths for different lensing configurations. We compare the results to observation and find that there is a physical offset between the light coming from stars and the light radiated by dust in the simulated galaxies that is in agreement with observations. The simulated light emission is found to be more compact in the stellar regime than the dust regime compared with observed galaxies. The effect of the lensing configuration on the differential magnification is estimated through various lens models. We study the three main components that can affect the differential magnification: physically offset between the lens and the source, relative distance between the source, lens and the observer and the mass distribution of the lens. These all contribute to a differential magnification of the stellar light

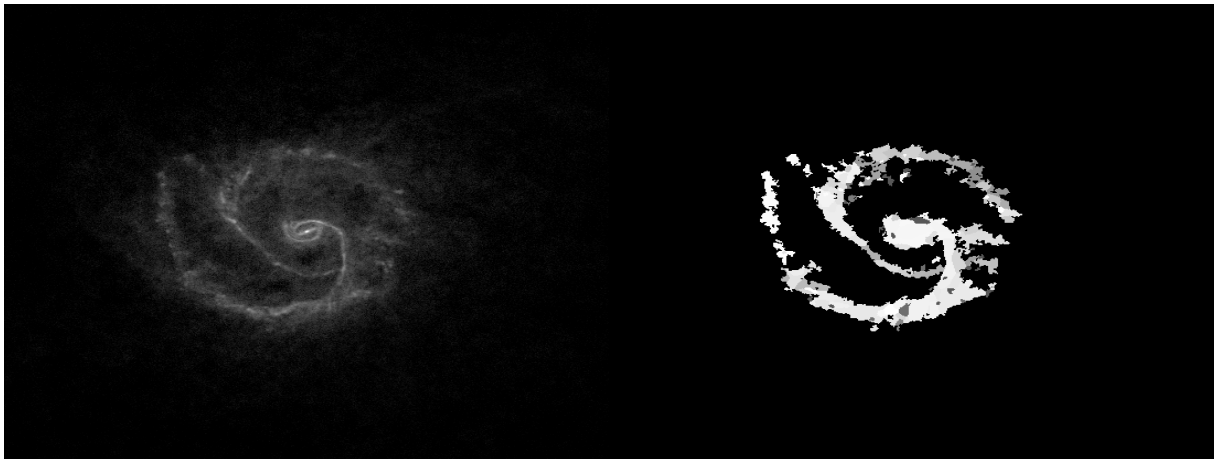

Figure 4.1: The left side shows the simulated FIR emission (500 μm) from one of the sample galaxies. The resolution of the SKIRT output is $\sim$ 25 pc/pixel. The right side is the SourceExtractor model for the galaxy that is used to create the ellipses passed through the lens model. The typical sizes for the arcs used for the models is 10^2 pc to 10^3 pc.

vs. the dust emission. When deriving the physical properties of galaxies from model SEDs we find that the overall effect of differential magnification is an underestimation of the ratio of star-formation rate to stellar mass that is equivalent to the ratio of stellar magnification to dust magnification.

4.1 Background

The importance of the gravitational lensing phenomenon to modern observational cosmology can not be overstated. The flux amplification and increased spatial resolution of strong gravitational lensing allows for the observation of distant and dust obscured galaxies. There now exists a very large body of work which utilizes gravitational lensing to study the physical properties of high redshift galaxies (Fu et al., 2012; Messias et al., 2014; Calanog et al., 2014; Timmons et al., 2016; Nayyeri et al., 2017b). These studies utilize multi-band wide-area observations such as the *Herschel*-Astrophysical TeraHertz Large Area Survey (H-ATLAS) (Eales et al., 2010) to identify strongly lensed systems. Follow-up observations with

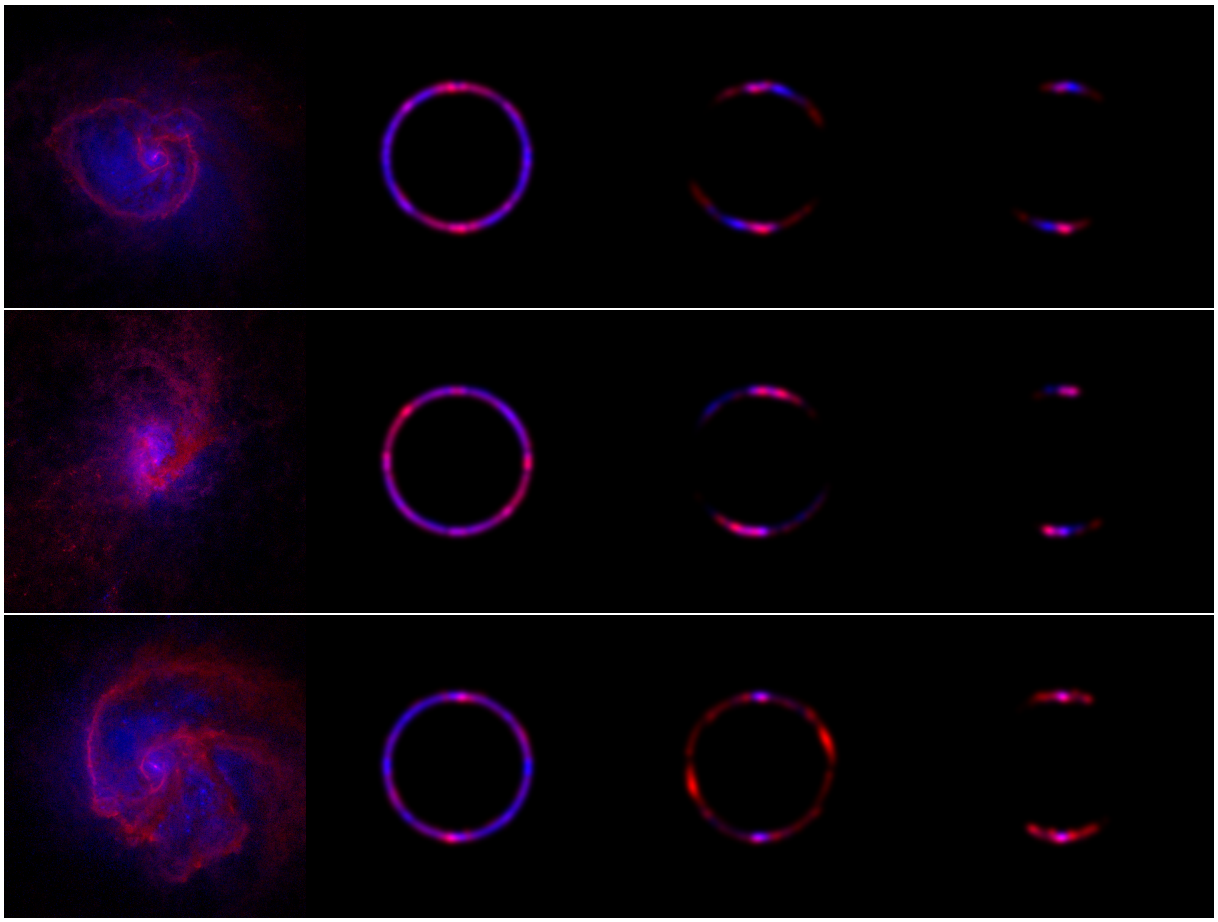

Figure 4.2: Simulated emission from the source plane is shown as the left most panel. The corresponding image plane for several lensing potential positions is shown in the three panels to the right. The blue in each image represents the simulated light coming from the stellar portions of the galaxy while the red represents the warm dust emission.

terrestrial telescopes like Keck and ALMA has allowed astronomers to study the physical properties of strongly lensing systems.

Many studies involving strongly lensed galaxies have shown that there can be a discrepancy between the magnitude of magnification for different wavelengths of light (Blandford & Narayan, 1992). This effect is known as differential lensing. Since gravitational lensing is not color dependent differential lensing is a result of spatial offset between the emission of light coming from different components of a galaxy (stellar light, warm dust, cool gas, etc). Recent studies have shown that a compact source will be more magnified due to strong lensing than a diffuse source using a two component model (Hezaveh et al., 2012). Understanding the effect of differential lensing will shed light on the mixing and compactness of galaxy components namely, stellar components and warm dust which can be compared with physical properties such as star formation to see what effect the structural make-up of a galaxy has on these properties.

With the observations of galaxies at multiple wavelengths we can construct the spectral energy distribution (SED) of the sources and use that to derive the physical properties, in particular the stellar mass and star-formation rates. Recent studies show that the position of individual sources on the main-sequence of star-forming galaxies can be biased by the presence of differential lensing (Blain, 1999; Pontoppidan & Wiklind, 2001).

One key area in which differential lensing is less understood is the mid-IR wavelength range. When correcting for differential lensing, the SED is usually divided into just the stellar component which is de-magnified using optical and near-IR wavelengths and the dust component which is de-magnified using far-IR wavelengths. The mid-IR is a combination of stellar and dust light which also contains prominent poly-aromatic hydrocarbon (PAH) lines. It is therefore important to investigate the magnification of this region to see if it follows the stellar or the dust emission magnification.

The differential lensing effect is prominent in high-redshift dusty star forming galaxies (Bussmann et al., 2013; Calanog et al., 2014; Timmons et al., 2016). These galaxies are bright in the sub-millimeter regime due to a large fraction of light being absorbed and re-radiated at longer wavelengths due to the dust. Large gas and dust reservoirs within dusty star-forming galaxies have a large spatial extent and are offset with respect to the stellar emission. Obscured star-formation, as present in sub-millimeter bright galaxies (SMGs), make up a large fraction of the global star-formation rate density at high redshifts (Le Floc'h et al., 2005). It is paramount to make sure that the studies being done on this star-bursting set of galaxies is done carefully as they reveal an important phase in cosmic evolution.

The proliferation of massive high resolution cosmological simulations has opened up a new era for cosmology but tensions remain between simulation and observation. One relevant example being the gas-to-baryon fraction vs. stellar mass. Observations like those done in Narayanan et al. (2012) show a steep slope for the gas-to-baryon fraction while simulated galaxies from Davé et al. (2010) show a more flattened slope suggesting less gas reservoirs for star-formation. While the effect of differential lensing is found routinely in observational studies it is reasonable to ask if it can be reproduced in cosmological simulations. Studying the differences in simulation and observation with regard to lensing further helps to identify the underlying reasons for the spatial offset in emitted light coming from galaxies specifically with respect to the mixing and compactness of SMGs.

In this chapter we utilize the power of high resolution cosmological simulations to recreate the effect of differential lensing. We pass the simulated light from 13 sub-millimeter bright galaxy snapshots through different model lens systems to confirm that simulations are recreating the correct structure of high-redshift dusty galaxies as well as to study the effects of different lensing systems on the derived physical properties that come from the spectral energy distribution of the simulated light.

The chapter is organized as follows: In the next section, the simulations are described. Section 4.3 describes the radiative transfer model. In section 4.4 the gravitational lens model is presented. In section 4.5 the results of the data analysis are presented. Section 4.6 contains a discussion of the results and their implications to cosmology and galaxy formation. Section 4.7 is a brief summary.

Throughout we make use of the standard flat-ΛCDM cosmological model with H_0= 67.7 km s^{-1} Mpc^{-1} and Ω_Λ=0.69 (Planck Collaboration et al., 2016a).

4.2 Simulations

The galaxies used in this study were simulated using the Feedback In Realistic Environments (FIRE) project (Hopkins 2017). The details of the simulations can be found in Anglés-Alcázar et al. (2017). FIRE consists of a set of hydro-dynamical cosmological zoom-in simulations that aim to accurately simulate the feedback effects within galaxies during formation. Without proper modeling of galaxy feedback, galaxies would cool too quickly, eventually growing too large in size (Hopkins 2011) and not reflecting the observational evidence for galaxy mass (Kennicutt, 1998). FIRE team simulations have been shown to be in strong agreement with observation on a number of important galaxy physical parameters, including stellar masses, star-formation rates and metallicities (Hopkins et al., 2014; van de Voort et al., 2015; Ma et al., 2016; Sparre et al., 2017).

The simulations in Anglés-Alcázar et al. (2017) make use of the newer FIRE-2 code (Hopkins et al., 2018) which has improved numerical accuracy. The galaxies for this study come from a sample of massive galaxies as a part of the MassiveFIRE project (Feldmann et al., 2016) which was improved upon in Anglés-Alcázar et al. (2017) with the inclusion of a new model for black hole growth.

Table 4.1: Physical Properties of Simulated Halos

Parameter	Value
$\log_{10}M_{halo}/M_{\odot}$	12.5
$\log_{10}M_{*}/M_{\odot}$	11.2
$\log_{10}M_{gas}/M_{\odot}$	10.4
$\log_{10}SFR/M_{\odot}yr^{-1}$	100
$r_{1/2}$/kpc	0.86

Table 4.1: Average properties of simulated halos at z = 2. All values calculated within 0.1 R_{vir}. $r_{1/2}$ is the half-mass radius, which is calculated using the stellar mass within 0.1 R_{vir} from Cochrane et al. (in prep).

Details of the selection process for galaxies in this study can be found in Cochrane et al. in prep. The galaxies were selected based on reaching Milky Way halo mass ($M_{\rm halo} \sim 10^{12.5} M_{\odot}$) by $z = 2$. The average properties of the halos coming from the FIRE-2 simulations is given in Table 1. The halos used are consistent with observations of high-redshift star-forming galaxies. Selecting sub-millimeter bright galaxies out of the total number from the simulation is done through a quick estimation as the total number of galaxies in large FIRE-2 simulations makes selection difficult. At each snapshot the star-formation rate is measured and the dust mass is estimated using the gas mass where $M_{dust} = 0.001\ M_{gas}$. The combination of these tracers is used to get a crude estimate for the sub-millimeter flux density for the selection of SMGs. Thirteen snapshots from the FIRE-2 simulations were found to be sufficiently bright in the FIR regime and are used in this study.

4.3 Radiative Transfer Model

To correctly model the differential magnification effect through lensing the light emitted across a broad SED for each snapshot needs to be properly modeled. Following the path of

photons as they are emitted and absorbed is a difficult task numerically. The details of the radiative transfer methods used in this study are presented in Cochrane et al. in prep. The process is briefly described here.

In order to properly model the multi-wavelength emission from the simulated galaxies the radiative transfer code: Stellar Kinematics Including Radiative Transfer (SKIRT) is utilized. The SKIRT project simulates continuum radiation transfer in dusty galaxies by employing the Monte Carlo technique to properly emulate processes including scattering, absorption and emission by the dust (Baes et al., 2011).

The 3-D geometries of the stellar and dust particles are mapped out for each simulated galaxy. Photons are emitted by star particles, which come from the simulation, and are traced through the interstellar medium (ISM) at each time step. The dusty medium in which the photons propagate comes from Weingartner & Draine (2001) prescription for dust in a Milky Way type galaxy and assuming a dust-to-metals mass ratio of 0.4. This includes both large grains as well as ultra small grains which correspond to polyaromatic hydrocarbons (PAHs). The star particles are given a STARBURST99 spectral energy distribution (Leitherer et al., 1999).

The flux is 'observed' by seven detectors, $z = 0$, at different inclinations with respect to the emitting galaxy. The wavelength range covers from the UV to the FIR rest-frame wavelengths. The resolution of the final image is 25 [pc/pixel] with an image output for 100 wavelength points for each galaxy in the study.

4.4 Lens Model

We make use of the program LENSTOOL (Kneib et al., 1996; Jullo et al., 2007) to model the image plane of the simulated galaxies. The input for LENSTOOL is not a direct image

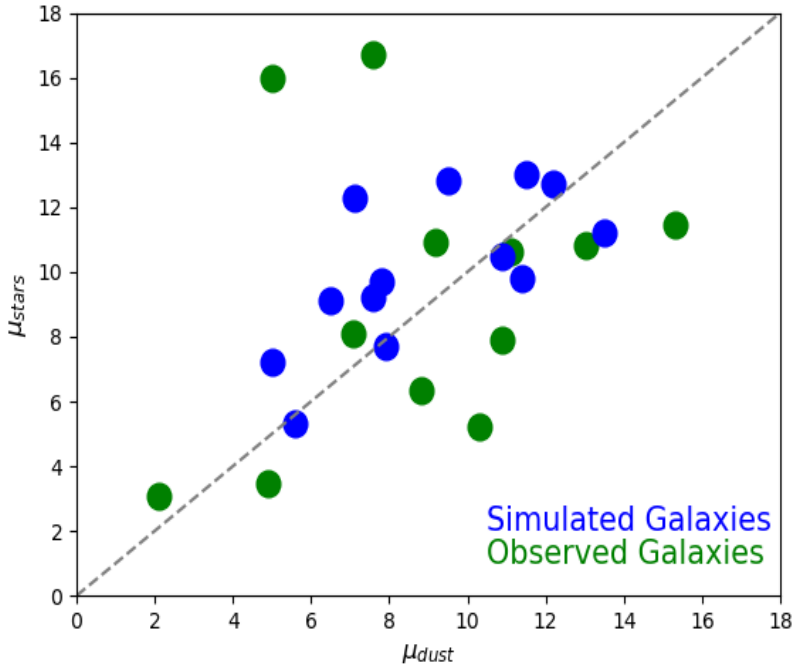

Figure 4.3: The effect of differential magnification between two distinct wavelengths which correspond to dust emission and stellar emission for both the simulated galaxies (blue) averaged over many different lens configurations as well as observed galaxies (green). The observed galaxies come from Calanog et al. (2014); Bussmann et al. (2013); Dye et al. (2014); Fu et al. (2012); Gavazzi et al. (2011)

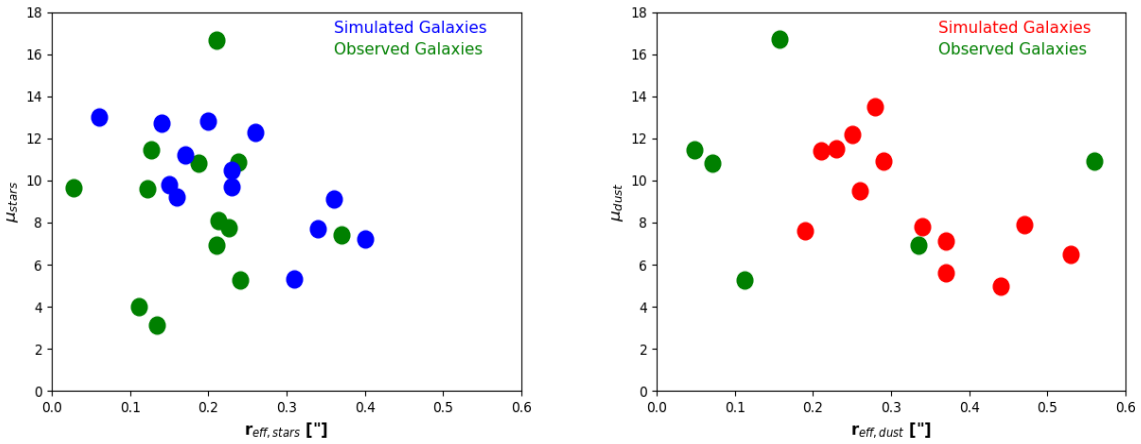

Figure 4.4: Left: The magnification is compared with the effective radius for the stellar light. The blue points represent the simulated galaxies from the sample while the green points represent the observed galaxies from Calanog et al. (2014); Bussmann et al. (2013); Dye et al. (2014); Fu et al. (2012); Gavazzi et al. (2011). Right: The magnification is compared with the effective radius for the warm dust emission. The red points represent the simulated galaxies from the sample while the green points represent the observed galaxies from Calanog et al. (2014); Bussmann et al. (2013); Dye et al. (2014); Fu et al. (2012); Gavazzi et al. (2011).

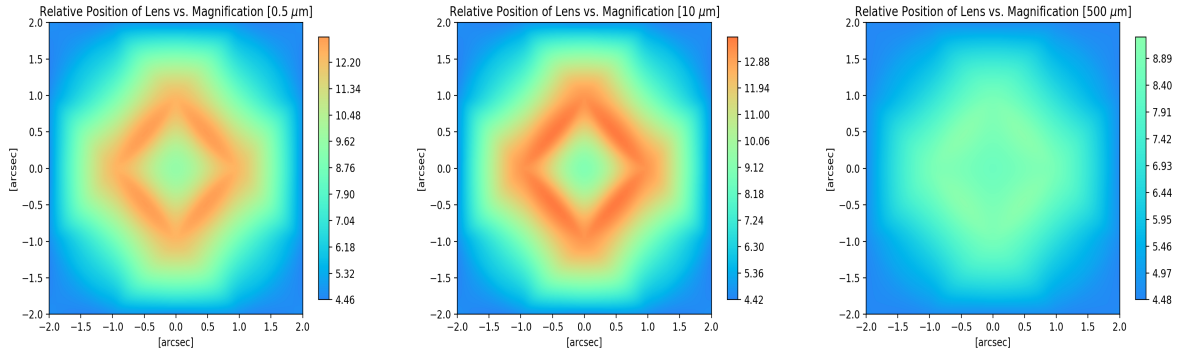

Figure 4.5: The predicted magnification as a function of the position of the foreground lens with respect to the background. The different points in the 2D figure represent different locations of the foreground lens and the color bar represents the measured magnification at that offset.

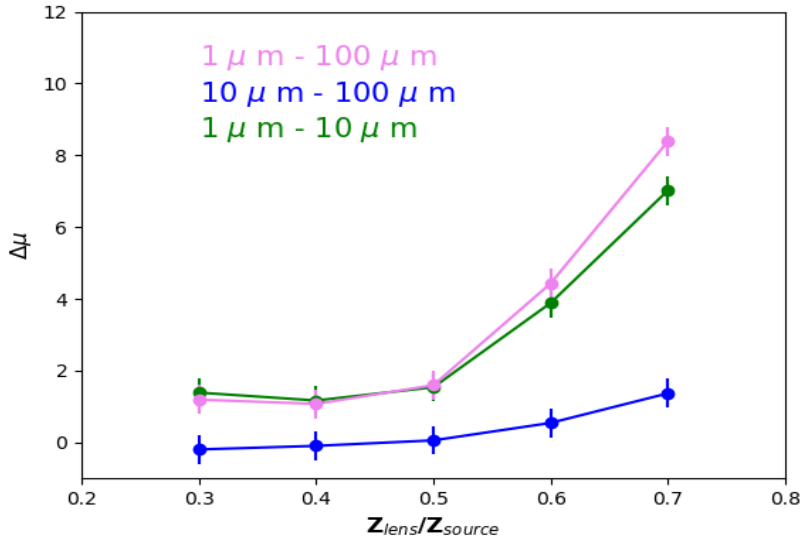

Figure 4.6: The difference in magnification between different wavelength points (1μm, 10μm and 100μm) as a function of the position of the lens compared with the source averaged over the 13 snapshots.

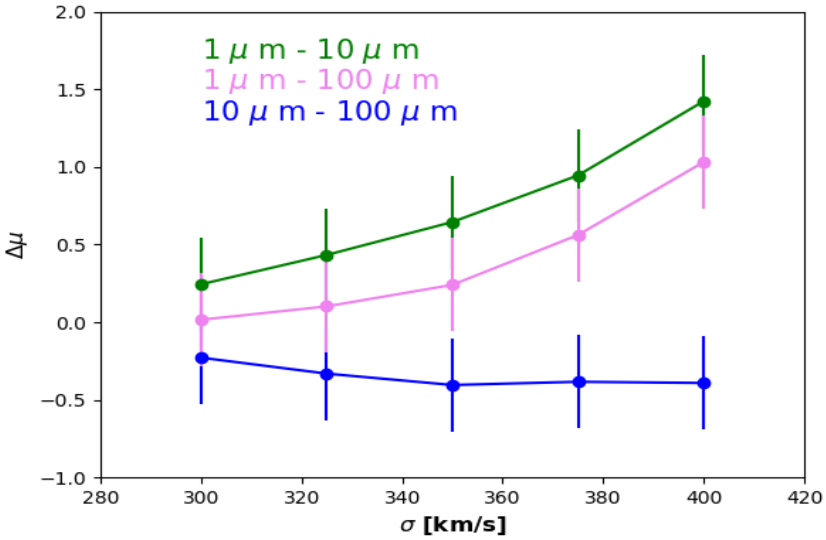

Figure 4.7: The difference in magnification between different wavelength points (1μm, 10μm and 100μm) as a function of the velocity dispersion of the foreground lens averaged over the 13 snapshots.

but a list of arcs whose properties determine the resulting image. In order to model the arcs, photometry is done on the source plane flux which is the output from the SKIRT analysis. The is done using SourceExtractor (Bertin & Arnouts, 1996). The simulated flux is measured using ISO apertures giving the magnitude, orientation, size and position of each arc. The typical sizes for the arcs used for the models is 10^2 pc to 10^3 pc. The resolution of the SKIRT output is ~ 25 pc/pixel.

Figure 4.1 shows the result of passing one of the simulated emission images through SourceExtractor in order to recover positions and sizes of ellipses. On the left side of the figure is the 860μm emission from one of the simulated galaxies. On the right side is the resulting components of the emission as detected by SourceExtractor. The output catalog from SourceExtractor gives the information for each component of the galaxy measured.

Once a list of arcs in the source plane is generated it is passed through the lens model. The lens model consists of singular isothermal sphere (SIS) which can be modified by changing the velocity dispersion of the model lens. The relative position of the lens with respect to the background source can also be changed as well as the redshift of the source. The results of modifying these parameters and their effect on differential magnification is presented in the results section.

While each simulated galaxy has output files at many wavelengths we chose the 1μm and the 860μm as a good representation of the stellar emission and the dust emission respectively. These wavelengths correspond to typical observed wavelengths in order to compare the simulated galaxy sample with observations.

In Figure 4.2 we show the simulated emission in the source plane alongside the simulated emission in the image plane based on differing positions of the lensing potential. The first image on the left is the simulated emission from stellar light in blue and the simulated emission from dust in red at the source plane for three of the galaxies used in the analysis.

In the next image to the right a potential is placed at in alignment with the center of the source plane image and the resulting image plane reconstruction is shown. In the next two images to the right the potential is moved off center to show the effect of multiple components in the image plane.

4.5 Results

Figure 4.3 shows the effect of differential magnification between two distinct wavelengths for both the simulated galaxies in this study as well as a comparison with observed galaxies. As can be seen in the figure, the simulated galaxies show a clear difference in magnification between the emission from stars and the emission from dust. Interestingly, the simulated galaxies appear to have a higher magnification with respect to the dust emission than the light coming from stars when compared with the observed galaxies.

On the left side of Figure 4.4 the magnification is compared with the effective radius for the stellar light. This is compared with the stellar light from the observed galaxies. In the simulated galaxies there is a clear relationship between the compactness of the component and the magnification factor. In the simulated galaxies the stellar component is found to be on average more compact and having a higher magnification. This is not seen in the observed galaxies.

On the right side of Figure 4.4 the magnification is compared with the effective radius for the dust emission from the simulations. This is compared with the dust emission from the observed galaxies. In the simulated galaxies there is a clear relationship between the compactness of the component and the magnification factor. In the simulated galaxies the stellar component is found to be on average more compact and having a higher magnification. This is not seen in the observed galaxies.

The effect of the lensing system on differential magnification is considered in Figures 4.5, 4.6 and 4.7. In Figure 4.5 the position of the foreground lens is changed with respect to the background source. The magnification is measured and the average is taken over the 13 simulated galaxies at each emission. The figure shows the results for three wavelengths in order to see if the positional change effects different wavelengths and by what magnitude.

As can be seen in the figure, the effect of changing the position of the foreground lens is wavelength dependent for the sample of simulated galaxies. The diffuse dust emission is not as effected by the changing position as the more compact stellar type emission.

Figure 4.6 shows the effect of changing the relative distances between the lens and the source. The difference in magnification between three distinct wavelengths (1μm, 10μm and 100μm) is compared to the change in redshift ratio of the lens and source. As the lens moves closer to the source the differential magnification grows dramatically for the difference in the near-IR/optical wavelengths vs. both mid-IR and far-IR. The difference between the mid-IR and far-IR wavelengths does not show the same effect.

Figure 4.7 shows the effect of changing the velocity dispersion of the SIS foreground lens. The difference in magnification between the same wavelengths as the previous figure (1μm, 10μm and 100μm) is compared to a range of velocity dispersion. The changing velocity dispersion has an effect on the differential magnification between the shorter wavelengths with respect to the mid and longer wavelengths. The larger mass potential increases the magnification of the stellar components more than it does the dust components.

4.6 Discussion

Studies have shown that differential magnification is both very real (Calanog et al., 2014) and can have an effect on the derived physical properties coming from the spectral energy

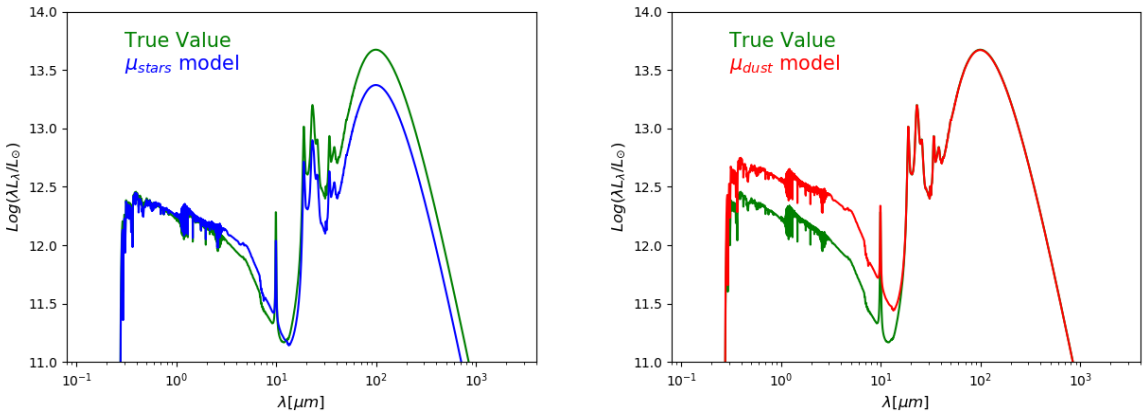

Figure 4.8: Left: The "true" value of the SED, the SED when differential magnification is taken into account, is plotted against if the observed fluxes were de-magnified by the stellar magnification. Right: The result if the observed flux was de-magnified by the dust magnification compared with the true value. It is important to note that in the case of the figure $\frac{\mu_{\rm dust}}{\mu_{\rm stars}} = 0.5$. The SEDs are plotted in the rest-frame.

distribution (Serjeant, 2012; Er et al., 2013). Clearly, this effect must rise out of some spatial offset between different emitting sources within a galaxy. As our cosmological simulations get increasingly more sophisticated in modeling the inner workings of galaxies it is important to make sure that the structure of the resulting simulation is matched with what is seen observationally. The differential lensing effect is one clear way to try to resolve tensions between simulation and observation.

In this study the galaxy emission passed through a simple lens model shows the signs of differential magnification. The simulated galaxies showed an average $\frac{\mu_{dust}}{\mu_{stars}} = 0.9$ while the observed galaxies showed and average $\frac{\mu_{dust}}{\mu_{stars}} = 1.1$. It has been shown that higher magnification can result from more compact regions and the above result would suggest that the simulated galaxies are either more compact in the stellar emission or are not as compact in the dust emission as the observed galaxies.

When comparing the simulated stellar light to the effective radius it is seen that the magnification drops as the effective radius gets larger. This is what is expected and matches fairly well with the observed galaxies. The simulated dust emission follows the same pattern

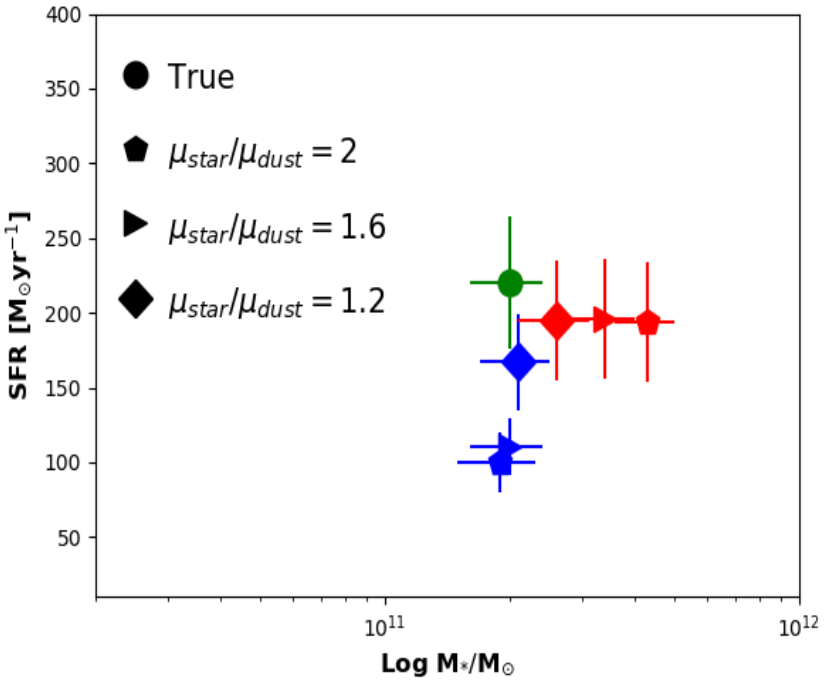

Figure 4.9: The SFR vs. stellar mass. The green point represents the model when the stellar and dust emission are correctly de-magnified by wavelength. The blue points represent when only the stellar model is used while the red points correspond to when the dust magnification is used to de-magnify. The differing symbols show the effect for different values of $\frac{\mu_{\rm stars}}{\mu_{\rm dust}}$. It can be seen here that the larger the differential magnification the further the estimated physical properties are from the true value. De-magnifying by the stellar light results in an underestimation of the SFR while de-magnifying by the dust emission results in an overestimation of the stellar mass with the difference between the estimated value and the true value being approximately equal to the ratio of $\frac{\mu_{\rm stars}}{\mu_{\rm dust}}$

as the stellar light with an overall dust radius being larger than the stellar radius. For the observed galaxies, the effective dust radius is more compact than the simulated galaxies. This might be explained by the simple lack of data in the dust regime or it is a selection effect due to more compact dust regions being preferentially selected in the FIR due to their high magnification and brightness.

The lensing system plays a distinct roll in the amount of differential magnification as can be seen in Figures 4.5, 4.6 and 4.7. As the lensing system changes the main component to be effected is the shorter wavelength emission which has a compact distribution. This compactness makes the shorter wavelength light, which corresponds to the stellar emission, more sensitive to the magnifying effect of the foreground lens.

The over all effect of the lensing configuration needs to be taken into account for studies that wish to properly de-magnify the background emission for an analysis of the SED. For lenses with a larger potential as well as lensing systems in which the foreground lens is closer to the background source than the observer the short wavelength light has a stronger magnification than in other lensing systems making the effect of differential magnification more pronounced. For the opposite case, one with a small mass potential or a lens that is closer to the observer, the effect is much smaller to the point at which it becomes negligible.

The position of the lens with respect to the background source can also effect the magnitude of differential magnification. If the background and foreground components are in alignment with the observers line of sight the differential magnification effect is minimized. As the spatial offset grows so does the magnification of the shorter wavelength more compact regions until the strong lensing gives way to weak lensing when the impact parameter becomes too large.

The mid-IR regime tends to follow the same route as the far-IR regime in our simulations. For the sake of properly de-magnifying the emission from PAHs and other mid-IR light,

using the magnification of the dust emission appears to be a prudent choice compared with the stellar emission.

We model the spectral energy distribution for the lensed galaxies using the Multi-wavelength Analysis of Galaxy Physical Properties (MAGPHYS) software (da Cunha et al., 2008). The sample used in this study are a representation of high-z dusty galaxies and so the newer HIGHZ model library of MAGPHYS is utilized (da Cunha et al., 2015). The MAGPHYS package compares model SEDs to the observed fluxes of galaxies. In this case the observed fluxes are the emission output from the SKIRT modeling.

MAGPHYS outputs include, the estimated stellar mass of the galaxy as well as the star-formation rate. The estimation of these values are based partially on the stellar vs. dust emission observed. With respect to differential magnification it is useful to see how much the magnification difference will effect these results. Typically, if only stellar emission observations or only dust emission observations are available, then the lens model is performed using one component and then the flux is de-magnified at that value across all wavelengths.

If the stellar emission is at a higher magnification on average than the dust emission then if one divides by the stellar magnification then the dust will be underestimated or if one divides by the dust magnification then the stellar emission will be overestimated. This will have a measurable effect on the outputs of MAGPHYS. To test this and see the effect of differential magnification on the observations of these simulated galaxies the fluxes were passed through the MAGPHYS program.

The results are shown in Figure 4.8. On the left side of Figure 4.8 the "true" value of the SED, the SED when differential magnification is taken into account, is plotted against if the observed fluxes were de-magnified by the stellar magnification. The right side of the figure is showing the result if the observed flux was de-magnified by the dust magnification compared with the true value. It is important to note that in the case of the figure $\frac{\mu_{\rm dust}}{\mu_{\rm stars}} = 0.5$.

The star-formation rate vs. stellar mass is plotted in Figure 4.9. The green point represents the model when the stellar and dust emission are correctly de-magnified by wavelength. The blue points represent when only the stellar model is used while the red points correspond to when the dust magnification is used to de-magnify. The differing symbols show the effect for different values of $\frac{\mu_{\text{stars}}}{\mu_{\text{dust}}}$. When the stellar components of the galaxy are more compact than the dust components as seen in the simulation as well as observation we see that the IR luminosity is underestimated in the models in which the light is de-magnified by the stellar model. This translates to an underestimation of the SFR in the stellar models. For the SEDs de-magnified using the dust model there is a rise in the luminosity from the optical and near IR wavelengths compared with the true value. In the SED this translates to an overestimation of the total stellar mass of the galaxy.

In either case the SFR or stellar mass is affected by approximately the same factor as the stellar to dust magnification ratio.The overall trend in diagnosing the effect of differential magnification on galaxy studies of dusty high redshift star forming galaxies is that there is an underestimation of the ratio of SFR to stellar mass.

4.7 Summary

FIRE-2 cosmological simulations were used in order to model the light coming from sub-millimeter bright galaxies in order to recreate and study the effect of differential magnification. The light was passed through lens models in order to estimate the magnification factor as a function of wavelength to determine if the magnification difference as seen in observations can be recovered through simulation. The resulting difference in magnification was compared to observation and it was found to be in agreement with observed galaxies. The effect of compactness on magnification was studied and as expected the more compact regions of the simulated galaxies experienced a higher level of magnification than the ex-

tended regions. This led to a higher magnification at shorter wavelengths from the more compact stellar regions than the longer wavelength light coming from the more extended regions of dust. Three components can change the differential magnification. Having the source and lens be physically offset, having the lens be closer to the source than the observer and increasing the mass of the lens all contribute to a greater magnification of the stellar light vs. the dust emission intensifying the differential magnification effect. When deriving the physical properties of galaxies from model SEDs we find that the overall effect of differential magnification is an underestimation of the ratio of star-formation rate to stellar mass that is equivalent to the ratio of stellar magnification to dust magnification.

Chapter 5

Halo Pressure Profile through the Skew Cross-Power Spectrum of Sunyaev-Zel'dovich Effect and CMB Lensing in *Planck*

We measure the Cosmic Microwave Background (CMB) skewness power spectrum in *Planck*, using frequency maps of the HFI instrument and the Sunyaev-Zel'dovich (SZ) component map. The two-to-one skewness power spectrum measures the cross-correlation between CMB lensing and the thermal SZ effect. We also directly measure the same cross-correlation using *Planck* CMB lensing map and the SZ map and compare it to the cross-correlation derived from the skewness power spectrum. We model fit the SZ power spectrum and CMB lensing-SZ cross power spectrum via the skewness power spectrum to constrain the gas pressure profile of dark matter halos. The gas pressure profile is compared to existing measurements in the literature including a direct estimate based on the stacking of SZ clusters in *Planck*.

5.1 Background

The importance of the *Planck* mission (Planck Collaboration et al., 2011a) to cosmology can not be overstated. The measurement of cosmic microwave background (CMB) anisotropies has allowed for increased accuracy in measurements of cosmological parameters. Going beyond primary anisotropies *Planck* frequency maps can be used to probe higher order correlations that arise from secondary effects like the Sunyaev-Zel'dovich (SZ) effect (Sunyaev & Zeldovich, 1980), integrated Sachs-Wolfe effect (ISW) (Sachs & Wolfe, 1967) and gravitational lensing (Smith et al., 2007) among others.

The SZ effect is the result of inverse Compton scattering of photons off free electrons. The SZ effect on the CMB is proportional to the integrated electron pressure inside galaxy clusters. Measurement of the SZ effect is a key tracer of the hot electron gas in the intra-cluster medium (ICM). Due to its unique frequency spectrum relative to CMB black-body the thermal SZ effect can be separated in multi-frequency CMB maps (Cooray et al., 2000). Gravitational lensing of the CMB is caused by the intervening mass distribution and is a tracer of the line of sight projected matter potential. The integrated lensing map can be extracted from a quadratic (Okamoto & Hu, 2003) and likelihood (Hirata et al., 2008) estimators on CMB. A non-zero correlation between the lensing effect and the SZ effect establishes the relationship between dark matter and hot intra-cluster gas (Hill & Spergel, 2014). This is an excellent probe of the large scale distribution of gas. Several studies have attempted to look at this correlation (Cooray et al. 2000; Hill & Spergel 2014) including one using the WMAP data (Calabrese et al., 2010). Here we update the previous work by incorporating data from *Planck*.

The cross-correlation between CMB lensing and thermal SZ results in a non-Gaussian signal at the three-point level of the correlation function (Spergel & Goldberg 1999; Cooray et al. 2000). While challenging to measure directly the bispectrum can be collapsed into a sum of

two-point functions in what is known as the skewness power spectrum involving a squared temperature-temperature correlation. As has been shown in previous work (Cooray 2001; Munshi et al. 2011) the skewness spectrum, related to the CMB-CMB lensing-SZ bispectrum, can be probed through the cross-correlation of a temperature squared map and a map of the SZ effect. This skewness spectrum contains all the information from the bispectrum once the estimator is appropriately weighted. The three point correlation function using only the CMB is an independent look at the lensing-SZ cross-correlation.

The amplitude of the non-Gaussian signals arising from the SZ effect can help constrain physical properties of the large scale structure of the Universe. Specifically, we consider here the gas pressure profile within galaxy clusters as a function of radius from the dark matter halo. Having a three point correlation between the lensing and SZ effect can constrain parameters in the pressure profile model to reveal new physics regarding the relationship between dark matter and gas pressure.

The gas pressure profile of the ICM can be derived from the Navarro-Frenk-White (gNFW) profile assuming hydrostatic equilibrium (Navarro et al. 1996; Komatsu & Seljak 2001). Such a profile for the gas takes the form

$$\tilde{P}(x) = \frac{P_0}{(c_{500}x)^{\gamma}[1 + (c_{500}x)^{\alpha}]^{(\beta-\gamma)/\alpha}}, \tag{5.1}$$

The gas pressure profile is fully determined by the parameter set $\{P_0, c_{500}, \alpha, \beta, \gamma\}$ which are the central pressure, concentration, central slope, intermediate slope and outer slope of the ICM pressure, respectively (Nagai et al., 2007). The gas pressure profile of galaxy clusters and its relation to the SZ effect has been studied by several groups including Arnaud et al. (2010) and Planck Collaboration et al. (2013). In Planck Collaboration et al. (2013) the

reconstructed SZ map was used to study the pressure of 62 massive clusters. By stacking radial profiles, the gas pressure profile was measured and the best fit parameters were found to be $[P_0, c_{500}, \alpha, \beta, \gamma] = [6.41, 1.81, 1.33, 4.13, 0.31]$. It was found that at large radii the pressure profile was flatter than simulations would predict. In Arnaud et al. (2010), simulations and observations of 33 clusters from XMM-Newton are used to create a profile for gas pressure and the resulting parameters are $[P_0, c_{500}, \alpha, \beta, \gamma] = [8.40, 1.18, 1.05, 5.49, 0.308]$. Recent work by Sayers et al. (2013) concluded that higher mass and larger redshift did not significantly effect the pressure profile. Sayers et al. (2013) used 45 massive galaxy clusters at $0.15 < z < 0.88$ and found the pressure profile parameters to be $[P_0, c_{500}, \alpha, \beta, \gamma] = [4.29, 1.18, 0.86, 3.67, 0.67]$. The CMB bispectrum measurement can be a complementary way to constrain the gas pressure parameters and provide additional observational evidence for probing the gas pressure profile.

The chapter is organized as follows: in the next section we discuss the skewness estimator and its derivation. In section 5.3 we review the data analysis preformed. In section 5.4 the results of the analysis are presented. In section 5.5 the MCMC analysis is discussed along with the results and their cosmological implications. Section 5.6 is a summary of the findings and suggestions for future work. Throughout we make use of the standard flat-ΛCDM cosmological model with H_0= 70 km s^{-1} Mpc^{-1} and Ω_Λ=0.73.

5.2 Estimator

The derivation of the bispectrum and the skewness spectrum are discussed at length in several papers including Cooray (2001) and more recently Munshi et al. (2011). Here the authors cover the key points for this analysis and refer the reader to the previous work for a more detailed discussion. The angular bispectrum $B^{TTy}_{\ell_1\ell_2\ell_3}$ is defined as a triangle with sides (ℓ_1,ℓ_2,ℓ_3) in multipole space where $T(\mathbf{n})T(\mathbf{n})$ and $y(\mathbf{n})$ are statistically isotropic fields.

With T representing a temperature map and y representing the SZ y-component map. The bispectrum is related to the multipole moments of the fields by:

$$B^{TTy}_{\ell_1\ell_2\ell_3} = \sum_{m_1 m_2 m_3} \begin{pmatrix} \ell_1 & \ell_2 & \ell_3 \\ m_1 & m_2 & m_2 \end{pmatrix} \qquad \langle a^T_{\ell_1 m_1} a^T_{\ell_2 m_2} a^y_{\ell_3 m_3} \rangle \tag{5.2}$$

The skewness power spectrum is the correlation of the product map $T(\mathbf{n})T(\mathbf{n})$ and $y(\mathbf{n})$. This is useful because the angular bispectrum $B^{TTy}_{\ell_1\ell_2\ell_3}$ can be difficult to measure fully. The skewness spectrum $C^{TT,y}_{\ell}$ is a summation of the triangular configurations keeping one of the sides length ℓ fixed. Following the discussion in Cooray 2001; Munshi et al. 2011; Calabrese et al. 2010 the bispectrum can be described by:

$$\begin{aligned} B^{TTy}_{\ell_1\ell_2\ell_3} &= -[C^{\phi y}_{\ell_1} C_{\ell_1} \frac{\ell_2(\ell_2+1) - \ell_1(\ell_1+1) - \ell_3(\ell_3+1)}{2} \\ &+ \text{perms.}] \sqrt{\frac{(2\ell_1+1)(2\ell_2+1)(2\ell_3+1)}{4\pi}} \begin{pmatrix} \ell_1 & \ell_2 & \ell_3 \\ 0 & 0 & 0 \end{pmatrix} \end{aligned} \tag{5.3}$$

Here $C^{\phi y}_{\ell}$ is the amplitude of the cross-correlation power spectrum between the lensing potential and the y-parameter map and C_{ℓ_1} is the unlensed CMB anisotropy power spectrum. Only the permutations in which ℓ_1 and ℓ_2 vary are used since ℓ_3 remains tied to the secondary anisotropy and is fixed to relate to the skewness spectrum.

From Munshi et al. 2011; Calabrese et al. 2010 the optimized skewness estimator begins with defining a set of nine weighted temperature maps:

$$\begin{aligned} X^1_{\ell m} &= \frac{a_{\ell m}}{\tilde{C}_\ell} C_\ell; Y^1_{\ell m} = \ell(\ell+1)\frac{a_{\ell m}}{\tilde{C}_\ell}; Z^1_{\ell m} = \frac{a_{\ell m}}{\tilde{C}_\ell} C^{\phi y}_\ell \\ X^2_{\ell m} &= -\ell(\ell+1)\frac{a_{\ell m}}{\tilde{C}_\ell} C_\ell; Y^2_{\ell m} = \frac{a_{\ell m}}{\tilde{C}_\ell}; Z^2_{\ell m} = \frac{a_{\ell m}}{\tilde{C}_\ell} C^{\phi y}_\ell \\ X^3_{\ell m} &= \frac{a_{\ell m}}{\tilde{C}_\ell} C_\ell; Y^3_{\ell m} = \frac{a_{\ell m}}{\tilde{C}_\ell}; Z^3_{\ell m} = -\ell(\ell+1)\frac{a_{\ell m}}{\tilde{C}_\ell} C^{\phi y}_\ell \end{aligned} \tag{5.4}$$

Where $\tilde{C}_\ell = C_\ell + N_\ell / b^2_\ell$ is the temperature power spectrum, b_ℓ is the beam transfer function and N_ℓ is the noise power spectrum. The nine weighted maps are generated by $T^{(i)}(\mathbf{n}) = \sum Y_{\ell m}(\mathbf{n}) T^{(i)}_{\ell m}$ where i is the index of the weighted map from above. The optimized skew spectrum is defined as:

$$C^{XY,Z}_\ell = \frac{1}{2\ell+1} \sum_i \sum_m \mathrm{Real}[(\mathrm{X^{(i)}}(\mathbf{n})\mathrm{Y^{(i)}}(\mathbf{n}))_{\ell \mathrm{m}} \mathrm{Z^{(i)}}(\mathbf{n})_{\ell \mathrm{m}}] \tag{5.5}$$

The measured skewness spectrum $\hat{C}^{TT,y}_\ell$ now can be related to the bispectrum as shown in Cooray 2001; Munshi et al. 2011 as:

$$\hat{C}^{XY,Z}_\ell = \frac{1}{2\ell+1} \sum_{\ell_1 \ell_2} \frac{\hat{B}_{\ell \ell_1 \ell_2} B_{\ell \ell_1 \ell_2}}{\tilde{C}_\ell \tilde{C}_{\ell_1} \tilde{C}_{\ell_2}} \tag{5.6}$$

Here $\hat{B}_{\ell\ell_1\ell_2}$ is the reduced bispectrum, meaning it has been weighted as the maps have in the derivation of $C_\ell^{TT,y}$ and the calculation only includes the permutations in which ℓ_3 is fixed. The range of ℓ is $2 < \ell < 1600$.

Now the measured skewness spectrum $\hat{C}_\ell^{TT,y}$ can be related to the theoretical $C_\ell^{TT,y}$. The theory $C_\ell^{TT,y}$ is calculated analytically by plugging the bispectrum formulation in Equation 2 into Equation 5. Up to this point the amplitude of the lensing SZ cross-correlation $C_\ell^{\phi y}$ has been taken to be unity. While the measured spectrum contains one factor of $C_\ell^{\phi y}$ and one factor of $\hat{C}_\ell^{\phi y}$, the theory spectrum contains two factors of $C_\ell^{\phi y}$. The ratio of the measured and theoretical spectra gives the measured lensing SZ cross-correlation $\hat{C}_\ell^{\phi y}$.

5.3 Data Analysis

For the purposes of this analysis the *Planck* PR2-2015 all sky maps were used. Specifically the 100 GHz, 143G Hz and 217 GHz temperature maps were used as well as the MILCA full mission y-map component foreground map. The data were reduced using custom python scripts within the HEALPY[1] (Górski et al., 2005) code framework. Briefly, the temperature maps were masked using a combination of Galactic foreground mask and the *Planck* released point source map. The 60% foreground mask in conjunction with a point source mask was utilized in order to mask out any contamination by the Milky Way galaxy and bright sources. The monopole signal as well as the dipole signal were modeled using HEALPY and removed before measuring the power spectrum.

In order to measure the noise N_ℓ for the temperature maps 100 *Planck* released simulated noise maps were passed through the analysis pipeline and the resulting median power spectrum was determined to be the noise contribution to the measured power spectrum. The CMB anisotropy power spectrum C_ℓ was generated using the CAMB (Lewis, 2013) code, the

[1] http://healpix.sourceforge.net

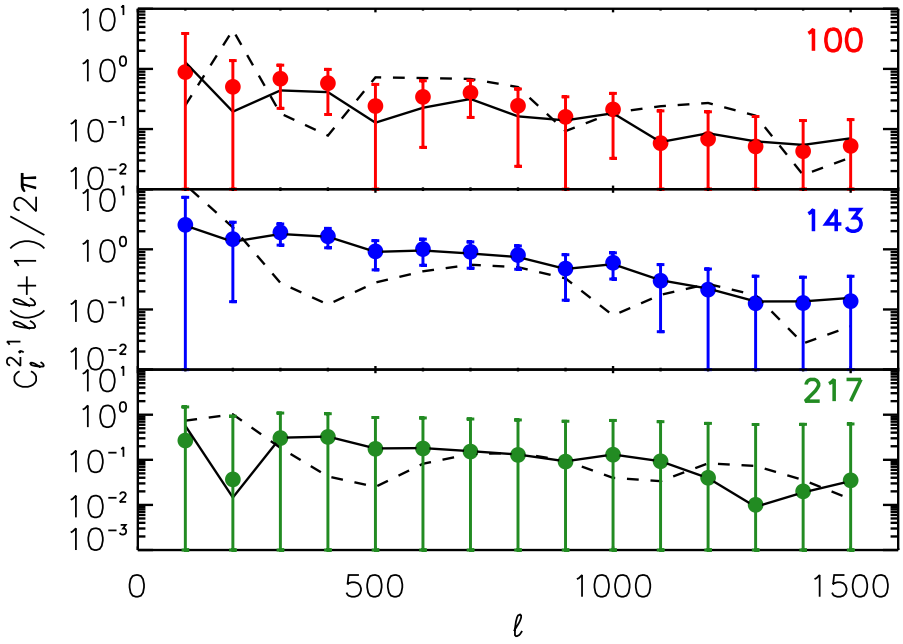

Figure 5.1: The measured skewness spectrum for each of the three frequencies. 100 GHz, 143GHz and 217 GHz from top to bottom respectively. The contributions of the dust signal and the SZ signal in the temperature maps are plotted as well. The dashed line is the resulting spectrum after subtracting the *Planck* dust map from the y-parameter map. The solid line is the resulting spectrum after having subtracted the frequency corrected y-map from the temperature map.

result of which was in agreement with the measured CMB power spectrum released by the *Planck* team. To model the noise in the y-map, the *Planck* released MILCA homogeneous noise power spectrum was used.

To measure the direct cross-correlation between lensing and tSZ (Spergel & Goldberg, 1999), the *Planck* released lensing map was similarly masked before being cross correlated with the component y-map to measure $C_\ell^{\phi y}$. To measure the dust contamination the *Planck* released dust map was used and subtracted from the temperature maps before being run through the data pipeline.

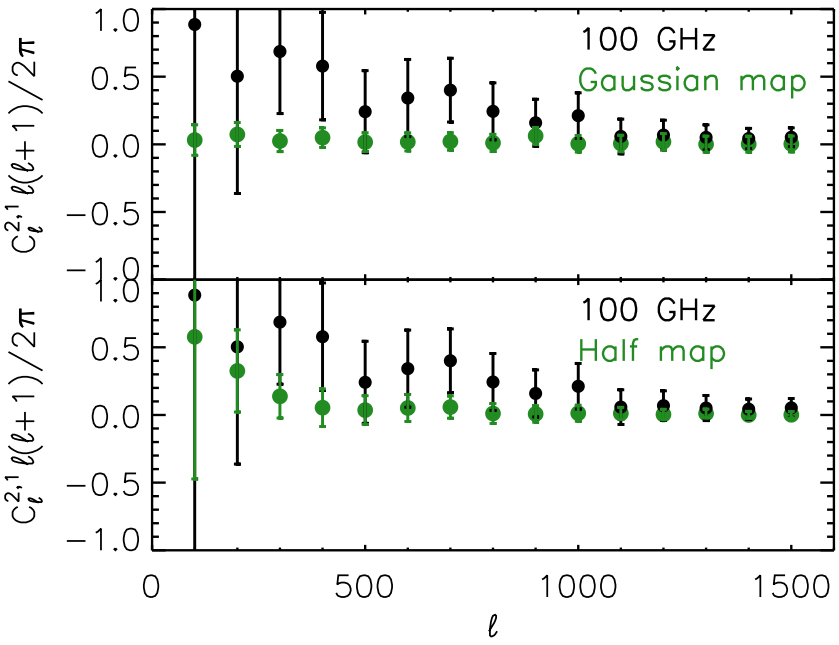

Figure 5.2: The result of passing a Gaussian map with noise through the estimator and the result of passing the half-map difference through the estimator. For comparison, the 100 GHz skewness spectrum is plotted. Both results are consistent with a null result as would be expected.

5.4 Results

In Figure 5.1 we show the resulting skewness power spectra from the different frequencies with error bars from the simulated noise maps as well as cosmic variance. While there is a similar signal in the 100 and 143 GHz spectra the 217 GHz spectrum shows a deficiency. This is due to the SZ effect being frequency dependent with a smaller signal at 217 GHz compared to 100 and 143 GHz. Also plotted are the contribution of the dust and SZ effect on the temperature maps. The dashed line represents the skewness power spectra when the *Planck* dust map is subtracted from the y-parameter map before being correlated with the temperature squared map. From the results it doesn't appear that the dust contribution to the y-parameter map is significant. The solid line represents subtracting a scaled y-parameter map from the temperature maps before squaring them and correlating with the y-parameter map. The solid line shows that the SZ signal does not contaminate the temperature maps.

Subtracting the dust map from the y-parameter map is a test for the CIB contamination in the y-map as dust us a tracer of the CIB. While the subtracted dust map skewness spectra do not show a statistically significant difference from the non-subtracted spectra it is worth noting that removing the CIB leakage from the it y-map is a difficult task and has been the subject of analysis in several articles Hill & Spergel 2014; Planck Collaboration et al. 2016b. In Planck Collaboration et al. (2016c) the correlation between the SZ effect and the CIB is measured. From those results, the CIB contamination contribute as much as 20% of the signal at intermediate and small angular scales.

The results of the data pipeline null test are shown in Figure 5.2. The upper part shows the result when passing a simple Gaussian map with simulated noise through the pipeline. The bottom part shows the result when using a map made up of the difference between two half-maps. For comparison, the 100 GHz spectrum is plotted. If there is no systematic contribution to the signal in the data pipeline both the Gaussian and half-map spectra

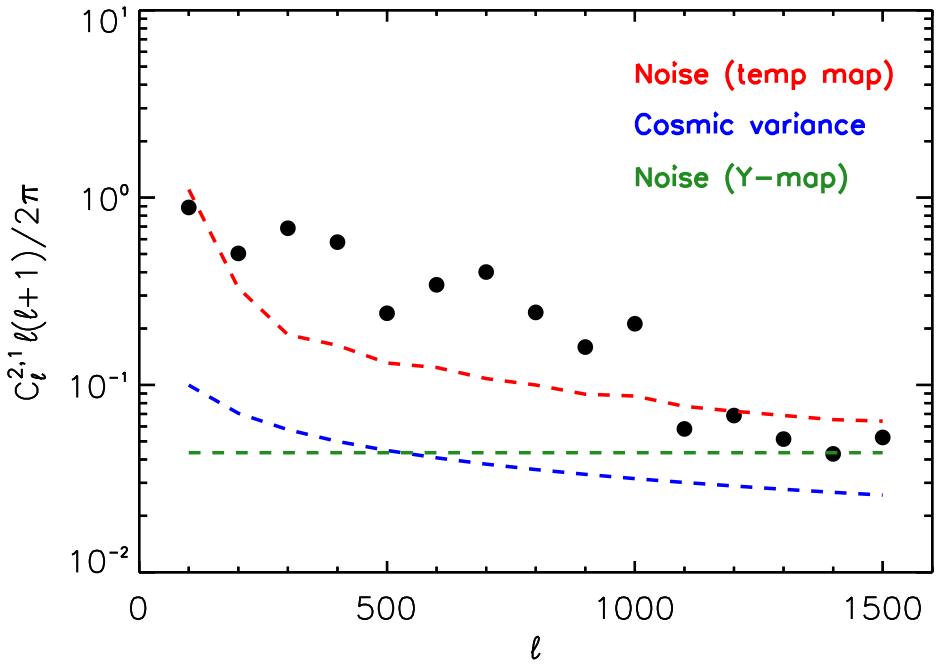

Figure 5.3: The component contributions to the total error. The 100 GHz spectrum is shown as an example which is representative of all three frequencies.

should be consistent with zero. While the error is large in the half-map spectrum, both results show that the signal in the 100 GHz spectrum is not coming from systematics and is non-vanishing.

The contributions from various error estimates are plotted in Figure 5.3. In the figure the 100 GHz skewness spectrum is plotted and is representative of the other frequencies. To estimate the error contribution from the temperature maps, 100 *Planck* simulated noise maps at each frequency were passed through the data pipeline. The standard deviation of the resulting power spectra became the error estimate. The dominate source of error is from the simulated temperature noise maps while the noise contribution from the y-parameter map is not as significant. The contribution from cosmic variance is not significant. At high ℓ all of the noise contributions become significant with the temperature map noise rising above the signal. Figure 5.4 contains a histogram plot of the skew spectrum value at $\ell = 1000$ for

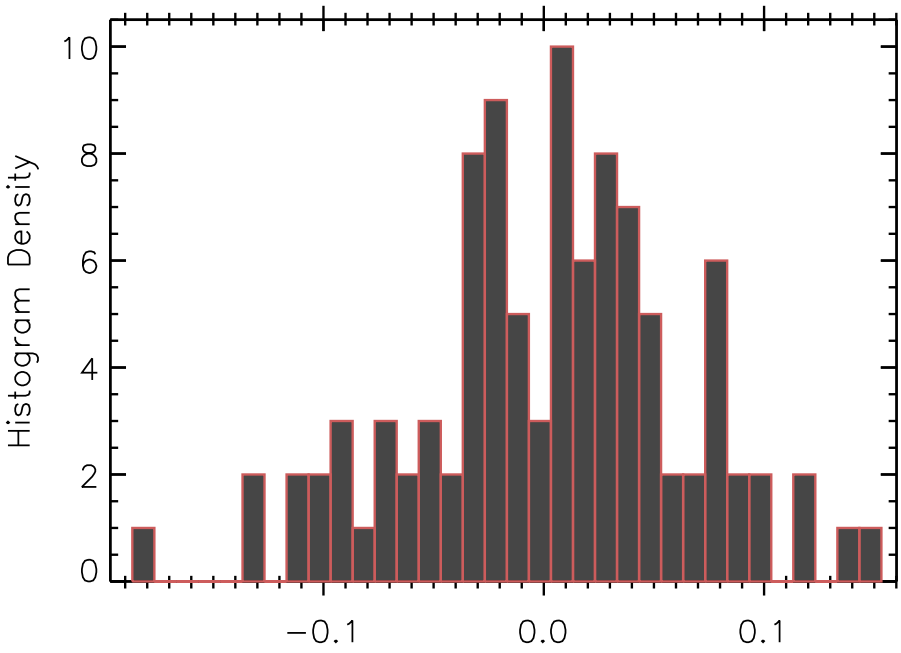

Figure 5.4: A histogram of the variance in the signal of the simulated noise. 100 simulated maps were put through the same estimator as the data and the value at $\ell = 1000$ is plotted here.

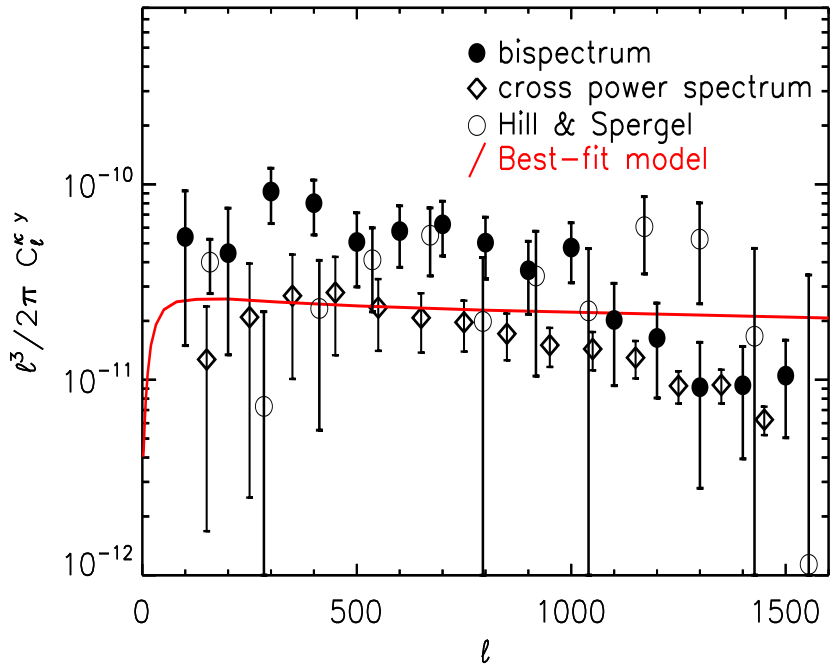

Figure 5.5: The best fit model for the cross power spectrum $C_\ell^{\kappa y}$ is plotted in red. The model is compared to the measured cross power spectrum from the skew spectrum analysis, the direct cross power spectrum of the *Planck* lensing map with the y-parameter map. The results from Hill & Spergel (2014) are shown as a comparison, being the direct two point lensing-SZ cross correlation and the y-map auto spectrum from the generated maps therein.

the 100 GHz simulated noise maps is shown. The noise contribution is almost Gaussian as expected over 100 simulated maps.

5.5 MCMC and Model Interpretation

Figure 5.5 and Figure 5.6 show the measured three point lensing convergence-SZ cross-correlation power spectrum $C_\ell^{\kappa y}$ and the measured two point y-parameter auto power spectrum C_ℓ^{yy}. From the Monte Carlo Markov Chain (MCMC) procedure, we obtain the best fit models for each case and have plotted the result. The measured lensing-SZ cross-correlation comes from the resulting skewness power spectra which has been averaged over the three

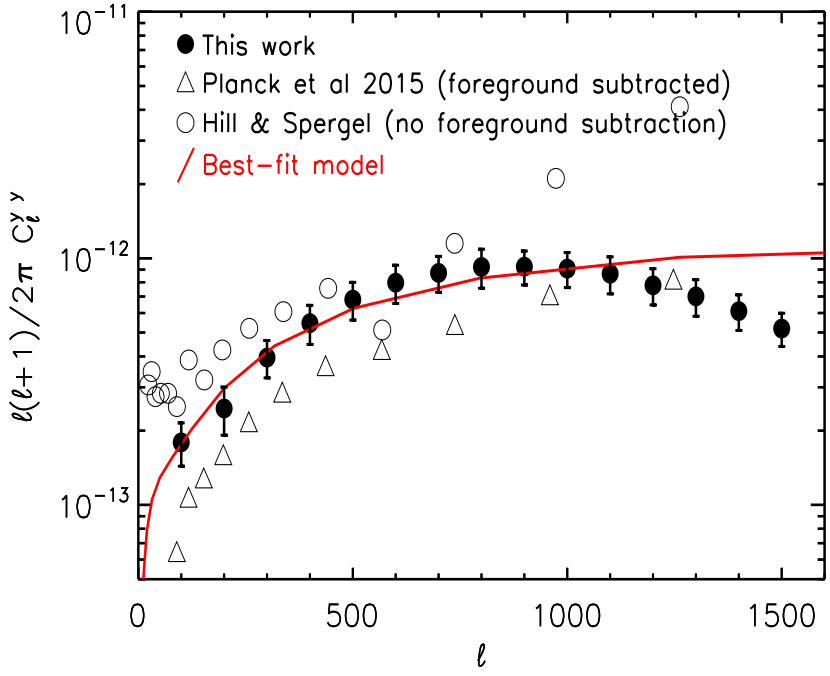

Figure 5.6: The best fit model for the auto power spectrum C_ℓ^{yy} is plotted in red. The model is compared with the auto power spectrum of the *Planck* y-parameter maps. The results from Hill & Spergel (2014) as well as Planck Collaboration et al. (2016b) are shown as a comparison, being the direct two point lensing-SZ cross correlation and the y-map auto spectrum from the generated maps therein. The error bars for Planck Collaboration et al. (2016b) are smaller than the symbols used in the plot.

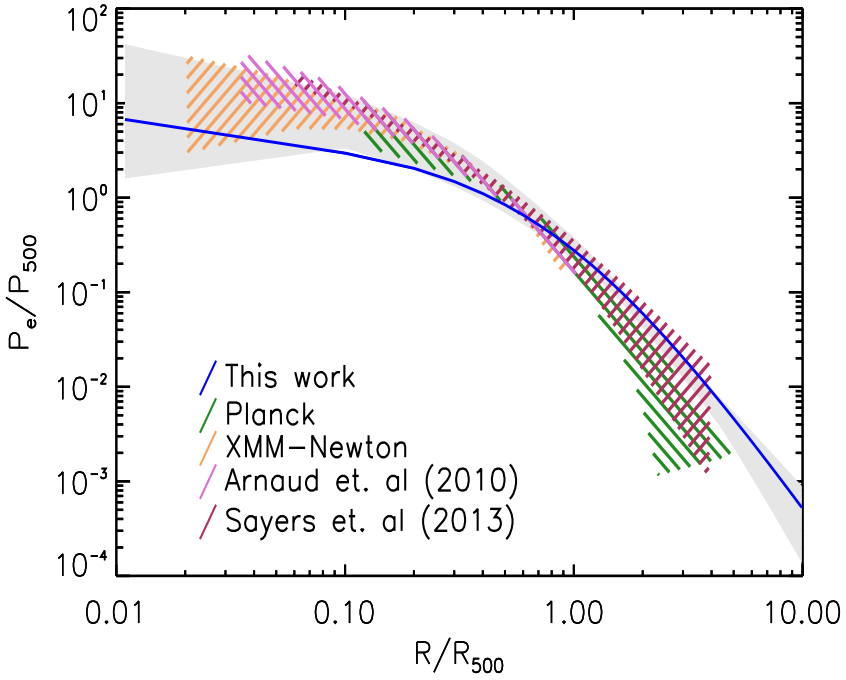

Figure 5.7: The best fit model of the gas pressure $P_e(r)$ including the 1σ confidence region shown by the shaded region. For comparison the pressure profiles measured in Planck Collaboration et al. 2013; Arnaud et al. 2010; Sayers et al. 2013 are also shown as a 1σ region.The pressure profiles have been set to $z = 0$ for comparison.

frequency bands with error added in quadrature. Because of the noise dominance the covariance in error between the three frequencies is not significant and is neglected. Also shown is the measured cross correlation of the *Planck* lensing map with the y-parameter map as well as the two point lensing-SZ cross correlation measured in Hill & Spergel (2014). The two point y-parameter auto power spectrum is measured by taking the auto-spectrum of the *Planck* y-parameter map. For comparison the Hill & Spergel (2014) auto spectrum is shown as well as the Planck Collaboration et al. (2016b) auto spectrum. The spectrum from Hill & Spergel (2014) can be considered as a raw spectrum with no foreground subtraction while the Planck Collaboration et al. (2016b) spectrum has had foreground contaminants removed. See Planck Collaboration et al. (2016b) for more details. At intermediate and small angular scales the raw spectrum includes contributions from the CIB while the foreground subtracted spectrum does not.

The best fit model for the gas pressure from the three-point correlation is shown in Figure 5.7 along with the 1σ confidence region. For comparison gas pressure profiles from *Planck* and XMM-*Newton* are shown (Planck Collaboration et al., 2013; Arnaud et al., 2010) as well as the higher z clusters from Sayers et al. (2013).

We follow the gas pressure model in Arnaud et al. (2010), i.e.,

$$\begin{aligned} P_e(r) &= 1.65 h_{70}^2 E^{8/3}(z) [\frac{M_{500}}{3 \times 10^{14} M_\odot / h_{70}}]^{2/3+\alpha_P} \\ &\times \tilde{P}(x) \ [\mathrm{eV/cm^3}]. \end{aligned} \tag{5.7}$$

Here $E(z) = H(z)/H_0$, $h_{70} = h/0.7$ and $\alpha_P = 0.12$. We determine the radius r_{500} from the relation $M_{500} = 4\pi/3[500\rho_c(z)]r_{500}^3$. In this equation, $\rho_c(z)$ is the critical density and $x = r/r_{500}$.

We use the halo model (Cooray & Sheth, 2002) to predict the theoretical power spectra C_ℓ^{yy} and $C_\ell^{\kappa y}$ following the calculations of 1-halo and 2-halo terms (Planck Collaboration et al., 2014; Hill & Spergel, 2014; Battaglia et al., 2015). The gas pressure profile in this work is taken from Arnaud et al. (2010) and Ma et al. (2015), where the parameter set is assumed to be independent of mass and redshift. While in Battaglia et al. (2015), some of the parameters can vary with mass and redshift and they verified that the halo model calculation was largely consistent with the measurements from numerical simulations. We do not expect significant differences between these gas pressure models, given the weak dependence on the mass and redshift and the limited constraining power of the measured cross-power spectrum. However, to produce the most precise gas pressure profile, one has to rely on numerical simulations. We compare the theoretical power spectra of both C_ℓ^{yy} and $C_\ell^{\kappa y}$ to the measured ones, sampling the gas pressure profiles and generating posterior distribution functions from the following likelihood

$$-2\ln\mathcal{L} = \sum_{i=\kappa y, yy}\sum_{b}\Big[\frac{C_b^{\mathrm{obs,(i)}} - \hat{C}_b^{(i)}}{\Delta_b}\Big]^2 + \mathrm{const.} \tag{5.8}$$

Such a MCMC procedure generates a sufficient amount of samples of the parameters for the gas pressure profile, among which we can obtain the best fit model corresponding to the smallest chi-square. In Figure 5.5 and 5.6, we show the best fit model for the Planck lensing and tSZ, while in Van Waerbeke et al. (2014), a similar analysis was performed with the shear measurements of Canada France Hawaii Telescope Lensing Survey and a newly-constructed tSZ map from Planck.

5.6 Discussion

As demonstrated, the three-point measurement from the skew spectrum is in agreement with the two-point direct measurement from Hill & Spergel (2014). It serves as an independent check on the work done before and can be used to constrain physical properties like the gas pressure profile. The non-zero result confirms the correlation between dark matter CMB lensing and the hot ICM traced by the thermal SZ effect.

Using only the CMB, the gas pressure profile is examined as a separate check on the work done by observing clusters directly or by simulation. The resulting gas pressure profile from the MCMC procedure is defined by the parameters $\{P_0, c_{500}, \alpha, \beta, \gamma\}$ are $\{5.1^{+2.0}_{-1.8},\ 1.7^{+0.6}_{-0.5},\ 1.2^{+0.5}_{-0.3},\ 3.2^{+0.4}_{-0.3},\ 0.3^{+0.2}_{-0.1}\}$. These parameters are in agreement with the literature in which observations and simulations are conducted to measure the profile.

It should be noted that Planck Collaboration et al. (2013), Arnaud et al. (2010) and Sayers et al. (2013) are probing high mass clusters while the cross spectrum is more sensitive to the lower mass clusters (Battaglia et al., 2015). While Sayers et al. (2013) found that the gas pressure profile is nearly universal over a wide range of mass/redshift, simulations have shown that the profile can be sensitive to these parameters (Le Brun et al., 2015).

As can be seen in Figure 5.7 the pressure profile from this work is in agreement with the work done by observations from *Planck*, XMM-*Newton*, *Chandra* as well as simulations. Considering the differences in mass between this work and the observational/simulation work in the literature, the gas pressure profiles are of a similar shape within 1σ. This would lend credence to the idea that the gas pressure profile is more universal over a wide range of mass/redshift. As a check the two point correlation was also modeled for the pressure profile and found to not vary significantly from the three-point model.

5.7 Summary

The CMB skewness power spectrum was measured using the correlation between *Planck* frequency maps and *Planck* Sunyaev-Zel'dovich (SZ) component maps. We also measure the lensing-thermal SZ cross-correlation power spectrum using the three-point correlation function (bispectrum) and compare it to the two-point correlation direct measurements from *Planck* all sky maps.

The Markov Chain Monte Carlo (MCMC) procedure is utilized in order to find the best fit lensing cross-correlation power spectrum as well as the best fit y-parameter auto-spectrum. The best fit and uncertainty values for the gas pressure parameters are found to be $\{P_0, c_{500}, \alpha, \beta, \gamma\}$ are $\{5.1^{+2.0}_{-1.8}, 1.7^{+0.6}_{-0.5}, 1.2^{+0.5}_{-0.3}, 3.2^{+0.4}_{-0.3}, 0.3^{+0.2}_{-0.1}\}$ Where $P_0, c_{500}, \alpha, \beta$ and γ are the central pressure, concentration, central slope, intermediate slope and outer slope respectively. The parameters are found to be in agreement with literature.

Bibliography

Amblard, A., Cooray, A., Serra, P., et al. 2010, *Astro. Astrophys.*, 518, L9

Anglés-Alcázar, D., Faucher-Giguère, C.-A., Kereš, D., et al. 2017, *Mon. Not. Royal Astron. Soc.*, 470, 4698

Arnaud, M., Pratt, G. W., Piffaretti, R., et al. 2010, *Astro. Astrophys.*, 517, A92

Baes, M., Verstappen, J., De Looze, I., et al. 2011, *Astrophys. J. Suppl.*, 196, 22

Baldwin, J. A., Phillips, M. M., & Terlevich, R. 1981, PASP, 93, 5

Banerji, M., Chapman, S. C., Smail, I., et al. 2011, *Mon. Not. Royal Astron. Soc.*, 418, 1071

Bartelmann, M., & Narayan, R. 1995, in American Institute of Physics Conference Series, Vol. 336, Dark Matter, ed. S. S. Holt & C. L. Bennett, 307–319

Bartelmann, M., & Schneider, P. 2001, Phys. Rep., 340, 291

Battaglia, N., Hill, J. C., & Murray, N. 2015, *Astrophys. J.*, 812, 154

Bertin, E., & Arnouts, S. 1996, *Astro. Astrophys. Suppl.*, 117, 393

Blain, A. W. 1996, *Mon. Not. Royal Astron. Soc.*, 283, 1340

—. 1999, *Mon. Not. Royal Astron. Soc.*, 304, 669

Blandford, R. D., & Narayan, R. 1992, *Ann. Rev. of Astron. Astrophys.*, 30, 311

Bothwell, M. S., Smail, I., Chapman, S. C., et al. 2013, *Mon. Not. Royal Astron. Soc.*, 429, 3047

Bourne, N., Dunne, L., Ivison, R. J., et al. 2011, *Mon. Not. Royal Astron. Soc.*, 410, 1155

Bussmann, R. S., Dey, A., Armus, L., et al. 2012, *Astrophys. J.*, 744, 150

Bussmann, R. S., Pérez-Fournon, I., Amber, S., et al. 2013, *Astrophys. J.*, 779, 25

Calabrese, E., Smidt, J., Amblard, A., et al. 2010, Phys. Rev. D, 81, 043529

Calanog, J. A., Fu, H., Cooray, A., et al. 2014, *Astrophys. J.*, 797, 138

Calzetti, D. 2001, PASP, 113, 1449

Canameras, R., Nesvadba, N. P. H., Guery, D., et al. 2015, ArXiv e-prints, arXiv:1506.01962

Casey, C. M., Narayanan, D., & Cooray, A. 2014, Phys. Rep., 541, 45

Casey, C. M., Chen, C.-C., Cowie, L. L., et al. 2013, *Mon. Not. Royal Astron. Soc.*, 436, 1919

Chabrier, G. 2003, PASP, 115, 763

Chapman, S. C., Blain, A. W., Smail, I., & Ivison, R. J. 2005, *Astrophys. J.*, 622, 772

Condon, J. J. 1992, *Ann. Rev. of Astron. Astrophys.*, 30, 575

Conroy, C., Dutton, A. A., Graves, G. J., Mendel, J. T., & van Dokkum, P. G. 2013, *Astrophys. J.*, 776, L26

Cooray, A. 2001, Phys. Rev. D, 64, 043516

Cooray, A., Hu, W., & Tegmark, M. 2000, *Astrophys. J.*, 540, 1

Cooray, A., & Sheth, R. 2002, Phys. Rep., 372, 1

da Cunha, E., Charlot, S., & Elbaz, D. 2008, *Mon. Not. Royal Astron. Soc.*, 388, 1595

da Cunha, E., Walter, F., Smail, I. R., et al. 2015, *Astrophys. J.*, 806, 110

Daddi, E., Dickinson, M., Morrison, G., et al. 2007, *Astrophys. J.*, 670, 156

Davé, R., Finlator, K., & Oppenheimer, B. D. 2012, *Mon. Not. Royal Astron. Soc.*, 421, 98

Davé, R., Finlator, K., Oppenheimer, B. D., et al. 2010, *Mon. Not. Royal Astron. Soc.*, 404, 1355

Dekel, A., Sari, R., & Ceverino, D. 2009, *Astrophys. J.*, 703, 785

Domínguez, A., Siana, B., Henry, A. L., et al. 2013, *Astrophys. J.*, 763, 145

Dye, S., Negrello, M., Hopwood, R., et al. 2014, *Mon. Not. Royal Astron. Soc.*, 440, 2013

Eales, S., Dunne, L., Clements, D., et al. 2010, PASP, 122, 499

Elbaz, D., Daddi, E., Le Borgne, D., et al. 2007, *Astro. Astrophys.*, 468, 33

Engel, H., Tacconi, L. J., Davies, R. I., et al. 2010, *Astrophys. J.*, 724, 233

Er, X., Ge, J., & Mao, S. 2013, *Astrophys. J.*, 770, 110

Erb, D. K., Shapley, A. E., Pettini, M., et al. 2006, *Astrophys. J.*, 644, 813

Feldmann, R., Hopkins, P. F., Quataert, E., Faucher-Giguère, C.-A., & Kereš, D. 2016, *Mon. Not. Royal Astron. Soc.*, 458, L14

Frayer, D. T., Ivison, R. J., Scoville, N. Z., et al. 1999, *Astrophys. J.*, 514, L13

Fu, H., Jullo, E., Cooray, A., et al. 2012, *Astrophys. J.*, 753, 134

Fu, H., Cooray, A., Feruglio, C., et al. 2013, *Nature*, 498, 338

Gavazzi, R., Cooray, A., Conley, A., et al. 2011, *Astrophys. J.*, 738, 125

George, R. D., Ivison, R. J., Hopwood, R., et al. 2013, *Mon. Not. Royal Astron. Soc.*, 436, L99

Gladders, M. D., Hoekstra, H., Yee, H. K. C., Hall, P. B., & Barrientos, L. F. 2003, *Astrophys. J.*, 593, 48

Gladders, M. D., & Yee, H. K. C. 2005, *Astrophys. J. Suppl.*, 157, 1

González-Nuevo, J., Lapi, A., Fleuren, S., et al. 2012, *Astrophys. J.*, 749, 65

Górski, K. M., Hivon, E., Banday, A. J., et al. 2005, *Astrophys. J.*, 622, 759

Greve, T. R., Bertoldi, F., Smail, I., et al. 2005, *Mon. Not. Royal Astron. Soc.*, 359, 1165

Greve, T. R., Vieira, J. D., Weiß, A., et al. 2012, *Astrophys. J.*, 756, 101

Griffin, M. J., Abergel, A., Abreu, A., et al. 2010, *Astro. Astrophys.*, 518, L3

Hainline, K. N., Shapley, A. E., Kornei, K. A., et al. 2009, *Astrophys. J.*, 701, 52

Hainline, L. J., Blain, A. W., Smail, I., et al. 2011, *Astrophys. J.*, 740, 96

Harris, A. I., Baker, A. J., Frayer, D. T., et al. 2012, *Astrophys. J.*, 752, 152

Hayward, C. C., & Smith, D. J. B. 2015, *Mon. Not. Royal Astron. Soc.*, 446, 1512

Hezaveh, Y. D., Marrone, D. P., & Holder, G. P. 2012, *Astrophys. J.*, 761, 20

Hill, J. C., & Spergel, D. N. 2014, J. Cosmology Astropart. Phys., 2, 030

Hirata, C. M., Ho, S., Padmanabhan, N., Seljak, U., & Bahcall, N. A. 2008, Phys. Rev. D, 78, 043520

Hodge, J. A., Carilli, C. L., Walter, F., et al. 2012, *Astrophys. J.*, 760, 11

Holland, W. S., Bintley, D., Chapin, E. L., et al. 2013, *Mon. Not. Royal Astron. Soc.*, 430, 2513

Hopkins, P. F., Kereš, D., Oñorbe, J., et al. 2014, *Mon. Not. Royal Astron. Soc.*, 445, 581

Hopkins, P. F., Wetzel, A., Kereš, D., et al. 2018, *Mon. Not. Royal Astron. Soc.*, 480, 800

Ivison, R. J., Papadopoulos, P. P., Smail, I., et al. 2011, *Mon. Not. Royal Astron. Soc.*, 412, 1913

Ivison, R. J., Smail, I., Le Borgne, J.-F., et al. 1998, *Mon. Not. Royal Astron. Soc.*, 298, 583

Ivison, R. J., Magnelli, B., Ibar, E., et al. 2010, *Astro. Astrophys.*, 518, L31

Jones, T., Ellis, R., Jullo, E., & Richard, J. 2010, *Astrophys. J.*, 725, L176

Jullo, E., Kneib, J.-P., Limousin, M., et al. 2007, New Journal of Physics, 9, 447

Kennicutt, Jr., R. C. 1998, *Ann. Rev. of Astron. Astrophys.*, 36, 189

Kewley, L. J., Dopita, M. A., Sutherland, R. S., Heisler, C. A., & Trevena, J. 2001, *Astrophys. J.*, 556, 121

Kneib, J.-P., Ellis, R. S., Smail, I., Couch, W. J., & Sharples, R. M. 1996, *Astrophys. J.*, 471, 643

Komatsu, E., & Seljak, U. 2001, *Mon. Not. Royal Astron. Soc.*, 327, 1353

Kümmel, M., Walsh, J. R., Pirzkal, N., Kuntschner, H., & Pasquali, A. 2009, PASP, 121, 59

Lapi, A., González-Nuevo, J., Fan, L., et al. 2011, *Astrophys. J.*, 742, 24

Lawrence, A., Warren, S. J., Almaini, O., et al. 2007, *Mon. Not. Royal Astron. Soc.*, 379, 1599

Le Brun, A. M. C., McCarthy, I. G., & Melin, J.-B. 2015, *Mon. Not. Royal Astron. Soc.*, 451, 3868

Le Floc'h, E., Papovich, C., Dole, H., et al. 2005, *Astrophys. J.*, 632, 169

Leitherer, C., Schaerer, D., Goldader, J. D., et al. 1999, *Astrophys. J. Suppl.*, 123, 3

Lewis, A. 2013, Phys. Rev., D87, 103529

Lilly, S. J., Eales, S. A., Gear, W. K. P., et al. 1999, *Astrophys. J.*, 518, 641

Ma, B., Cooray, A., Calanog, J. A., et al. 2015, *Astrophys. J.*, 814, 17

Ma, X., Hopkins, P. F., Faucher-Giguère, C.-A., et al. 2016, *Mon. Not. Royal Astron. Soc.*, 456, 2140

Magnelli, B., Saintonge, A., Lutz, D., et al. 2012, *Astro. Astrophys.*, 548, A22

Mannucci, F., Cresci, G., Maiolino, R., Marconi, A., & Gnerucci, A. 2010, *Mon. Not. Royal Astron. Soc.*, 408, 2115

Messias, H., Dye, S., Nagar, N., et al. 2014, *Astro. Astrophys.*, 568, A92

Michałowski, M., Hjorth, J., & Watson, D. 2010a, *Astro. Astrophys.*, 514, A67

Michałowski, M. J., Dunlop, J. S., Cirasuolo, M., et al. 2012, *Astro. Astrophys.*, 541, A85

Michałowski, M. J., Hayward, C. C., Dunlop, J. S., et al. 2014, *Astro. Astrophys.*, 571, A75

Michałowski, M. J., Murphy, E. J., Hjorth, J., et al. 2010b, *Astro. Astrophys.*, 522, A15

Michałowski, M. J., Castro Cerón, J. M., Wardlow, J. L., et al. 2016, *Astro. Astrophys.*, 595, A72

Momcheva, I. G., Lee, J. C., Ly, C., et al. 2013, *Astron. J.*, 145, 47

Munshi, D., Heavens, A., Cooray, A., & Valageas, P. 2011, *Mon. Not. Royal Astron. Soc.*, 414, 3173

Nagai, D., Kravtsov, A. V., & Vikhlinin, A. 2007, *Astrophys. J.*, 668, 1

Narayanan, D., Bothwell, M., & Davé, R. 2012, *Mon. Not. Royal Astron. Soc.*, 426, 1178

Navarro, J. F., Frenk, C. S., & White, S. D. M. 1996, *Astrophys. J.*, 462, 563

Nayyeri, H., Keele, M., Cooray, A., et al. 2016, ArXiv e-prints, arXiv:1601.03401

Nayyeri, H., Cooray, A., Jullo, E., et al. 2017a, *Astrophys. J.*, 844, 82

—. 2017b, *Astrophys. J.*, 844, 82

Negrello, M., Perrotta, F., González-Nuevo, J., et al. 2007, *Mon. Not. Royal Astron. Soc.*, 377, 1557

Negrello, M., Hopwood, R., De Zotti, G., et al. 2010, Science, 330, 800

Okamoto, T., & Hu, W. 2003, Phys. Rev. D, 67, 083002

Oliver, S. J., Bock, J., Altieri, B., et al. 2012, *Mon. Not. Royal Astron. Soc.*, 424, 1614

Peng, C. Y., Ho, L. C., Impey, C. D., & Rix, H.-W. 2002, *Astron. J.*, 124, 266

Pettini, M., & Pagel, B. E. J. 2004, *Mon. Not. Royal Astron. Soc.*, 348, L59

Pilbratt, G. L., Riedinger, J. R., Passvogel, T., et al. 2010, *Astro. Astrophys.*, 518, L1

Planck Collaboration, Ade, P. A. R., Aghanim, N., et al. 2011a, *Astro. Astrophys.*, 536, A1

—. 2011b, *Astro. Astrophys.*, 536, A1

—. 2013, *Astro. Astrophys.*, 550, A131

—. 2014, *Astro. Astrophys.*, 571, A21

—. 2016a, *Astro. Astrophys.*, 594, A13

Planck Collaboration, Aghanim, N., Arnaud, M., et al. 2016b, *Astro. Astrophys.*, 594, A22

Planck Collaboration, Ade, P. A. R., Aghanim, N., et al. 2016c, *Astro. Astrophys.*, 594, A23

Poglitsch, A., Waelkens, C., Geis, N., et al. 2010, *Astro. Astrophys.*, 518, L2

Pontoppidan, K. M., & Wiklind, T. 2001, in Astronomical Society of the Pacific Conference Series, Vol. 237, Gravitational Lensing: Recent Progress and Future Go, ed. T. G. Brainerd & C. S. Kochanek, 183

Riechers, D. A., Hodge, J., Walter, F., Carilli, C. L., & Bertoldi, F. 2011, *Astrophys. J.*, 739, L31

Sachs, R. K., & Wolfe, A. M. 1967, *Astrophys. J.*, 147, 73

Sayers, J., Czakon, N. G., Mantz, A., et al. 2013, *Astrophys. J.*, 768, 177

Scoville, N., Aussel, H., Sheth, K., et al. 2014, *Astrophys. J.*, 783, 84

Serjeant, S. 2012, *Mon. Not. Royal Astron. Soc.*, 424, 2429

Shivaei, I., Reddy, N. A., Shapley, A. E., et al. 2015, *Astrophys. J.*, 815, 98

Simpson, J. M., Swinbank, A. M., Smail, I., et al. 2014, *Astrophys. J.*, 788, 125

Smith, K. M., Zahn, O., & Doré, O. 2007, Phys. Rev. D, 76, 043510

Sobral, D., Best, P. N., Matsuda, Y., et al. 2012, *Mon. Not. Royal Astron. Soc.*, 420, 1926

Sparre, M., Hayward, C. C., Feldmann, R., et al. 2017, *Mon. Not. Royal Astron. Soc.*, 466, 88

Speagle, J. S., Steinhardt, C. L., Capak, P. L., & Silverman, J. D. 2014, *Astrophys. J. Suppl.*, 214, 15

Spergel, D. N., & Goldberg, D. M. 1999, Phys. Rev. D, 59, 103001

Steidel, C. C., Rudie, G. C., Strom, A. L., et al. 2014, *Astrophys. J.*, 795, 165

Sunyaev, R. A., & Zeldovich, I. B. 1980, *Mon. Not. Royal Astron. Soc.*, 190, 413

Swinbank, A. M., Chapman, S. C., Smail, I., et al. 2006, *Mon. Not. Royal Astron. Soc.*, 371, 465

Swinbank, A. M., Smail, I., Chapman, S. C., et al. 2004, *Astrophys. J.*, 617, 64

Swinbank, A. M., Papadopoulos, P. P., Cox, P., et al. 2011, *Astrophys. J.*, 742, 11

Symeonidis, M., Vaccari, M., Berta, S., et al. 2013, *Mon. Not. Royal Astron. Soc.*, 431, 2317

Tacconi, L. J., Neri, R., Chapman, S. C., et al. 2006, *Astrophys. J.*, 640, 228

Tacconi, L. J., Genzel, R., Smail, I., et al. 2008, *Astrophys. J.*, 680, 246

Tacconi, L. J., Genzel, R., Neri, R., et al. 2010a, *Nature*, 463, 781

—. 2010b, *Nature*, 463, 781

Tacconi, L. J., Neri, R., Genzel, R., et al. 2013, *Astrophys. J.*, 768, 74

Takata, T., Sekiguchi, K., Smail, I., et al. 2006, *Astrophys. J.*, 651, 713

Thomas, D., Maraston, C., Bender, R., & Mendes de Oliveira, C. 2005, *Astrophys. J.*, 621, 673

Timmons, N., Cooray, A., Nayyeri, H., et al. 2015, *Astrophys. J.*, 805, 140

Timmons, N., Cooray, A., Riechers, D. A., et al. 2016, *Astrophys. J.*, 829, 21

Toft, S., Smolčić, V., Magnelli, B., et al. 2014, *Astrophys. J.*, 782, 68

van de Voort, F., Quataert, E., Hopkins, P. F., Kereš, D., & Faucher-Giguère, C.-A. 2015, *Mon. Not. Royal Astron. Soc.*, 447, 140

Van Waerbeke, L., Hinshaw, G., & Murray, N. 2014, Phys. Rev. D, 89, 023508

Vlahakis, C., Eales, S., & Dunne, L. 2007, *Mon. Not. Royal Astron. Soc.*, 379, 1042

Wardlow, J. L., Cooray, A., De Bernardis, F., et al. 2013, *Astrophys. J.*, 762, 59

Weingartner, J. C., & Draine, B. T. 2001, *Astrophys. J.*, 548, 296

Wizinowich, P. L., Le Mignant, D., Bouchez, A. H., et al. 2006, PASP, 118, 297

Wright, E. L., Eisenhardt, P. R. M., Mainzer, A. K., et al. 2010, *Astron. J.*, 140, 1868

Younger, J. D., Fazio, G. G., Wilner, D. J., et al. 2008, *Astrophys. J.*, 688, 59